NASA-TM-X-69220) NUMERICAL AND EXPERIMENTAL STUDIES OF THE NATURAL CONVECTION FLOW WITHIN A HORIZONTAL CYLINDER SUBJECTED TO A UNIFORMLY COLD WALL (NASA) 140 p HC $9.00 CSCL 20D G3/12

N73-21278

Unclas 68629

NUMERICAL AND EXPERIMENTAL STUDIES OF THE NATURAL CONVECTION FLOW WITHIN A HORIZONTAL CYLINDER SUBJECTED TO A UNIFORMLY COLD WALL BOUNDARY CONDITION

By

Roger Bell Stewart

Thesis submitted to the Graduate Faculty of the

Virginia Polytechnic Institute and State University

in partial fulfillment of the requirements for the degree of

DOCTOR OF PHILOSOPHY

in

Aerospace Engineering

MAY 973
RECEIVED
NASA STI FACIL
INPUT BRA

October 1972

I

NUMERICAL AND EXPERIMENTAL STUDIES OF THE NATURAL CONVECTION FLOW WITHIN A HORIZONTAL CYLINDER SUBJECTED TO A UNIFORMLY COLD WALL BOUNDARY CONDITION

by

Roger Bell Stewart

Thesis submitted to the Graduate Faculty of the

Virginia Polytechnic Institute and State University

in partial fulfillment of the requirements for the degree of

DOCTOR OF PHILOSOPHY

in

Aerospace Engineering

APPROVED:

Dr. J. A. Schetz, Chairman

Dr. W. B. Olstad

Dr. C. H. Lewis

Dr. J. E. Kaiser, Jr.

Dr. Yau Wu

October 1972

Blacksburg, Virginia

(ABSTRACT)

Numerical solutions are obtained for the quasi-compressible Navier-Stokes equations governing the time dependent natural convection flow within a horizontal cylinder. The early time flow development and wall heat transfer is obtained after imposing a uniformly cold wall boundary condition on the cylinder. Solutions are also obtained for the case of a time varying cold wall boundary condition. Windward explicit differencing is used for the numerical solutions. The viscous truncation error associated with this scheme is controlled so that first order accuracy is maintained in time and space. The results encompass a range of Grashof numbers from 8.34×10^4 to 7×10^7 which is within the laminar flow regime for gravitationally driven fluid flows. Experiments within a small scale instrumented horizontal cylinder revealed the time development of the temperature distribution across the boundary layer and also the decay of wall heat transfer with time. Agreement between measured temperature distributions and the numerical solutions was generally good. The time decay of the dimensionless ratio $Nu/G_r^{1/4}$ is found numerically and experimentally and, over most of the cylinder wall, good agreement is obtained between these two results. The numerical results indicate that the fluid exhibits a strong tendency to resist first order motion within the inner core region. The early establishment of a shallow positive upward temperature gradient within the core enhances its stability. No first order vortical motion is induced by the boundary layer and this is attributed in part to the fluid deceleration near the bottom of the cylinder along with expulsion of fluid from

the boundary layer in the lower portions of the cylinder.

IV

ACKNOWLEDGMENTS

The author wishes to express his appreciation to Dr. J. A. Schetz for his helpful suggestions and criticisms throughout this effort, and to the entire graduate committee for their review and suggestions on this thesis.

The author is also indebted to the National Aeronautics and Space Administration for permitting material obtained from research conducted at the Langley Research Center to be used in this thesis.

Particular thanks are due Miss Lillian R. Boney for programming the numerical work and the computer plotting routines. The author would also like to thank Mr. George W. Johnson for setting up all of the experimental apparatus as well as carrying out all of the automatic data gathering operations. Thanks are due Mrs. Gloria Evans for typing the rough draft and Joanne Halvorson who typed the final draft.

Finally the author is greatly indebted to his wife and three sons for their patient and encouraging help throughout the entire graduate effort.

TABLE OF CONTENTS

Page

Acknowledgements i

Table of Contents. ii

List of Figures. iii

List of Symbols. vi

CHAPTER

I. Introduction. 1

II. Physical Description of the Problem 5

III. Mathematical Formulation of the Governing Equations . . . 7

IV. Development of the Finite Difference Approximation to the Governing Equations 16

V. Numerical Solutions 22

A. Constant Wall Temperature Boundary Condition . . . 22

B. Time Varying Wall Temperature Boundary Condition . 29

VI. Experimental Apparatus. 35

VII. Discussion of Experimental Results. 41

VIII. Conclusions 47

IX. Bibliography. 50

X. Appendix A - Stability Analysis 52

XI. Appendix B - Thermocouple Errors. 60

Table I. 67

Figures. 68-128

VITA 129

LIST OF FIGURES

Figure — Page

1. Schematic diagram of horizontal Cylinder with coordinate system and wall boundary conditions 68

2. Finite difference grid network 69

3. Flow diagram for numerical calculations 70

   a. Continued 70
   b. Continued 71
   c. Continued 72
   d. Concluded 73

4. Azimuthal velocity distribution for a Grashof number of $7x10^7$ 74

   a. $\theta = 90°$ 74
   b. $\theta = 23.7°$ 75
   c. $\theta = 161°$ 76

5. Radial velocity distribution within the Cylinder
   a. $\theta = 90°$ 77
   b. $\theta = 23.7°$ 78
   c. $\theta = 161°$ 79
   d. $R = .44$ 80

6. Temperature distribution within the Cylinder

   a. $\theta = 90°$ 81
   b. $\theta = 23.7°$ 82
   c. $\theta = 161°$ 83

7. Dimensionless wall heat transfer decay with time 84

8. Temperature distribution within the core showing a positive upward gradient 85

9. The Nusselt-Grashof relation for a time dependent natural convection flow 86

10. The effects of radial grid refinedment

   a. Temperature distribution 87
   b. Azimuthal velocity. 88

11. Velocity and temperature distributions for a Grashof number of 8.34×10^4 89

a. Azimuthal velocity 89
b. Radial velocity 90
c. Temperature 91
d. Nusselt-Grashof Relation 92

12. Azimuthal velocity distribution for a Grashof number of 1.2×10^6 93

13. Time dependent wall temperature decay from the one dimensional heat conduction solution 94

14. Azimuthal velocity distrubution for a time dependent wall temperature boundary condition 95

15. Time dependence of the Grashof number for a time dependent wall temperature boundary condition 96

16a. Temperature distribution for a time dependent wall temperature boundary condition 97

16b. Temperature distributions for constant and variable wall temperature boundary conditions 98

17. Comparison of azimuthal velocity distribution for constant and variable wall temperature boundary conditions 99
a. Dimensionless time $\tau = 8.5$ 99
b. Dimensionless time $\tau = 26.2$ 100

18. Nusselt-Grashof relation for a time dependent wall boundary condition 101

19. Oscilloscope photographs of fluid element displacements from the numerical solutions for natural convection flow within a horizontal cylinder 102

a. $t = 0$; $t = 1.97$ sec. 102
b. $t = 3.04$; $t = 3.86$ 103
c. $t = 4.54$; $t = 5.13$ 104
d. $t = 5.67$; $t = 6.15$ 105
e. $t = 6.60$ 106

20a. Photograph of natural convection chamber 107

20b. Schematic of natural convection apparatus 108

21. Cooling manifold for natural convection chamber. 109

22. Boundary layer thermocouple installation. 110

23. Vertical flat plate apparatus for natural convection velocity measurements. 111

a. Side view 111
b. Front view. 112

24. Experimental temperature distributions for a time dependent wall boundary condition with $NG_{r\ max} = 7 \times 10^7$. 113

a. at $t = 1.2$ seconds 113
b. at $t = 4.0$ seconds 114
c. at $t = 8.0$ seconds 115

25. Experimental boundary layer decay at different azimuthal locations 116

a. $\theta = \pi/2$; $R = .966$ 116
b. $\theta = 70^o$, $R = .966$ 117
c. $\theta = 0$, $R = .966$ 118

26. Measured pressure decay within the horizontal cylinder. . . . 119

27. The Nusselt-Grashof relation for a time dependent wall boundary condition. 120

28. Experimental radial temperature distribution. 121

a. $\theta = \pi/2$; $t = 4.0$ seconds. 121
b. $\theta = \pi/2$; $t = 8.0$ seconds. 122

29. Experimental radial temperature distributions for $NG_{r\ max} = 7 \times 10^7$ 123

a. $\theta = 70^o$; $t = 4.0$ seconds. 123
b. $\theta = 70^o$; $t = 8.0$ seconds. 124

30. Experimental radial temperature distribution for $NG_{r\ max} = 1.8 \times 10^6$. 125

a. $\theta = \pi/2$; $t = 2.0$ seconds. 125
b. $\theta = \pi/2$; $t = 4.0$ seconds. 126

31. Experimental boundary layer temperature decay at $\theta = \pi/2$; $R = .966$ and $NG_{r\ max} = 1.3 \times 10^6$ 127

32. The Nusselt Grashof relation for a time dependent wall boundary condition and a maximum Grashof number of 6.5×10^5 128

LIST OF SYMBOLS

a	dimensionless constant defined in equation 5.8 and also in appendix A.
b	dimensionless constant defined in equation 5.8 and also in appendix A.
c	dimensionless constant
C_p	specific heat at constant pressure
d	diameter of cylinder
g	gravitational constant
G_r	Grashof Number = $\frac{gr_w^3}{\nu_1^2}\left(\frac{T_i - T_w}{T_i}\right)$
h	heat transfer coefficient
k	thermal conductivity
N_{pr}	Prandtl number = $\frac{c_p \mu}{k}$
N_u	Nusselt number defined by equation 5.1
p	pressure
P	dimensionless pressure
P^*	dimensionless dynamic pressure
r	radial distance from center of cylinder
R	dimensionless radial distance from center of cylinder
ΔR	distance between two successive radial grid points
$R_{e\Delta}$	computational cell Reynolds number = $U\Delta R\sqrt{G_r}$
t	time
T	temperature
T_{xo}	temperature of slab surface given by equation 5.6

u	azimuthal velocity
U	dimensionless azimuthal velocity
v	radial velocity
V	dimensionless radial velocity
x	distance into cylinder wall
α_e	artificial viscosity defined by equation 4.1
α	temperature difference given by equation 3.9
β	volumetric coefficient of expansion for a perfect gas
ρ	fluid density
$\tilde{\rho}$	dimensionless fluid density
ϕ	dimensionless temperature function defined by equation 3.9
Φ	dimensionless temperature function defined by equation 5.6
θ	azimuthal coordinate
$\Delta\theta$	distance between two successive azimuthal grid points
τ	dimensionless time
$\Delta\tau$	dimensionless time increment
μ	dynamic viscosity
ν	kinematic viscosity
h_1	Characteristic value (eigenvalue) for amplification matrix in energy stability analysis. See equation A-8
h_2	Characteristic value (eigenvalue) for amplification matrix in momentum stability analysis. See equation A-9

Subscripts

i	initial value at time = o

j	azimuthal grid point location
l	radial grid point location
w	value at cylinder wall

Superscripts

n	present value of time also summation index in equation 5.6
n + 1	new value of time

INTRODUCTION

Chapter I

Natural convection flows within closed containers have intrigued mathematicians and fluid dynamicists for many years. Part of the motivation for understanding such flows was based upon an early realization that many practical engineering situations are governed by gravitationally driven fluid flows. Present day interest is concerned with the flow of fluids within pipes, nuclear reactor cooling systems, turbine blades, and stationary containers. These fluid flows may be significantly influenced by natural or induced body forces. The resultant fluid motion and heat transfer are the principle features of interest and it is toward an understanding of these features that most studies have been directed. The early work by Nusselt (reference 1), Hermann (reference 2), Beckmann (reference 3), and Hermann (reference 4) established both the appropriate governing equations as well as the general relationship between the non-dimensional heat transfer and the Grashof number for external flows over cylindrical configurations. Numerous experimental studies have confirmed the theoretical findings (reference 5 through 7) for large values of the Grashof number wherein a boundary-layer flow is present. Not until the work reported by Ostrach (reference 8), Lewis (reference 9), Batchelor (reference 10), and Pillow (reference 11) was the internal natural convection problem given a general theoretical treatment comparable to the external problem. More recent analytical studies involving somewhat restricted

wall boundary conditions have been reported by De Vahl Davis (reference 12), Weinbaum (reference 13), Menold (reference 14), Hantman and Ostrach, (reference 15) and Gill (reference 16).

The principal problem that has thus far prevented a general analytical solution stems from the coupling between the boundary layer flow near the walls of the container and the core flow that is driven by the boundary layer flow. In formulating the problem in terms of a stream function most of the previous investigators except Hantman and Ostrach (reference 15) have been faced with the necessity of specifying a core stream function behavior that is not known a priori. Thus, depending upon specified wall boundary conditions, the core has been assumed to have either an isothermal constant vorticity character or to be stratified with streamlines extending into the boundary layer. Both analytical solutions and experiments have shown that two entirely different flow configurations are possible. If the flow is heated from below, the core streamlines are closed and the core is isothermal. If the wall boundary condition is such that heating occurs from the side, the core is stratified with isotherms and streamlines coinciding. The studies reported thus far are not able to predict the critical heating phase angle at which a rotating flow configuration changes to a stratified flow configuration. The Oseen linearization used by Weinbaum does not help the problem because this approximation decouples the core flow from the boundary layer flow. The core is expected to be closely coupled to the boundary layer flow because it is driven by the boundary layer.

B

A related problem with less troublesome boundary conditions is that of a horizontal cylinder with one half of its bounding walls raised to a constant, uniform temperature and the other half lowered an equal amount below the initial fluid temperature. Thus a rotating boundary-layer flow encircles the inside cylindrical walls with the flow rising over one half the circumference and falling over the other half. This problem was studied numerically by Hellums (reference 16). Hellums used what is now termed the windward or donor cell differencing technique for the time dependent problem starting from initially imposed wall boundary conditions. He obtained numerical solutions for the velocity, temperature, and heat transfer distributions within the cylinder. Because fluid is both entrained and ejected by the boundary-layer flow, the windward finite differencing scheme is quite suitable for this type of problem. Hellums was able to make favorable comparisons between his solutions and experiments carried out by Martini and Churchill (reference 17). These comparisons were possible for the steady state flow only. No unsteady flow measurements were reported. For steady state flow, Hellums verified the relationship between the Nusselt number and Grashof number; $Nu = C\ G_r^{1/4}$ both from a formal derivation of the dimensionless governing equations and from the resultant numerical solutions. For unsteady flow the coefficient C can be expected to be time dependent. The work reported by Hellums is closely related to the present study and will be discussed in more detail in the chapters following. At the present time only a very few of the possible boundary conditions that could be imposed on a

horizontal cylinder have been studied and with only partial success in most of the cases reported.

The work reported here represents an attempt to clarify the flow resulting from a new wall boundary condition that has not been here-to-fore studied for the internal flow problem. A uniform cold wall is established at time zero and the early time development of the fluid motion is studied. The fluid is initially at rest and will also return to rest at very large times after flow initiation. Thus a steady state is not of interest in the present work. In addition, solutions are obtained for the case in which the wall temperature decays with time. This problem corresponds to experimental boundary conditions that were imposed within a small cylinder in the present work. The experiments are described and a discussion of the relationship between the numerical work and the experimental work is given.

A Physical Description of the Problem

Chapter II

The geometry and nomenclature of the horizontal cylinder to be studied is shown in figure 1. The cylinder is of semi infinite length to allow a region of two dimensional flow to exist[1]. One practical application for such a geometry is related to a large blowdown wind tunnel storage facility in which the major heat loss to the walls occurs due to gravitationally driven natural convection flows. When a hot gas is stored in such a tank appreciable azimuthal gas flow occurs due to the imbalance between the gravitational body forces and the existing hydrostatic pressure gradient in the fluid. The gas, which is air, is initially at rest with a balance between the body force and the hydrostatic pressure gradient. The gas is initially at a uniform temperature T_i. At time zero, a uniform cold wall is imposed on the cylinder, and the resulting conduction of heat out of the gas near the wall causes the convective motion to begin. As the flow develops, a thin boundary layer is formed near the wall and this layer thickens with time. The initially motionless inner fluid (the core) is driven by the boundary layer flow and gives up energy to the heat conducting boundary layer fluid. As time progresses the boundary layer will affect the inner-most regions of the core flow and eventually the gas can be expected to give up all of its excess energy to the cold wall.

[1]A two dimensional flow within a horizontal cylinder has been observed by Brooks and Ostrach (reference 21).

When this happens the fluid will be once again at rest with a uniform temperature now equal to the wall temperature. Several distinct features are intuitively apparent. Because of the uniform wall temperature, a mid-plane of symmetry is immediately established with the dividing line running vertically upward through the center of the cylinder. Along the mid plane of symmetry the azimuthal velocity is zero. In each half cylinder there are two stagnation points which will be at the intersection of the line of mid-plane symmetry and the wall.

The principle motion in the boundary layer will be azimuthal and the induced motion will be radial. Because of the small coefficient of viscosity for air we may expect velocities of lower order in the core then in the boundary layer as well as both inward and outward radial velocities across the boundary layer. In addition it might be anticipated that some stratification of the flow will occur in the lower portions of the cylinder. The geometry and principle features of the flow having been outlined, the remainder of this thesis will be concerned with obtaining an understanding of the details of the flow from numerical solutions to the governing equations as well as experimental measurements.

Mathematical Formulation of the Governing Equations

Chapter III

The model chosen for this study is that of a viscous, heat conducting, quasi-compressible fluid that conforms to the Boussinesq approximation. For small differences between the gas temperature and the wall temperature, the density may be taken as a function of temperature only and considered as a variable only where it modifies the body force terms in the equations describing conservation of momentum. This approximation has been investigated extensively in references 4, 8, 15, and 16.

In dimensional form the quasi-compressible Navier Stokes equations applicable to the case of large Grashof Numbers and small gas to wall temperature differences in cylindrical coordinates are:

$$\frac{\partial u}{\partial t} + v\frac{\partial u}{\partial r} + \frac{u}{r}\frac{\partial u}{\partial \theta} + \frac{uv}{r} = -g \sin\theta - \frac{1}{\rho r}\frac{\partial p}{\partial \theta}$$

$$+ \frac{\mu}{\rho}\left(\frac{\partial^2 u}{\partial r^2} + \frac{1}{r}\frac{\partial u}{\partial r} - \frac{u}{r^2} + \frac{1}{r^2}\frac{\partial^2 u}{\partial \theta^2} + \frac{2}{r^2}\frac{\partial v}{\partial \theta}\right) \quad \text{Azimuthal Momentum} \qquad 3.1$$

$$\frac{\partial v}{\partial t} + v\frac{\partial v}{\partial r} + \frac{u}{r}\frac{\partial v}{\partial \theta} - \frac{u^2}{r} = g \cos\theta - \frac{1}{\rho}\frac{\partial p}{\partial r}$$

$$+ \frac{\mu}{\rho}\left(\frac{\partial^2 v}{\partial r^2} + \frac{1}{r}\frac{\partial v}{\partial r} + \frac{1}{r^2}\frac{\partial^2 v}{\partial \theta^2} - \frac{v}{r^2} - \frac{2}{r^2}\frac{\partial u}{\partial \theta}\right) \quad \text{Radial Momentum} \qquad 3.2$$

$$\frac{\partial rv}{\partial r} + \frac{\partial u}{\partial \theta} = 0 \quad \text{Mass Continuity} \qquad 3.3$$

$$\frac{\partial T}{\partial t} + v\frac{\partial T}{\partial r} + \frac{u}{r}\frac{\partial T}{\partial \theta} = \frac{K}{\rho C_p}\left(\frac{\partial^2 T}{\partial r^2} + \frac{1}{r}\frac{\partial T}{\partial r} + \frac{1}{r^2}\frac{\partial^2 T}{\partial \theta^2}\right) \quad \text{Energy} \qquad 3.4$$

Viscous dissipation and pressure work contributions to the energy equation are neglected at the outset as these terms have been shown to be negligible for gravitationally driven flows. (See Ostrach reference 18).

$$\rho = \frac{\rho_i T_i}{T} \quad \text{Boussinesq Equation of State for a perfect gas} \qquad 3.5$$

This system of equations consists of three second order, non-linear partial differential equations, one first order, linear partial differential equation and an algebraic equation of state. For the physical flow described in chapter two, the following initial and boundary conditions are imposed:

at $t = 0$

$$u(r,\theta,0) = v(r,\theta,0) = 0$$

$$T(r,\theta,0) = T_i \qquad 3.6$$

$$p(r,\theta,0) = p_i(r,\theta,0)$$

$$\rho(r,\theta,0) = \rho_i$$

at $$r = r_w$$

$$u(r_w,\theta,t) = v(r_w,\theta,t) = 0 \qquad 3.7$$

$$T(r_w,\theta,t) = T_w$$

and at $r = 0$

$$p(0,\theta,t) = p_o$$

and on $$\theta = 0 \text{ and } \pi$$

$$\frac{\partial u}{\partial \theta} = 0 \qquad \text{Mid Plane Symmetry} \qquad 3.8$$

$$\frac{\partial v}{\partial \theta} = 0$$

$$\frac{\partial T}{\partial \theta} = 0$$

The equations 3.1 - 3.8 will be more conveniently dealt with in non dimensional form. The following dimensionless quantities are defined:

$$U = \frac{u}{\sqrt{g\ \beta\alpha\ r_w}} \qquad V = \frac{v}{\sqrt{g\ \beta\alpha\ r_w}}$$

$$\phi = \frac{T_i - T}{T_i - T_w} \qquad P = \frac{p}{g\ \beta\alpha\ \rho_i\ r_w}$$

$$\alpha = T_i - T_w$$

$$\tilde{\rho} = \frac{\rho}{\rho_i} \qquad \beta\alpha = 1 - \frac{T_w}{T_i}$$

$$\beta = \frac{1}{T_i}$$

$$\tilde{\tau} = t\sqrt{g\ \beta\alpha/r_w} \qquad R = \frac{r}{r_w} \tag{3.9}$$

Substituting equations 3.9 into equations 3.1 - 3.8 and rearranging gives:

$$\frac{\partial U}{\partial \tau} + V\frac{\partial U}{\partial R} + \frac{U}{R}\frac{\partial U}{\partial \theta} + \frac{UV}{R} = \frac{-\sin\theta}{\beta\alpha} - \frac{1}{\tilde{\rho}R}\frac{\partial P}{\partial \theta}$$
$$+ \frac{1}{\sqrt{G_r}}\left(\frac{\partial^2 U}{\partial R^2} + \frac{1}{R}\frac{\partial U}{\partial R} - \frac{U}{R^2} + \frac{1}{R^2}\frac{\partial^2 U}{\partial \theta^2} + \frac{2}{R^2}\frac{\partial V}{\partial \theta}\right) \tag{3.10}$$

$$\frac{\partial V}{\partial \tau} + V\frac{\partial V}{\partial R} + U\frac{\partial V}{\partial \theta} - \frac{U^2}{R} = \frac{\cos\theta}{\beta\alpha} - \frac{1}{\tilde{\rho}}\frac{\partial P}{\partial R}$$
$$+ \frac{1}{\sqrt{G_r}}\left(\frac{\partial^2 V}{\partial R^2} + \frac{1}{R}\frac{\partial V}{\partial R} + \frac{1}{R^2}\frac{\partial^2 V}{\partial \theta^2} - \frac{V}{R} - \frac{2}{R^2}\frac{\partial U}{\partial \theta}\right) \tag{3.11}$$

$$\frac{\partial RV}{\partial R} + \frac{\partial U}{\partial \theta} = 0 \tag{3.12}$$

$$\frac{\partial\phi}{\partial\tau} + V\frac{\partial\phi}{\partial R} + \frac{U}{R}\frac{\partial\phi}{\partial\theta} =$$

$$\frac{1}{\tilde{\rho}\ P_r\sqrt{G_r}}\left(\frac{\partial^2\phi}{\partial R^2} + \frac{1}{R}\frac{\partial\phi}{\partial R} + \frac{1}{R^2}\frac{\partial^2\phi}{\partial\theta^2}\right) \qquad 3.13$$

$$\tilde{\rho} = \frac{1}{1 - \beta\alpha\phi} \qquad 3.14$$

Initial conditions

at $\tau = 0$

$$U = V = 0 \qquad 3.15$$

$$\phi = 0$$

$$P = P_i$$

$$\tilde{\rho} = 1$$

Boundary Conditions

at $R = 1.0$

$$\tilde{\rho}_w = \frac{1}{1 - \beta\alpha}$$

$$U = V = 0$$

$$\phi = 1.0 \qquad 3.16$$

and at $$R = 0$$

$$P = P_o$$

on $$\theta = 0 \quad \text{and} \quad \pi$$

$$\frac{\partial V}{\partial \theta} = \frac{\partial U}{\partial \theta} = \frac{\partial \phi}{\partial \theta} = 0 \qquad \text{Mid Plane Symmetry} \qquad 3.17$$

The nondimensionalization provides the unit order variables U, V, ϕ, and $\tilde{\rho}$. The reference pressure is $\rho_i g \beta\alpha r_w$ so that the dimensionless pressure will be greater than order one. The reference time is of order one, so the dimensionless time can also be greater than unity.

In previous investigations some simplification of equations 3.10 through 3.13 were made. Hellums (reference 16) derived the governing equations for unsteady internal flows within horizontal cylinders. The Coriolis force $\frac{UV}{R}$ as well as the derivative $\frac{\partial V}{\partial \theta}$ in the azimuthal momentum equation were shown to be negligible. In addition, the viscous terms in the radial momentum equation and the first three terms on the left hand side of equation 3.11 are negligible. (see Hermann, reference 4). Finally, the derivative $\frac{\partial^2 \phi}{\partial \theta^2}$ was found to be a low order term in equation 3.13. However the derivatives considered negligible were in fact carried along within the present computational scheme and systematic checks were made to verify that the small order of the terms persisted. Formal ordering of equation 3.10 through 3.14

by asymptotic series expansions of the dependent variables and stretching of the normal coordinate is complicated by the eventual thickening of the boundary layer. At large values of time the boundary layer is no longer thin and the matched core expansions and inner expansions are invalidated. An additional simplification to equations 3.10 through 3.14 involves the form of the pressure gradient terms.

It is convenient to divide the pressure into two separate parts:

$$P = P_i + P^* \qquad 3.18$$

P_i is the initial zero motion hydrostatic pressure. P^* is a "dynamic" pressure that arises due to motion and thermal changes within the fluid. The motivation for equation 3.18 is well founded in that the initial hydrostatic pressure gradient is known exactly:

$$\frac{1}{\tilde{\rho}R}\frac{\partial P_i}{\partial \theta} = -\frac{\sin\theta}{\tilde{\rho}} \qquad 3.19$$

$$\frac{1}{\tilde{\rho}}\frac{\partial P_i}{\partial R} = \frac{1}{\tilde{\rho}}\cos\theta \qquad 3.20$$

For many gravitationally driven flows the contribution to the overall pressure gradient from $\frac{\partial P^*}{\partial \theta}$ or $\frac{\partial P^*}{\partial R}$ is a small order effect. (see Hellums reference 16 and Ostrach reference 18). Knowledge of the hydrostatic pressure gradient facilitates solution of the governing equations through the use of equations 3.19 and 3.20. With these considerations and substituting equations 3.19 and 3.20 into equations

3.10 through 3.14 the governing system becomes:

$$\frac{\partial U}{\partial \tau} + V \frac{\partial U}{\partial R} + \frac{U}{R} \frac{\partial U}{\partial \theta} = - \phi \sin \theta - \frac{(1 - \phi \beta\alpha)}{R} \frac{\partial P^*}{\partial \theta} + \frac{1}{\sqrt{G_r}} \left(\frac{\partial^2 U}{\partial R^2} + \frac{1}{R} \frac{\partial U}{\partial R} - \frac{U}{R^2} + \frac{1}{R^2} \frac{\partial^2 U}{\partial \theta^2} \right) \qquad 3.21$$

$$\frac{\partial P^*}{\partial R} = \frac{U^2}{R} - \phi \cos \theta \qquad 3.22$$

$$\frac{\partial RV}{\partial R} + \frac{\partial U}{\partial \theta} = 0 \qquad 3.23$$

$$\frac{\partial \phi}{\partial \tau} + V \frac{\partial \phi}{\partial R} + \frac{U}{R} \frac{\partial \phi}{\partial \theta} = \frac{1}{P_r \sqrt{G_r}} \left(\frac{\partial^2 \phi}{\partial R^2} + \frac{1}{R} \frac{\partial \phi}{\partial R} \right) \qquad 3.24$$

Initial conditions

at $\tau = 0$

$$U = V = 0$$

$$\phi = 0$$

$$P^* = 0 \qquad 3.25$$

Boundary conditions

at $R = 1.0$

$$U = V = 0 \qquad 3.26$$

$$\phi = 1.0$$

and at

$$R = 0$$

$$P^* = P^*_o$$

and on

$$\theta = 0 \quad \text{and} \quad \pi$$

$$\frac{\partial U}{\partial \theta} = \frac{\partial \phi}{\partial \theta} = 0 \qquad 3.27$$

Development of the Finite Difference Approximation to the Governing Equations

Chapter IV

Low velocity fluid flows have proven difficult to solve using finite difference techniques. When the fluid velocity is low, long computational times are required, and for gravitationally driven flows that start from rest, the situation is further aggravated. The fluid flow studied here should develop maximum velocities on the order of several feet per second; thus long computational times appear unavoidable. The second difficulty arises from the fact that both positive and negative velocity components may be expected as fluid will be both entrained and expelled by the boundary layer. Numerical instabilities are produced by positive and negative coefficients of the convective terms of a difference scheme unless special care is taken regarding the form of the differencing. For these reasons an explicit, windward differencing technique was chosen (also called the donor cell technique). As shown recently by Roache (reference 19), the windward scheme along with all but one other scheme (reference 20) have only first-order accuracy in the transient development of the flow. A diffusive truncation error is introduced which appears as an artificial viscosity that may override the physical viscous damping within the fluid. Because of this, care must be taken with the windward scheme to insure that the grid size is sufficiently small so that artificial viscous effects do not have a predominant effect on the numerical development of the flow. From reference 19 it is seen that the artificial viscosity of the

C

transient windward differencing scheme in dimensional form is:

$$\alpha_e = \frac{|u|\Delta r}{2}\left(1 - \frac{|u|\Delta t}{\Delta r}\right) \qquad 4.1$$

If α_e is to be much less than the physical viscosity we may write:

$$\frac{|u|\Delta r}{2\mu}\left(1 - \frac{|u|\Delta t}{\Delta r}\right) << 1.0 \qquad 4.2$$

or

$$\Delta r << \frac{2\mu}{|u|} + |u|\,\Delta t$$

Providing that

$$u \quad \Delta t << \frac{2\mu}{|u|} \qquad 4.3$$

Thus, depending on the fluid velocity and the allowable time step obtained from stability constraints, the step size must be kept well below the right hand side of inequality 4.3. For some flows that have been studied, this requirement is over restrictive and can be relaxed. (See Callens, reference 22). With these considerations the finite difference equations approximating eqs. 3.18 - 3.25 are written as:

$$\frac{U^{n+1}_{J,\ell} - U^{n}_{J,\ell}}{\Delta\tau} + \frac{V^{n}_{J,\ell}}{\Delta R}\begin{bmatrix} U^{n}_{J,\ell+1} - U^{n}_{J,\ell} & \text{if} & V^{n}_{J,\ell} \leq 0 \\ \\ U^{n}_{J,\ell} - U^{n}_{J,\ell-1} & \text{if} & V_{J,\ell} > 0 \end{bmatrix} +$$

$$\frac{U^n_{J,\ell}}{R(\ell)\Delta\theta}\begin{bmatrix} U^n_{J+1,\ell} - U^n_{J,\ell} & \text{if} & U^n_{J,\ell} \le 0 \\ U^n_{J,\ell} - U^n_{J-1,\ell} & \text{if} & U^n_{J,\ell} > 0 \end{bmatrix} = -\phi^n_{J,\ell}\sin\theta -$$

$$(1 - \beta\alpha\,\phi^n_{J,\ell})\,\frac{P^*_{J+1,\ell} - P^*_{J,\ell}}{R(\ell)\Delta\theta} +$$

$$\frac{1}{\sqrt{G_r}\,\Delta R^2}\left[U_{J,\ell+1}\,\frac{R(\ell) + \Delta R}{R(\ell) + \frac{\Delta R}{2}} + U_{J,\ell-1}\,\frac{R(\ell) - \Delta R}{R(\ell) - \frac{\Delta R}{2}}\right.$$

$$\left. - U_{J,\ell}\left(\frac{R(\ell)}{R(\ell) + \frac{\Delta R}{2}} + \frac{R(\ell)}{R(\ell) - \frac{\Delta R}{2}}\right)\right] + \frac{1}{\sqrt{Gr}\,R^2}\left(\frac{U_{J+1,\ell} - 2U_{J,\ell} + U_{J-1,\ell}}{\Delta\theta^2}\right) \qquad 4.4$$

$$P^{*n+1}_{J,\ell} = P^{*n+1}_{J,\ell-1} - U^{2\;n+1}_{J,\ell}\,\frac{\Delta R}{R(\ell)} + (\Delta R\cos\theta)\phi^{n+1}_{J,\ell} \qquad 4.5$$

$$V^{n+1}_{J,\ell} = \left[(V_{J,\ell-1})\,\frac{R}{\Delta R} - (U_{J,\ell} - U_{J-1,\ell})^{n+1}\frac{1}{\Delta\theta}\right]\frac{1}{\left(\frac{R}{\Delta r} + 1\right)} \qquad 4.6$$

$$\frac{\phi^{n+1}_{J,\ell} - \phi^n_{J,\ell}}{\Delta\tau} + \frac{V^n_{J,\ell}}{\Delta R}\begin{bmatrix} \phi^n_{J,\ell+1} - \phi^n_{J,\ell} & \text{if} & V^n_{J,\ell} \le 0 \\ \phi^n_{J,\ell} - \phi^n_{J,\ell-1} & \text{if} & V^n_{J,\ell} > 0 \end{bmatrix}$$

$$+ \frac{U^n_{J,\ell}}{R(\ell)\Delta\theta}\begin{bmatrix} \phi^n_{J+1,\ell} - \phi^n_{J,\ell} & \text{if} & U^n_{J,\ell} \le 0 \\ \phi^n_{J,\ell} - \phi^n_{J-1,\ell} & \text{if} & U^n_{J,\ell} > 0 \end{bmatrix} =$$

$$\frac{1}{P_r\sqrt{G_r}}\left(\phi^n_{J,\ell+1} - 2\phi^n_{J,\ell} + \phi_{J,\ell-1}\right)\frac{1}{\Delta R^2} \qquad 4.7$$

at

$$\tau = 0$$

$$U = V = 0$$

$$\phi = 0 \qquad 4.8$$

$$P = P_i$$

$$\tilde{\rho} = 1$$

at $R = 1.0$ and on $\theta = 0$ and π

$$\tilde{\rho}_w = \frac{1}{1 - \beta\alpha} \qquad U_{J+1,\ell} = -U_{J-1,\ell}$$

$$U = V = 0 \qquad 4.9$$

$$\phi_w = 1.0 \qquad \phi_{J+1,\ell} = \phi_{J-1,\ell}$$

at $R = 0$ $\quad P^* = 0$

Because both U and ϕ are very small quantities near $R = 0$ the boundary condition for P^* given in equations 4.9 is a close approximation to the physical situation.

The stability and convergence of this system of equations is inferred by applying a Von Neumann stability analysis to the linearized forms of the difference equations. Appendix A provides the

details of the analysis. Although the procedure outlined by Richtmyer (reference 26) is rigorously applicable to a limited class of linear equations, it has worked successfully for the non-linear equations of fluid mechanics. The allowable time step obtained in appendix A is given by:

$$\Delta\tau \leq \frac{1}{\frac{2|U_{J,\ell}|}{R(\ell)\Delta\theta} + \frac{2|V_{J,\ell}|}{\Delta R} + \frac{4}{\sqrt{G_r}\,(R(\rho)\Delta\theta)^2} + \frac{4}{\sqrt{G_r}\,\Delta R^2}} \qquad 4.10$$

The time step chosen for most of the calculations was 0.8 of the right hand side of equation 4.10. The value provided stable calculations over the majority of cases studied. Theoretically it is difficult to establish optimum grid spacing ratios. Past work across boundary layers has been dictated by the need to resolve large gradients over short spatial lengths, and thus a fine grid spacing has been used in the spatial dimension normal to a bounding surface. For the cylindrical geometry the principal flow in the boundary layer is azimuthal, but it was found that radial flow is of primary importance in the core. A grid network that is refined in only the radial direction (normal to the cylinder walls) does not seem appropriate here. The computational experience with different grid spacing ratios indicates that a ratio $\frac{\Delta R}{\Delta\theta} << 1.0$ is essential for stable results. This probably should not be surprising in a cylindrical coordinate system because the azimuthal grid expression appears as $R(\ell)\Delta\theta$ in the difference equations, and it is immediately seen that this value reduces to $\Delta R\Delta\theta$ at the inner most

grid location next to the origin of coordinates.

The formal accuracy of the windward difference scheme is related to the computational cell Reynolds number. For the present study this number may be written as:

$$R_{e\Delta} = |U| \, \Delta R \sqrt{G_r} \qquad 4.11$$

For $R_{e\Delta} << 2$ the windward differencing will have first order accuracy in both the spatial and temporal differences.

V Numerical Solutions

A. Constant Wall Temperature

The system of equations 4.4 - 4.9 was solved for values of U, ϕ, V, and P^* over the entire grid following a step-function change in the cylinder wall temperature at time zero. A flow diagram describing the calculation sequence is shown in figure 3. It is seen that the correct difference equations are selected at each grid point depending upon the sign of $U_{j,1}$ or $V_{j,1}$ such that stable computations will result. The program was set up so that computations could be continued from a previous computer run, and thus extended run times up to 5 hours on the Langley Research Center CDC 6600 computer were made possible. Typical computational speeds for a 51 by 31 grid for the half cylinder were 1.02×10^7 grid points per hour. The real time development of the flow progressed at a rate of 1.25 seconds per hour of machine time. An order of magnitude faster flow development time was obtained with a 26 x 16 grid network; however a formal first order accuracy is not achieved with such a coarse grid.

The steps taken in the computational sequence of events were as follows:

1. Equation 4.7 was solved over the entire grid for new values of ϕ.
2. Equation 4.4 was then solved for new values of U over the entire grid.
3. Values of ϕ and U were updated.

4. Equation 4.6 was solved for the current values of V over the entire grid.
5. Equation 4.5 was solved for current values of P* over the entire grid.
6. Values of V and P* were updated.
7. Equation 4.10 was solved to determine an allowable time step.
8. Values of the Nusselt number at the wall were calculated.

The process was repeated over the entire grid for the next time step. The dimensionless heat transfer at the wall is given by the Nusselt number and obtained from the following:

$$N_u = \frac{hd}{k} \tag{5.1}$$

or

$$h = -\frac{1}{T_i - T_w} k\left(\frac{\partial T}{\partial r}\right)_{\substack{r = r_w \\ \theta = \text{const}}} \tag{5.2}$$

so that

$$N_u = \frac{1}{T_i - T_w} \frac{d}{\Delta r} \left(T_{J,\ell_{wall}} - T_{J,\ell_{wall}-1}\right) \tag{5.3}$$

or in dimensionless form:

$$N_u = \frac{2}{\Delta R} \left(1 - \phi_{J,\ell_{wall}-1}\right) \tag{5.4}$$

Table I lists the values of the input parameters that were used for the solutions to be presented. Figure 4 shows the results obtained for the case II solutions of Table I.

From the simple physical geometry of the cylinder a rather complicated flow pattern is revealed by the numerical results. Figure 4a shows the azimuthal velocity distribution at $\theta = \pi/2$ for three different time levels. The early time $\tau = 3.05$ can be considered as showing the distribution prior to what is considered to be fully developed flow. By this it is meant that peak velocities at any given location have not been achieved. The intermediate time, $\tau = 4.57$, shows the velocity distribution at its peak value, and the late time, $\tau = 14.5$, shows the distribution after a decay in the velocity has taken place. Significant inward displacement of the peak velocities is not apparent. The distributions do thicken with time over about 20 grid point spacings, and the viscous effects are transported further into the core of the fluid as time progresses. The distributions shown in figure 4 are typical of all the results obtained for the constant wall temperature case. Figure 4b shows the velocity distribution near the bottom of the cylinder at an azimuthal angle of 23.7°. The momentum gathered by the fluid falling downward has both thickened the boundary layer as well as increased the peak azimuthal velocity. At values of θ less than 23° the fluid rapidly decelerates and comes nearly to rest in the lower part of the cylinder. Figure 4c shows the velocity distribution near the top of the cylinder. The boundary layer is well defined, but the azimuthal velocities are substantially lower than in the bottom portion of the cylinder near the wall. Figure 5a shows the radial velocity distribution for case II of Table I. Here it is seen that the peak velocities are an order of magnitude less than

corresponding azimuthal velocities. The radial velocities peak at their maximum values at the later time, $\tau = 14.5$, in contrast to the azimuthal velocity peaks which occur near $\tau = 4.57$. At $\theta = 23.7^{\circ}$, figure 5b, the radial velocity is negative which indicates an explusion of fluid from the boundary layer. As the lower portion of the cylinder "fills" with fluid that has moved downward in the boundary layer, negative or radially inward flow takes place to accommodate the added fluid. Thus, fluid is slowly forced into the boundary layer near the top of the cylinder due to displacement effects from below. Figure 5c shows the radial velocity distribution in the upper portion of the cylinder. At $\theta = 161^{\circ}$ the flow is still developing with peak velocities occurring near $\tau = 14.5$.

Thus the general picture of the flow field involves three major features. First, there is a boundary-layer development near the wall due primarily to downward azimuthal fluid flow near the wall. Secondly, an induced radial velocity occurs that feeds fluid into the developing boundary layer in the upper and middle azimuthal locations of the cylinder and ejects fluid out of the boundary-layer at lower azimuthal locations. Third, a core region exists that strongly resists first-order motions and only very slowly forces fluid at lower levels to rise and enter into the boundary-layer. This is a striking example of a flow in which the principal motion is confined to the boundary layer.

The dimensionless temperature, T/T_i, is shown as a function of radial distance in figures 6. Here the thermal-boundary-layer is less

well developed than the velocity-layer at a given time. The conduction terms in the energy equation cause this behavior due to the very low fluid velocities that occur at early times after the cold wall initial condition is imposed. The accuracy of the results increases as the grid network is refined, but the computational time required for fine grids is enormous. The early behavior of wall-heat transfer is of principle interest, and figure 7 shows the Nusselt number decay with time for three different azimuthal stations. The computational results show that heat is conducted out of the fluid at early times at a greater rate than energy is convected into a fluid element. As the velocity field develops, this trend is altered causing a slight steepening of the temperature gradient near the wall. This result appears to be a valid physical description of the flow development. The convective terms in the energy equation are negligible when very low fluid velocities are present during early times. The result is an energy balance that is dominated by conduction out of the fluid to the wall until the flow field develops.

The increasing value of Nusselt number with increasing θ gives a clear picture of the positive upward temperature gradient within the boundary layer. This positive, upward gradient also exists in the core fluid as indicated by figure 8. The early establishment of this upward gradient produces a thermally stable core which tends to resist downward motion. The low velocities calculated in the core flow are in part, a result of this thermal behavior. Figure 9 shows a plot of $\frac{N_u}{G_r^{1/4}}$ as a function of time. The cold fluid entering and residing in the

lower portion of the cylinder causes a rapid and nearly linear decay of the dimensionless heat transfer function. For θ near $\pi/2$ and up to $\theta = \pi$, the function decays less rapidly due to the flow of warm fluid into the boundary layer from the core. At very large times the heat transfer function must asymptotically approach zero because the fluid gives up all of its excess energy to the wall. It is apparent that $C_1 \to \infty$ as $\tau \to 0$ due to the step function cold wall initial condition. The actual value of C_1 at early times near $\tau = o$ is dependent on the radial grid spacing used, as might be expected. A comparison of the effects of grid refinement is shown in figure 10. Here the value of T/T_i as a function of radial distance is shown for three different grid networks. The radial coordinate grid spacings are .02; .01; and .0067. The azimuthal location is $\theta = 90^\circ$, and the time is $\tau = 2.7$.

The profiles steepen as the grid is refined and convergence of the finite difference solution is evident. Of interest is the velocity distribution shown in figure 10b. Here convergence is also indicated by the refined grid results. The coarse grid velocity peak is, however, above the finer grid peaks. The slope of the distributions near the wall appears to be adjusting itself from an "overshoot" where $\Delta R = .01$ to a convergent result as ΔR becomes smaller. Similar results have been computed at Grashof numbers of 8×10^4 and 7×10^7 for the grid range given above. Case I of table I was computed for a Grashof number of 8.3×10^4. The computational time increases considerably at this relatively low Grashof number. Figure 11-a shows

some representative azimuthal velocity distributions for this case. The lower Grashof number results for this case can be interpreted as being due to a more viscous fluid flow, and the distributions reflect this. At a dimensionless time of $\tau = 3.07$ the boundary layer is considerably thicker than for the comparable boundary layer thickness of case II. Even at the early time of $\tau = 1.31$, the viscous effects are more pronounced than for the higher Grashof number case. Figure 11-b shows typical radial velocity distributions for the low Grashof number case. At $\tau = 3.07$ the distribution shows the effects of higher viscosity with a thicker profile than for the case II solution. Finally, figure 11-c shows the dimensionless temperature function distribution. Again the more viscous fluid of case I shows a thicker thermal boundary layer than the case II solution. All of the profiles for case I have a qualitative resemblance to the results for case II. The lower Grashof number solutions for the Nusselt-Grashof relation are shown in figure 11-d. These curves should be compared with the results shown in figure 9.

The computations for the dimensionless dynamic pressure, P^*, indicate that the dynamic pressure gradient makes only a small order contribution to the momentum balance within the fluid. This occurrence is consistent with the results reported by Ostrach in reference 18 and 24.

The results of the computations for case III at a Grashof number of 1.3×10^6 are shown in figure 12. The velocity profiles and temperature profiles represent a result that is intermediate to the case

I and case II solutions.

B. Time Varying Wall Temperature

Comparison of the experiments to be described in Chapter VI with numerical solutions necessitated the use of a time-dependent wall temperature boundary condition. The experimental wall temperature decay can be described by solution to the one-dimensional heat conduction equation. For a wall of thickness x_o initially at a temperature $\Phi(x,o) = 1$ where:

$$\Phi = \frac{T_w - T_{x_o}}{T_i - T_{x_o}} \qquad 5.5$$

And $t = 0$

$$T_w = T_i$$

$$\Phi(x,o) = 1 \qquad 5.6$$

T_{x_o} = Temperature of surface at $x = x_o$ after the cold wall boundary condition has been applied.

the temperature history at the inner face $x = o$ is given by:

$$\Phi(o,\tau) = 1 - \sum_{n=o}^{\infty}(-1)^n \left[2 \cdot \operatorname{erfc} \frac{(2n+1)x_o}{2\sqrt{kx \cdot \tau}} (g\ \beta\alpha/r_w)^{1/4}(\rho C)^{1/2}\right] \qquad 5.7$$

With the solution to equation 5.7 we may calculate the time dependence

of the coefficient $(G_r)^{-1/2}$ that appears in equations 4.4, 4.7, and 4.10 thus:

$$\frac{1}{(G_r)^{1/2}} = \frac{1}{(r_w^3 g/\nu_i^2)^{1/2}\left[\left(1 - \frac{T_{x_o}}{T_i}\right)\right](1 - \Phi(o,\tau))} \qquad 5.8$$

With this value calculated at each time step, the system of difference equations 4.4 through 4.10 can be solved using each new value of Grashof number which results from the time-varying wall temperature. As an example of the complementary error function solution for eq. 5.7, figure 13 shows the time-dependent dimensionless wall temperature decay. Several different limits on the number of terms taken in the summation of equation 5.7 showed rapid convergence for values of n greater than about 6. In figure 13 $n = 9$ was used for the temperature function solution.

A fundamental difficulty is encountered using the error function solution given by equation 5.7. At very early times the function is so close to unity that a near singularity is introduced into equation 5.8. The difference scheme is limited, however, to small time steps for solution of the momentum and energy equations. The wall temperature decay obtained from equation 5.7 is numerically incompatible with the difference scheme. This difficulty can be overcome by approximating equation 5.7 at early times by linear functions of the form:

$$\Phi(o,\tau) = a - b\tau \qquad 5.9$$

An approximation to the error function solution can be made using equation 5.9 if we choose: $a \leq 0.99$ and $b = 0.050$. Figure 14 shows the azimuthal velocity distribution for the case where the wall temperature decays according to equation 5.9 rearranged:

$$T_w = \Phi(o,\tau)(T_i - T_{x_o}) + T_{x_o} \qquad 5.10$$

The results shown in this figure correspond to the case II input values of Table I.

The time-dependent wall temperature solutions exhibit several interesting differences from the constant wall temperature solutions. In effect, a slowly cooled wall-boundary condition produces an early time driving force that is quite small. This is characterized by the time development of the Grashof number. Figure 15 shows a typical time history of the Grashof number for the case II input values and a wall that follows a temperature history given by equations 5.9 and 5.10. The development of the flow field is directly related to the time dependent Grashof number. The immediate consequence of a slowly cooled wall should appear as a less fully developed flow at any given time than one for which a step function wall temperature change has been imposed. The early time behavior is closely related to a lower Grashof number flow field. The boundary layer development follows the rising Grashof number with a different behavior than for the constant wall temperature results. In effect the driving force increases with time, and thus the flow experiences a longer and more pronounced acceleration. Figure

16-a shows a typical temperature distribution for the time-dependent wall boundary condition as well as for the constant wall temperature case. The details revealed by these curves are physically valid in that the constant wall temperature case, of necessity, must have a steeper slope near the wall and, in addition, must have a thinner thermal boundary layer due to the higher Grashof number at equal values of time. These features are clearly evident in figure 16-a.

A comparison of the constant and variable wall temperature cases at equal values of the Grashof number reveals the fundamental differences between the two cases. Figure 16-b shows that the variable wall temperature still has the effect of producing a more viscous flow by maintaining lower Grashof numbers throughout the entire time development than the constant cold wall case maintains. A comparison with the constant Grashof number case is difficult because of the fundamental difference between the two case histories. If the two boundary layer thicknesses are compared at equal values of R and time, we find the results shown in figure 17-a. The difference in the peak values of the dimensional velocity are of course even greater than shown in this figure because of the different value of reference velocity used in the non-dimensionalization, i.e. $u = \sqrt{g\ \beta\alpha\ r_w}\ U$. A comparison of the dimensionless azimuthal velocity distributions at equal values of both Grashof number and time is shown in figure 17-b. As expected the time varying wall case shows a thicker profile but with lower peak velocities. Similar results were observed for the temperature distribution which is also an indirect result of the

viscous behavior of the fluid. Perhaps the most significant single consideration regarding the energy transfer to the walls is the time dependent Nusselt-Grashof correlation. Hellums (reference 16) established the constant C in the relation $N_u = C\, G_r^{1/4}$. For steady flow within a horizontal cylinder C = 0.326. If a fully developed flow occurs in the present problem, the time dependent $C(\tau)$ should approach the steady value prior to a decay in the fluid motion. As time increases indefinitely in the present unsteady flow, $C(\tau) \rightarrow o$, since the fluid will then have given up all its excess energy to the cold walls. Figure 18 shows the time-dependent behavior for the Nusselt-Grashof correlation. The relation $N_u/G_r^{1/4}$ is seen to rapidly approach the steady state or fully developed value. The unsteady flow value of this relation for the present problem must be asymptotic with zero at large values of time. This behavior is demonstrated by the numerical results represented in figure 18.

Figures 19-a through 19-d illustrate the time history of "fluid particles" within the flow field from a sequence of photographs which were taken from an oscilloscope display of the particle displacements as computed from the numerical solutions. As shown in these figures particles were located, at t = 0, along rays separated by an azimuthal distance of $\pi/8$. From R = 0 to R = .64 the particles were spaced radially with $\Delta R = .04$. From R = .64 to R = 1.0 the radial spacing was $\Delta R = .01$. A two dimensional interpolation was used to obtain particle displacements between grid locations for the 31 by 101 mesh used for this case. The time dependent wall temperature decay for case II-τ of table I was used.

The sequence of photographs shows the fluid deceleration and stratification near the bottom of the cylinder. Regions where the number of particles increase represent regions of higher fluid density as might be expected. Figure 19-e is a plot of the displacements at 6.6 seconds. In this figure the particles belonging to each original ray have been faired in to illustrate the displacement profiles. Real time movies were made from plots such as these to give a physical picture of the flow field development. Because of the low velocities within the core flow, large values of time must be obtained with the numerical solutions before substantial particle displacements can be observed within the core.

Chapter VI - EXPERIMENTAL STUDIES

Apparatus

The instrumented stainless steel cylinder used for measuring temperature distributions in a gravitationally driven flow field is shown in figure 20-a. Experiments were made with the cylinder in a horizontal position, and rotation of the cylinder allowed measurements to be made at different azimuthal locations. Gage marks and internal thermocouple probes were used as references in setting the cylinder in a desired position, and a positive lock cradle was made to insure that the cylinder maintained a given position. An optical transit was used for precise orientation of the entire system. Figure 20-b is a schematic diagram of the entire apparatus. The cylinder was made of schedule 40 non magnetic stainless pipe with 300 series stainless steel end caps welded in place. The inside diameter was nominally 5.94 inches and the length was 60 inches. The cooling manifolds were insulated from the outer cooling jacket by means of one inch thick micarta rings. The purpose of this insulation was to allow filling of the coolant tanks prior to a run, and cooling the liquid to a uniform temperature without introducing conduction effects downward to the actual test cylinder. A threaded connection between the outer jacket and the test cylinder established a conduction path that had to be accounted for, and thus the insulator rings were installed.

The inside surface of the test cylinder was machined to a smooth finish with average surface projections not greater than 220 micro

inches from peak to valley. The cylinder was cleaned and vacuum leak tested prior to installation of the instrumentation. The cylinder maintained a pressure of less than 10^{-6} mm of mercury for a 24 hour period.

Figure 21 is a photograph of the cooling tanks, inlet manifolds, and outer cooling jacket surrounding the test cylinder. The valves for dumping the cooling fluid into the outer cooling jacket were manually operated, and the liquid coolant in the tanks could be completely discharged in less than one second. The "o" ring sealed valves shown in figure 20-b proved exceptionally reliable, and because of their large size the effective discharge rate from the coolant tanks was in excess of 2500 gallons per minute.

Instrumentation

Two sets of thermocouple probes were installed through the walls of the test cylinder. Initially copper-constantan thermocouple probes were installed as shown in figure 20-b for the purpose of determining whether or not a region of two dimensional flow existed in the region away from the end walls. Near the mid section of the cylinder there appeared to be no end wall effects and the thermal field was two dimensional.

The cylinder was then instrumented with a series of thermocouple probes to measure temperatures across the boundary layer at an $l/d = 5$. The boundary-layer probes were made from 30 gage copper-constantan wire with fiber sheathing left on the probes to reduce axial-conduction

losses along the wires. The probes were installed as shown in figure 22, the intent being to leave the flow field as nearly undisturbed as possible. At large values of time the probes could affect the flow recirculating from the core into the boundary layer, but the very low core velocities and core stratification found in the numerical solutions indicated that such disturbances should be negligible.

The thermocouple wires passed through stainless steel sheaths that were silver soldered into the cylinder wall. The sheaths were then encapsulated with rubber sealant, and the tank was vacuum leak tested as previously described. The thermocouple leads were housed in a controlled ice point cold junction box. The output wires from the cold junction were then lead to an analog to digital data-recording system where they were read out on computer tape. Care was taken in locating the boundary-layer thermocouple probes. These fine wires were quite easily displaced from a given position so that after being located in the correct position no further instruments or probes were inserted into the test cylinder. Also charging and purging of the cylinder was done at a slow rate to minimize convection velocities. Pressure measurements within the cylinder were made with a 0 to 15 psi absolute Statham gage and for the high Grashof number test with a 0 to 100 psi Statham gage. These gages were calibrated prior to each series of tests using a Wallace and Tiernan absolute gage as reference. The coolant temperature was monitored both in the coolant tanks and in the annular space surrounding the test cylinder by thermocouples that also lead through the cold junction to

the data recording system.

Test Procedure

The test procedure consisted of charging the cylinder with dry air at ambient temperature, sealing off the inlet and outlet valves to the cylinder, and then allowing a two hour waiting period for convection currents to damp out within the cylinder. Thirty minutes prior to a test, water and cracked ice were introduced into the coolant tanks, and the coolant was brought to a uniform and steady temperature that typically was 494°R. With all thermocouples displaying steady state readings the plug valves were opened, and the coolant was dumped over the test cylinder walls. Immediately upon opening the plug valves, a circulating pump was activated to minimize temperature gradients in the cold liquid by drawing cold liquid out of the annular region surrounding the test cylinder, and spraying the coolant back over the ice crystals in the coolant tanks. Strainers at the bottom of each tank prevented solid ice from going past the plug valves and into the annular tank chamber.

For a period of approximately five minutes following the coolant dumping, data sampling of all thermocouples and pressure instrumentation was taken. The digital system sampled each channel 400 times per second and stored the values on tape. A printer output from the digital system gave separate channel print outs at a rate of about 5 channels per second for convenience in visually following the temperature and pressure changes from the digital system.

Following a test, the coolant was removed from the system and room temperature water was flushed through the coolant tanks, valves, and annular chamber. Dry, ambient air was pumped through the test cylinder and it was sealed off when all thermocouple readings showed steady, ambient temperatures existed within the cylinder. A two hour waiting period, was then used as previously described.

Two series of tests were made using Freon and dry ice as the coolant. Wall temperatures down to $400^{\circ}R$ were achieved but it was found almost impossible to maintain uniform coolant temperatures. The problem was due to the formation of "snow" when dry ice was sublimed in Freon. A more reliable approach for raising the Grashof number was taken by pressurizing the cylinder. The experimental data reported here was obtained at a nearly constant gas to final wall temperature ratio of $\frac{T_w}{T_i} = .936$.

Attempts to Measure Gas Velocities

Considerable effort was put into an attempt to measure gas velocities near a wall in natural convection flow. Early studies by Martini and Churchill (reference 17) using titanium dioxide dust were difficult and with considerable uncertainty. The attempt made here involved the use of helium filled soap bubbles. A flat plate was constructed to test against previous experiments and theory. This plate is shown housed in a plexiglass cage in figures 23-a and 23-b. At time zero hot water was forced through three passages internal to the plate. At the same time, bubbles that were filled with mixtures of

He and N_2 and were neutrally buoyant were introduced to the lower leading edge region of the plate. Color movies were taken of the rapid entrainment of the bubbles into the plate boundary layer, and their subsequent acceleration vertically upward. Time displacement studies were made of the bubbles. Almost independent of bubble size, the bubbles all seek out a single streamline in the plate boundary layer. Thus it appears nearly impossible to measure a velocity profile. The reasoning for why the bubbles behave in this manner is based on the fact that the boundary layer is quite thin for the plate tested, and thus a steep velocity gradient normal to the plate exists which in effect produces a gradient across the bubble. Such a velocity gradient would act to draw the bubble laterally inward to a position of peak velocity within the boundary layer. A comparison of the measured velocities for both transient and steady flow conditions indicated that the bubbles were in fact traveling with close to the maximum theoretical velocities determined by Siegel (reference 25). The solution to the difficulty appears to be in producing a very thick boundary layer such that the bubble size is small compared to the change in velocity across a distance of one bubble diameter. Extensive tests were made to produce extremely small bubbles but below about .05 inches diameter neutral buoyancy cannot be achieved at standard atmospheric conditions. The hope of mapping out the velocity distribution within the cylinder by tracing the bubble displacements had to be abandoned.

Discussion of the Experimental Results

Chapter VII

Comparison of the numerical results and the experiments necessitated a consistent formulation of both the dimensionless variables as well as identical wall boundary conditions. Also the numerical solutions must have the initial conditions imposed at the same time zero as actually occurred in the experiments. It was found that within 0.4 sec after application of the cold liquid to the cylinder wall, temperature drops were detected within the gas near the wall. Thus time zero could be determined within 0.4 second by thermocouple signals alone. For comparison with the numerical results, the heat conduction equation was used for determining time zero for the experiments by allowing time zero for the conduction problem to occur when the liquid was first dumped from the hoppers. Time zero for the numerical computations and the fluid was taken when a 0.2° Rankine decrease in wall temperature had occurred due to conduction. (See equation 5.9)

As discussed in chapter 5, the near singularity in $\frac{1}{\sqrt{G_r}}$ for a time dependent wall temperature, limits the value of the constant, a, in equation 5.9 to values less than about .99.

With these considerations the measured and computed temperature distributions for an azimuthal angle of 90° are shown in figure 24. These results correspond to case II of table I with the exception of a variable wall temperature as mentioned above. The numerical solutions for 1.2, 4.0, and 8.0 seconds of real time compare favorably with the

measured results. The large computing time for the program prohibits carrying out the numerical solutions to larger values of time. The gradual thickening of the thermal boundary-layer is seen in these figures. Because the core acts as a reservoir of warm fluid for supplying the boundary layer, the temperature distributions within the layer tend to retain their profiles over a long period of time after the velocity field starts decaying. To illustrate the temperature decay, figures 25 show typical plots of both the experimental and theoretical temperature at a selected radial location. Figure 25-a shows an early time behavior both from experimental measurements, and from the numerical solutions that clearly indicates the inflection produced by the flow as the velocity distribution shifts toward a more developed profile. Similar behavior is seen in figure 25-b at $\theta = 70^{\circ}$. Finally at the bottom of the cylinder where the azimuthal motion of the fluid ceases, the temperature decay appears as shown in figure 25-c. The numerical results predict a more rapid decay than was actually measured. Several possible reasons for the disagreement are available. The most likely source of error lies within the framework of the differencing scheme near the mid-plane of symmetry. Because both the azimuthal and radial velocities are negative near the bottom of the cylinder, forward differencing is used throughout the momentum and energy equations. But forward differencing carries the grid points into regions of largest change and tends not to balance with the backward grid points that, for the present physical system, lie in regions of lesser change. Near the mid-plane the azimuthal velocity goes to zero but forward differencing

tends to override this due in part to the finite grid size, and thus it appears that errors may be largest near the bottom mid-plane of symmetry. In this respect the solutions are dependent upon the cylindrical geometry being considered. This represents a limitation or at least an undesirable aspect of one sided finite difference techniques.

It is of some interest to observe the experimentally measured pressure decay within the cylinder. This decay represents a three-dimensional (closed volume) phenomenon that is in a sense primarily dependent on the two-dimensional flow field that transports heat to the cylinder walls. Figure 26 shows a typical measured pressure decay for the case of a maximum Grashof number of 7×10^7. The pressure decay is a direct measure of the over all energy loss from the fluid. The mass in the enclosed cylinder remains constant over the total volume and thus values of the average tank pressure are a function of the average fluid temperature within the cylinder.

The single most important comparison made between the numerical results and the experiments is that of the Nusselt-Grashof relation for the time dependent flow. Figure 27 shows the measured time dependent variation of this dimensionless grouping. The comparison is favorable. Many steady state natural convection flows can be described by the Nusselt-Grashof correlation and from figure 27 it appears that a time dependent correlation could be written for an internal flow with the boundary conditions presently under consideration. The formulation of such a relation was not attempted in this study.

The Nusselt-Grashof relation is asymptotic with zero at large time as seen by:

$$\frac{N_u}{G_r^{1/4}} = \frac{2}{\Delta R} \frac{\left(1 - \phi_{J,\,\ell_{lim-1}}\right)}{\frac{r_w^3 g}{\nu_i^2}\left[\frac{T_i - T_w}{T_i}\right]^{-1/4}} \qquad 7.1$$

When $\tau \to \infty$ we find $\phi_{J,\ell_{lim-1}} \to 1$ and the right hand side of equation 7-1 goes to zero. The value of $N_u/G_r^{1/4}$ will pass through Hellum's steady state value (0.326) about 14 seconds after initiation of the flow. If figure 27 is compared to figure 18 the effect of a steadily decaying wall temperature is apparent. The curve shown in figure 27 can be interpreted as being a result of lower values of heat transfer when the wall is cooled unsteadily than when a step function cold wall is applied, such as for the figure 18 conditions.

Examples of typical experimental radial temperature distributions are shown in figure 28. In figure 28a at t = 4.0 seconds, the wall has cooled to about .983 of the initial temperature, and thus the distribution terminates at the wall (R=1.0) in the manner shown.

The thermocouple located at R = 0.2 was considered essential for monitoring the core temperature. If a very low ratio of T_w/T_i had been utilized, it could be anticipated that fluid would fall downward from the upper most walls of the cylinder. In such a case a negative vertical temperature distribution within the core might have been

E

observed. For the T_w/T_i ratio of these experiments the flow was almost completely confined within the wall boundary layers, and no negative upward distributions were measured. Figure 28-b shows the temperature distribution at 8.0 seconds after flow initiation. The measured profile has broadened more than the numerical solutions predict. Figure 29-a shows a similar result for $\theta = 70^{\circ}$.

A series of experiments at Grashof number values up to about 1.8×10^6 were made and some results are shown in figures 30. The very slow time development of the flow field is indicated by both the numerical calculations which take almost an order of magnitude longer computational time, than the case II solutions and by the experiments. The agreement between the numerical solutions and the experiments is not as good at low values of the Grashof number as at the higher Grashof numbers. The very slow development of the flow reduces the early time accuracy because of the small differences in temperature that must be measured. Figure 31 is a plot of the time history of the boundary-layer temperature at $R = .966$. The slow decay is an example of the lower Grashof number behavior. However, the relatively more rapid reduction of the gas to wall temperature ratio for the lower Grashof number case produces an undershoot of the Nusselt-Grashof relation. This is due to the differences between the velocity field development and the thermal field development and is shown in figure 32. An initial response to the near singularity at early times due to low values of the Grashof number causes the undershoot in the numerical results. Thus although the disturbance is damped by the difference

scheme, the accuracy of the results is severely lessened by the destabilizing influence of a very low early time Grashof number. Restated, the low Grashof number computations are characterized by a relatively rapid wall cooling which raises the wall heat transfer more rapidly than the one fourth power of the Grashof number. The Nusselt-Grashof behavior in both figure 27 and figure 32 must be viewed as being representative of one specific flow configuration, and also a very specific boundary condition. The difference between figures 27 and 32 indicates that a single correlation equation from the numerical results presented here, may not be possible to achieve for the entire range of unsteady laminar natural convection flow within a horizontal cylinder.

Conclusions

Chapter VIII

The present investigation has revealed the dynamic and thermal behavior of a confined fluid subjected to gravitational body forces. For a semi-infinite horizontal cylinder with uniformly cold walls the principle features of the flow involve a rapid development of the boundary layer adjacent to the walls, a tendency for fluid stratification in the lower regions of the cylinder, and a slow decay of the velocity and thermal fields with time. Experiments made in this investigation substantiate the thermal behavior predicted by numerical solutions to the quasi-compressible Navier-Stokes equations for the case of a time dependent wall temperature decay. Because the thermal and velocity fields are strongly coupled, the experimental findings imply that the velocity field may also be accurately described by the numerical results.

The following conclusions can be drawn from this study:

1. For very low velocity natural convection flows, windward finite differencing, which gives first order accuracy in time and space, is a suitable numerical scheme when positive and negative velocities occur. The large computing times required for such flow fields rules out more time consuming differencing schemes at the present time.

2. The windward scheme in cylindrical coordinates was not extremely sensitive to grid spacing ratios except when the ratio $\frac{\Delta R}{\Delta \theta} > 0.2$. Above this value, numerical instabilities occurred regardless

of the time step used.

3. The differencing scheme appeared to lose accuracy near the bottom of the cylinder where both the radial and azimuthal velocities are negative, and the azimuthal velocity is decelerating to zero at $\theta = 0$.

4. The early establishment of a positive upward temperature gradient within the central core flow, along with the effects of fluid viscosity combine to produce a strong resistance to induced fluid motion within the core. After initiation, the flow within the boundary layer develops rapidly, and decays over a long period of time.

5. The dynamic pressure gradient terms $\frac{1}{R}\frac{\partial P^*}{\partial \theta}$ and $\frac{\partial P^*}{\partial R}$ are negligible in the azimuthal and radial momentum equations for the conditions considered in this investigation.

6. The relationship between the Nusselt and Grashof numbers is found both numerically and experimentally for the case of unsteady natural convection flow within a horizontal cylinder subjected to uniformly cold wall boundary conditions. For the case of a time dependent wall boundary condition, the Nusselt-Grashof relation intercepts the steady state value of the dimensionless group about 14 seconds after the commencement of flow down the cylinder walls. For the case of a constant cold wall condition from time zero, the numerical results show that the Nusselt-Grashof relation intercepts the steady state value at about 3 second after commencement of the flow.

7. No first order vortical motion was found within the core flow. The absence of this motion is attributed to the boundary conditions

which require azimuthal deceleration of the boundary layer flow near the bottom of the cylinder. Both the theoretical and experimental models establish a mid plane of symmetry that satisfies the boundary conditions imposed in this study.

Bibliography

1. Nusselt, W.: Gesundh. Ing., Bd. 38, 1915.

2. Hermann, E.: Phys. Zeichshrift Bd. 33. 1932.

3. Beckmann, W.: Forsch Ing.-Wes., Bd. 2 1931.

4. Hermann, R.: Heat Transfer by Free Convection from Horizontal Cylinders in Diatomic Gases, NACA TM-1366 1954 (Translation).

5. Wamsler, F.: VDI Forschungsheft. 98/99 (Berlin) 1911.

6. Koch, W.: Beih. z. Gesundh.-Ing. Reihe 1, Heft 22 1927.

7. Jodlbauer, K.: Forsch. Ing.-Wes., Bd. 4 1933.

8. Ostrach, S.: Laminar Natural Convection Flow and Heat Transfer of Fluids with and without Heat Sources in Channels with Constant Wall Temperatures NACA TN-2863 1952.

9. Lewis, J. A.: Free Convection in Commercial Insulating Materials Ph. d. Thesis, Brown University Providence, R. I. 1950.

10. Batchelor, G. K.: Heat Transfer by Free Convection across a Closed Cavity between Vertical Boundaries at Different Temperatures. Quart. Journ. of Appl. Math. 12 209 1954.

11. Pillow, A. F.: The Free Convection Cell in Two Dimensions, Aero Research Lab. Dept. A-79 1952, Melbourne, Australia.

12. de Vahl Davis, G.: Laminar Natural Convection in a Rectangular Cavity, New York University, School of Eng. Report No. F-67-2 1967.

13. Weinbaum, S.: Natural Convection in a Horizontal Cylinder, Journ. of Fluid Mechanics, 18, 409 1964.

14. Menold, E.: Natural Convection in a Horizontal Cylinder at Large Prandtl Numbers, Case Institute of Technology, Ph.d Thesis, 1966.

15. Hantman, R. G.; Ostrach, S.: Natural Convection inside a Horizontal Cylinder, AFOSR Scientific Report AFOSR68-2341 1969.

16. Hellums, J. D.: Finite Difference Computation of Natural Convection Heat Transfer, Ph. d. Thesis University of Michigan, 1961.

17. Martini, W. R.; Churchill, S. W.: Natural Convection inside a Horizontal Cylinder, American Institute of Chemical Engineers J. 6. 251,1960.

18. Ostrach, S.: Laminar Flows with Body Forces, The Theory of Laminar Flows, Ed. F. K. Moore, Princeton University Press, Princeton New Jersey, 1964.

19. Roache, P. J.: On Artificial Viscosity Sandia Research Report SC-PR-71-0301, 1971.

20. Lax, P. D.; Wendroff, B.: Systems of Conservation Laws, Communications on Pure and Applied Mathematics Vol. 13, 217-237, 1960.

21. Brooks, I. H.; Ostrach, S.: An Experimental Investigation of Natural Convection in a Horizontal Cylinder, AFOSR Scientific Report., TR-69-0174, 1969.

22. Callens, E. E. Jr.: A Time Dependent Approach to Fluid Mechanical Phenomenology, AIAA Paper 70-46, January 1, 1970.

23. McAdams, W. H.: Heat Transmission 3rd Ed. McGraw-Hill 1954.

24. Ostrach, S.: An Analysis of Laminar Free Convection Flow and Heat Transfer about a Flat Plate Parallel to the Direction of the Generating Body Force. NACA Report 1111, 1953.

25. Siegel, R.: Transient Free Convection from a Vertical Flat Plate Transactions of the ASME Vol. 80 No. 2 February 1958.

26. Richtmyer, R. D.: Difference Methods for Initial Value Problems Interscience Publishers, 1957.

27. Moffat, R. J.: Gas Temperature Measurement in Temperature its Measurement and Control Science and Industry Vol. 3 Part 2 C. M. Herzfeld Ed. Reinhold Corp. 1962.

Stability Analysis

Appendix A

The von Neumann stability analysis deals with linearized forms of the governing equations. The coefficient velocities are all considered constant in equations 3.10 through 3.13. The effects of amplification of disturbances due to non linear terms is not within the scope of this method, however, the von Neumann criteria does provide an approximate stability limit that has proved quite suitable for non-linear fluid flow problems. The analysis will be made for the coupled system composed of the azimuthal momentum equation and the energy equation. The differences for the cross derivatives that do not appear in equations 4.4 and 4.7 will be included for stability considerations. Define the following equalities:

$$B = \frac{|U|\Delta\tau}{R\Delta\theta}$$

$$C = \frac{\Delta\tau}{\Delta R^2} \qquad D = \frac{\Delta\tau}{(R\Delta\theta)^2} \qquad E = \frac{1}{P_r\sqrt{G_r}} \qquad \text{A-1}$$

$$F = \frac{\Delta\tau}{R\Delta R} \qquad G = \frac{|V|\Delta\tau}{\Delta R}$$

$$H = \frac{1}{\sqrt{G_r}}$$

Use of absolute values on U and V allows the results of the analysis to be applied to fluid flows with either positive or negative

velocity components. Substituting equations A-1 into the energy equation gives:

$$\phi^{n+1}_{J,\ell} = \phi^{n}_{J,\ell}(1 - G - B - 2DE - 2EC) + \phi^{n}_{J,\ell-1}(G + EC - \frac{EF}{2})$$

$$+ \phi^{n}_{J-1,\ell}(B + ED) + \phi^{n}_{J+1,\ell}(ED) + \phi^{n}_{J,\ell+1}(EC + \frac{EF}{2}) \qquad \text{A-2}$$

Similarly equation 3 10 yields

$$U^{n+1}_{J,\ell} = U^{n}_{J,\ell}\left[1 - G - B - CH\left(\frac{R}{Rr\,\frac{\Delta R}{2}} + \frac{R}{R - \frac{\Delta R}{2}}\right) - 2DH\right]$$

$$+ U^{n}_{J,\ell-1}\left[G + CH\left(\frac{R - \Delta R}{R - \frac{\Delta R}{2}}\right)\right] + U^{n}_{J-1,\ell}(B + DH)$$

$$+ U^{n}_{J,\ell+1}\left[CH\left(\frac{R + \Delta R}{R + \frac{\Delta R}{2}}\right)\right] + U^{n}_{J+1,\ell}(DH)$$

$$- \sin\theta(1 - \phi^{n}_{J,\ell})\Delta\tau - G\,U^{n}_{J,\ell} \qquad \text{A-3}$$

For equation A-2 we define

$$a_1 = 1 - G - B - 2DE - 2EC$$

$$a_2 = G + EC - \frac{EF}{2}$$

$$a_3 = B + ED \qquad \text{A-4}$$

$$a_4 = ED$$

$$a_5 = EC + \frac{EF}{2}$$

and for equation A-3 we define:

$$b_1 = 1 - G - B - CH\left(\frac{R}{R + \frac{\Delta R}{2}} + \frac{R}{R - \frac{\Delta R}{2}}\right) - 2DH$$

$$b_2 = G + CH\left(\frac{R - \Delta R}{R - \frac{\Delta R}{2}}\right)$$

$$b_3 = B + \Delta H$$

$$b_4 = CH\,\frac{R + \Delta R}{R + \frac{\Delta R}{2}} \qquad \text{A-5}$$

$$b_5 = DH$$

Substituting equations A-4 into A-2 gives

$$\phi^{n+1}_{J,\ell} = a_1\phi^n_{J,\ell} + a_2\phi^n_{J,\ell-1} + a_3\phi^n_{J-1,\ell} + a_4\phi^n_{J+1,\ell} + a_5\phi^n_{J,\ell+1} \qquad \text{A-6}$$

and substituting equations A-5 into equation A-3 gives:

$$U^{n+1}_{J,\ell} = b_1U^n_{J,\ell} + b_2U^n_{J,\ell-1} + b_3U^n_{J-1,\ell} + b_4U^n_{J,\ell} + b_5U^n_{J+1,\ell}$$

$$- \sin\theta(1 - \phi^n_{J,\ell})\Delta\tau - U^n_{J,\ell}V^n_{J,\ell}\,\frac{\Delta\tau}{\Delta R} \qquad \text{A-7}$$

The amplification matrices formed from the coefficients in eqs. A-6 and A-7 have characteristic values (eigenvalues), h_1 and h_2.

For the energy equation:

$$h_1 = a_1 + a_2 e^{-ik_2 \Delta R} + a_3 e^{-ik_1 R\Delta\theta} + a_4 e^{ik_2 \Delta R} + a_5 e^{ik_2 R\Delta\theta} \qquad \text{A-8}$$

For the momentum equation:

$$h_2 = b_1 + b_2 e^{-ik_2 \Delta R} + b_3 e^{-ik_1 R\Delta\theta} + b_4 e^{ik_2 \Delta R} + b_5 e^{ik_1 R\Delta\theta} \qquad \text{A-9}$$

The von Neumann condition can be written as $|h| \leq 1.0$. The a_k and b_k are all real and positive except for a_1 and b_1 which may be either positive or negative. As indicated by Richtmyer (reference 26) and Hellums (reference 16) the largest absolute values of h_1 and h_2 will occur when all terms in equations A-8 and A-9 are real i.e. when

$$k_1 R\Delta\theta = k_2 \Delta R = \pi$$

or

$$k_1 R\Delta\theta = k_2 \Delta R = 2\pi$$

For the maximum real value of h_1 we write:

$$h_{1\ max} = a_1 + a_2 + a_3 + a_4 + a_5 \qquad \text{A-10}$$

or substituting from equation A-4 we get:

$$h_{1\ max} = 1 - G - B - 2DE - 2CE + G + CE - \frac{EF}{2} + B + 2DE + CE + \frac{EF}{2} \qquad \text{A-11}$$

or $$h_{1\ max} = 1 \qquad \text{A-12}$$

For the minimum value we find:

$$h_{1\ min} = a_1 - a_2 - a_3 - a_4 - a_5 \qquad \text{A-13}$$

Substituting from equations A-4 gives:

$$h_{1\ min} = 1 - G - B - 2DE - 2CE - G - CE + \frac{EF}{2} - B - 2DE - CE - \frac{EF}{2} \qquad \text{A-14}$$

or $$h_{1\ min} = 1 - 2 - G - 2B - 4DE - 4CE \qquad \text{A-15}$$

For stability we must have

$$2G + 2B + 4DE + 4CE \leq 1 \qquad \text{A-16}$$

Equation A-16 is the stability equation governing the energy equation.

Substituting equations A-1 into equation A-16 gives:

$$\frac{2|V|\Delta\tau}{\Delta R} + \frac{2|U|\Delta\tau}{R\Delta\theta} + \frac{4\Delta\tau}{(R\Delta\theta)^2 P_r\sqrt{G_r}} + \frac{4\Delta\tau}{\Delta R^2 P_r\sqrt{G_r}} \leq 1 \qquad \text{A-17}$$

or rearranging gives the maximum allowable time step for stability of the energy equation:

$$\Delta\tau \leq \frac{1}{\frac{2|V|}{\Delta R} + \frac{2|U|}{R\Delta\theta} + \frac{4}{(R\Delta\theta)^2 P_r \sqrt{G_r}} + \frac{4}{\Delta R^2 P_r \sqrt{G_r}}} \qquad \text{A-18}$$

Similarly for the momentum equation we find that:

$$h_{2\ max} = b_1 + b_2 + b_3 + b_4 + b_5 \qquad \text{A-19}$$

Substituting equation A-5 into equation A-19 we get:

$$h_{2\ max} = 1 - G - B - CH\left(\frac{R}{R + \frac{\Delta R}{2}} + \frac{R}{R - \frac{\Delta R}{2}}\right) - 2DH$$

$$+ G + CH\left(\frac{R - \Delta R}{R - \frac{\Delta R}{2}}\right) + B + DH + CH\left(\frac{R + \Delta R}{R + \frac{\Delta R}{2}}\right) \qquad \text{A-20}$$

$$+ DH$$

Simplifying gives:

$$h_{2\ max} = 1 + \frac{CH\ R}{R - \frac{\Delta R}{2}} - \frac{CH\ \Delta R}{R - \frac{\Delta R}{2}} + \frac{CH\ R}{R + \frac{\Delta R}{2}}$$

$$+ \frac{CH\ \Delta R}{R + \frac{\Delta R}{2}} - \frac{CH\ R}{R + \frac{\Delta R}{2}} - \frac{CH\ R}{R - \frac{\Delta R}{2}} \qquad \text{A-21}$$

or

$$h_{2\ max} = 1 + CH\left(\frac{\Delta R}{R + \frac{\Delta R}{2}} - \frac{\Delta R}{R - \frac{\Delta R}{2}}\right) \qquad \text{A-22}$$

If we exclude the origin then R will never be less than ΔR so from equation A-22 we see that $h_{2\ max}$ cannot exceed unity. (If R is large the term in parentheses in equation A-22 will be small). Now if $R = \Delta R$ equation A-22 gives:

$$h_{2\ max} = 1 - \frac{4}{3} CH \qquad \text{A-23}$$

This leads to the expression

$$\Delta\tau \leq \frac{3}{4} \Delta R^2 \sqrt{G_r} \qquad \text{A-24}$$

For large Grashof number flows equation A-24 does not impose a severe restriction on the allowable time step. For the minimum value of h_2 we write:

$$h_{2\ min} = b_1 - b_2 - b_3 - b_4 - b_5 \qquad \text{A-25}$$

or substituting equations A-5 into equation A-25 and simplifying gives:

$$h_{2\ max} = 1 - 2G - 2B - 4DH - CH \left[\frac{R - \Delta R}{R - \frac{\Delta R}{2}} + \frac{R}{R + \frac{\Delta R}{2}} + \frac{R}{R - \frac{\Delta R}{2}} \right] \qquad \text{A-26}$$

For stability we write:

$$2G + 2B + 4DH + 4CH \leq 1 \qquad \text{A-27}$$

F

Substituting equations A-1 into equation A-27 gives:

$$\frac{2|V|\Delta\tau}{\Delta R} + \frac{2|U|\Delta\tau}{R\Delta\theta} + \frac{4\Delta\tau}{(R\Delta\theta)^2\sqrt{G_r}} + \frac{4\Delta\tau}{(\Delta R)^2\sqrt{G_r}} \leq 1 \qquad \text{A-28}$$

Rearranging equation A-28 gives:

$$\Delta\tau \leq \frac{1}{\frac{2|V|}{\Delta R} + \frac{2|U|}{R\Delta\theta} + \frac{4}{(R\Delta\theta)^2\sqrt{G_r}} + \frac{4}{\Delta R^2\sqrt{G_r}}} \qquad \text{A-29}$$

Thus from the von Neumann approach the most stringent stability requirement for the present system of equations is given by equation A-29. (For the case where $NPr \leq 1.0$). This criteria is at most an approximation and requires validation by computer experiments. The studies reported here have in fact verified that the von Neumann criteria is a good approximation and any local violation of the limit given by equation A-29 resulted in large scale instabilities that develop quite rapidly in the computation.

Thermocouple Errors

Appendix B

There are four sources of temperature measurement error in addition to actual signal readout errors that must be investigated for any experimental study. These errors can be classified as being due to: (1) fluid velocity past the sensor; (2) conduction losses along the thermocouple wires; (3) radiation of energy from the thermocouple to its surroundings; (4) transient error due to a finite time lag in response caused by the thermal capacity of the sensor. These errors will be evaluated for operating conditions that are typical of the experiments carried out. Moffat (reference 27) gives a detailed discussion of the pertinent equations for such an analysis.

Thermocouple velocity error

The difference between the gas total temperature T_T and the temperature, T_J, given by the junction is:

$$T_T - T_J = (1 - \alpha_r) \frac{U_\infty^2}{2gJC_p} \qquad \text{B-1}$$

where:

α_r = Recovery Factor = $\dfrac{T_J - T_\infty}{T_T - T_\infty}$

T_∞ = fluid static temperature

U_∞ = fluid velocity

The recovery factor for wires perpendicular to the flow has been extensively studied and a summary of the results is shown in reference

27. For the very low fluid velocities encountered in the present work the recovery factor can be conservatively taken as: $\alpha_r = 0.61$. For a maximum fluid velocity of 4 feet/second the velocity error is calculated as:

$$T_T - T_J = \frac{(.39)16}{2(32.174)(.24)778} = 5.19 \times 10^{-4}\ {}^{o}F$$

The velocity error appears to be negligible for the present experimental conditions.

Conduction Error

The losses due to axial conduction along the thermocouple wires are given by the following equation:

$$T_T - T_J = \frac{T_T - T_M}{\cosh L(4hc/dk_s)} \qquad \text{B-2}$$

where:

T_T = Fluid Total Temperature

T_M = Mount Temperature

L = Distance from the Wall to the Sensor Junction

d = Wire Diameter

h_C = Convective Heat Transfer Coefficient

k_S = Thermal Conductivity of Sensor

k_G = Thermal Conductivity of the Gas Evaluated at Stagnation Conditions

The Reynolds number based on wire diameter is given as:

$$R_{ed} = \frac{\rho_T U_\infty d}{\mu_T} = \frac{4(8.33 \times 10^{-4})}{1.46 \times 10^{-4}} = 22.8 \qquad \text{B-3}$$

If the correlation equation of reference 27 for wires and perpendicular to the flow is used, the following results are obtained:

$$N_u = (.44 \pm .06) R_{ed}^{1/2} \qquad \text{B-4}$$

with

$$h_c = \frac{k_g N_u}{d} \qquad \text{B-5}$$

so that B-6

For a fluid total temperature $T_T = 536^\circ R$ and a mount temperature $T_M = 492^\circ R$ equation B-2 gives:

$$T_T - T_J = \frac{44}{\cosh 414} \qquad \text{B-7}$$

Thus

$$T_T - T_J << 1^\circ R \qquad \text{B-8}$$

The conduction losses are seen to be entirely negligible even for the shortest thermocouple sensors used in this investigation.

Radiation Losses

The radiation loss for a thermocouple within an enclosure is given by:

$$T_T - T_J = \frac{k_r \sigma \varepsilon}{h_c} \frac{A_R}{A_c} (T_J^4 - T_w^4) \qquad \text{B-9}$$

where

K_r = Radiation Form Factor

σ = Stefan Boltzman Constant

$\frac{A_r}{A_c}$ = Ratio of Area Available for Radiative Loss to Area Available for Convective Loss.

ε = Emissivity Compared to a Black body

For an enclosure that is large compared to the wire dimensions it is known that $K_r \simeq 1.0$.

For the present problem we may also write $\frac{A_r}{A_c} = 1.0$. Also for oxidized base metal thermocouples $\varepsilon \approx .85$. And

$$\sigma = 4.75 \times 10^{-13} \frac{Bt_4}{Ft^2 \sec^{o}R} \qquad \text{B-10}$$

Considering the largest gas to wall temperature difference to be $20^{o}R$ for the unsteady wall temperature decay of the present experiments, equation B-8 gives:

$$T_T - T_J = 3.70 \times 10^{-11} (1.14 \times 10^{10})$$

Thus

$$(T_J - T_J)_{max} = 0.42^{o}R \qquad \text{B-11}$$

Thus the radiative losses for the case of an unsteady wall temperature decay can be of significance. Within the boundary layer there is some reduction of the loss due to lower fluid temperatures. This affect is partially overcome by a reduction in the value of h_c within

boundary layer. As a percentage of the total gas temperature, equation B-11 represents a very small correction. It is however a known source of error and equation B-8 must be applied to the thermocouples that reach a junction to wall temperature difference near the values used to give equation B-11.

Transient Error

The lag in thermocouple response can be characterized by:

$$T_T - T_J = \omega \frac{dT_i}{dt} \qquad \text{B-12}$$

where

$$\omega = \frac{\rho c d}{4h_c} \qquad \text{B-13}$$

ω is a characteristic time that depends directly on the thermal storage capacity of the thermocouple and inversely upon the heat input to the thermocouple per degree of temperature difference.

For Copper

$$C = .0918 \ \frac{\text{BTU}}{\text{Lb } ^{o}\text{R}}$$

so that

$$\omega = \frac{(430)(.0918)}{4(1.09 \times 10^{-2})} \ \frac{.01}{12} = .754 \text{ seconds} \qquad \text{B-14}$$

Thus

$$\left(\frac{dT_i}{dt}\right)_{max} = 0.55\ ^{o}R/sec.$$

The maximum transient error is close to the radiative error and very neatly compensates for the radiative error calculated previously.

Other errors were reduced to a minimum for the system by calibration of the pressure instrumentation prior to each series of tests and also by performing a precise balance of the readout system prior to each test.

A large number of tests were carried out and each test condition reported here was duplicated at least three individual times. The comparison of temperature and pressure histories for duplicate tests is very close with random variations in temperature readings of no more than 1 ^{o}R between two tests run at the same conditions. The time history of pressure and temperature within the horizontal cylinder could be duplicated within 0.5 $^{o}/o$ from one test to another. This close repeatability was obtained over the entire Grashof number range of the experiments. Systematic errors are established by the limits of output accuracy of the sensors and pressure transducers and the total readout system. The rapid sampling rate of the automatic readout system removes the need for analyzing the experimental uncertainty by means of a Gaussian error curve. Instead, it is seen that the fluctuations shrink the distribution curve inside the smallest scale divisions of the readout system. As an illustration data samples are taken at a rate of 400 samples per second. The peak rate of temperature change measured

was close to $1^{\circ}R$ per second so that effectively 100 sample readings were taken within each 1/4 $^{\circ}R$ change in the value of temperature. For machine plotted data this is about the limit of scale size that can usefully be worked with. The data readings are truly scale limited rather than being perturbation limited. The absolute uncertainty of the temperature measurements is set by the error limits of the thermocouple junction itself. All known system errors are far below the thermocouple error which commercially is given as $\pm$ 1 1/2$^{\circ}F$. Calibrations of the thermocouples within a controlled ice point instrument showed less than 1/2 $^{\circ}F$ discrepancy between recorded signal and the ice point temperature. The temperature measurements have an overall uncertainty of something on the order of $\pm$ 1 1/2$^{\circ}F$ which is within about $\pm$0.2 $^{\circ}/_{o}$ of the measured values.

Table I

Parameter Variations for Numerical Studies

Case I	Case II	Case III
$NG_r = 8.34 \times 10^4$	$NG_r = 7 \times 10^7$	$NG_r = 1.36 \times 10^6$
$P_r = .715$	$P_r = .715$	$P_r = .715$
$\frac{T_w}{T_i} = .936$	$\frac{T_w}{T_i} = .936$	$\frac{T_w}{T_i} = .936$
T_w = constant	T_w = constant	T_w = constant
$r_w = 0.1$ ft.	$r_w = .25$ ft.	$r_w = .25$ ft.
$P_i = 1$ atm.	$P_i = 6.74$ atm.	$P_i = 1$ atm.

Case II - τ

Identical to Case II except:

$$T_w = \Phi(o,\tau)(T_i - T_{x_o}) + T_{x_o}$$

Case III - τ

Identical to Case III except:

$$T_w = \Phi(o,\tau)(T_i - T_{x_o}) + T_{x_o}$$

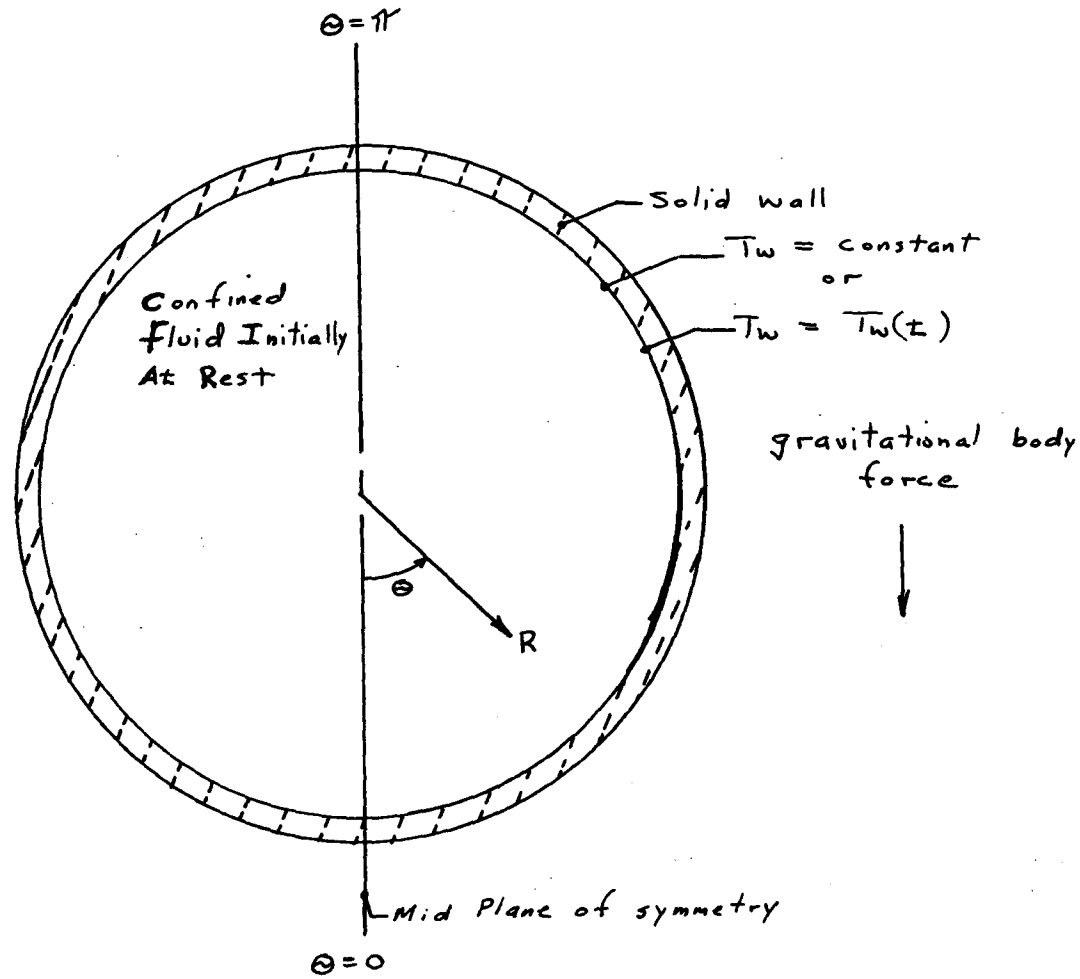

Figure 1.- Geometry of horizontal cylinder.

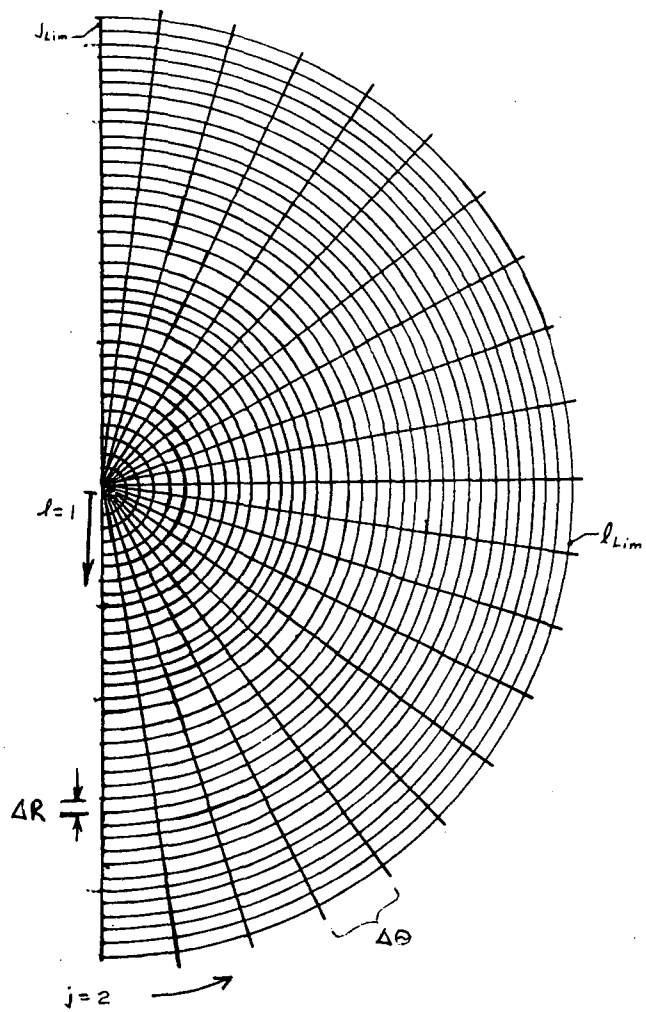

Grid Sizes Used		
ΔR	$\Delta\Theta$	Grid
.0067	.108	151 by 31
.01	.108	101 by 31
.02	.108	51 by 31

Figure 2.- Finite difference grid network.

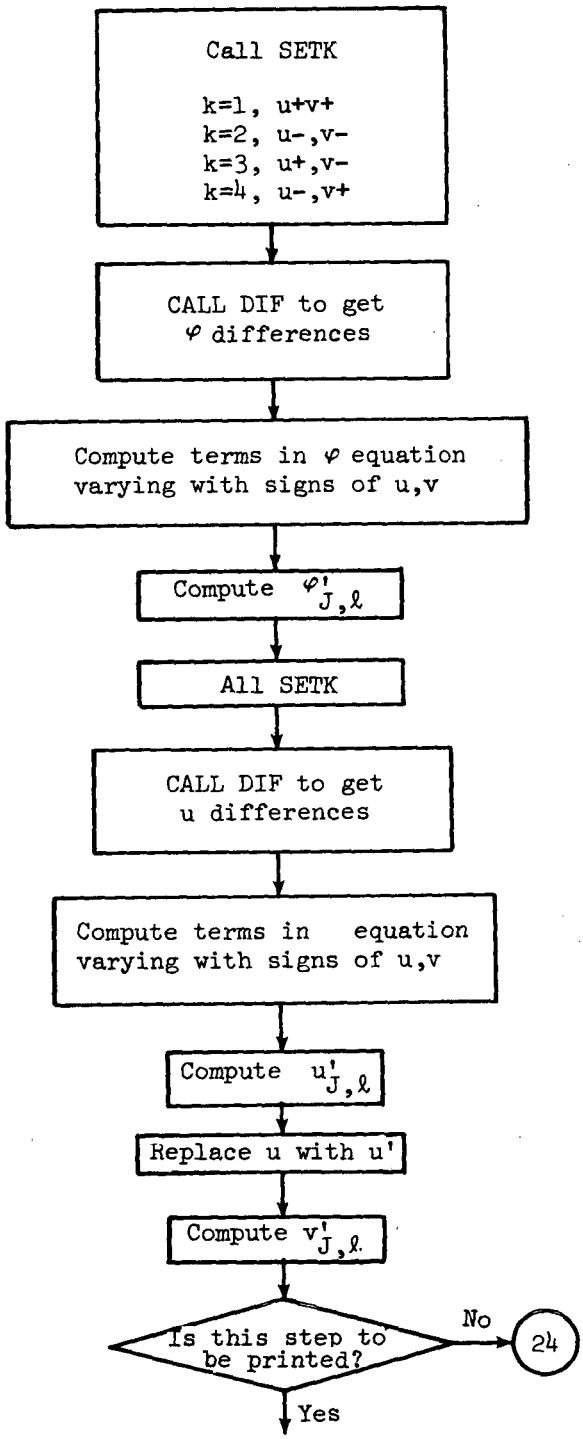

Figure 3a.- Flow diagram for finite difference calculation.

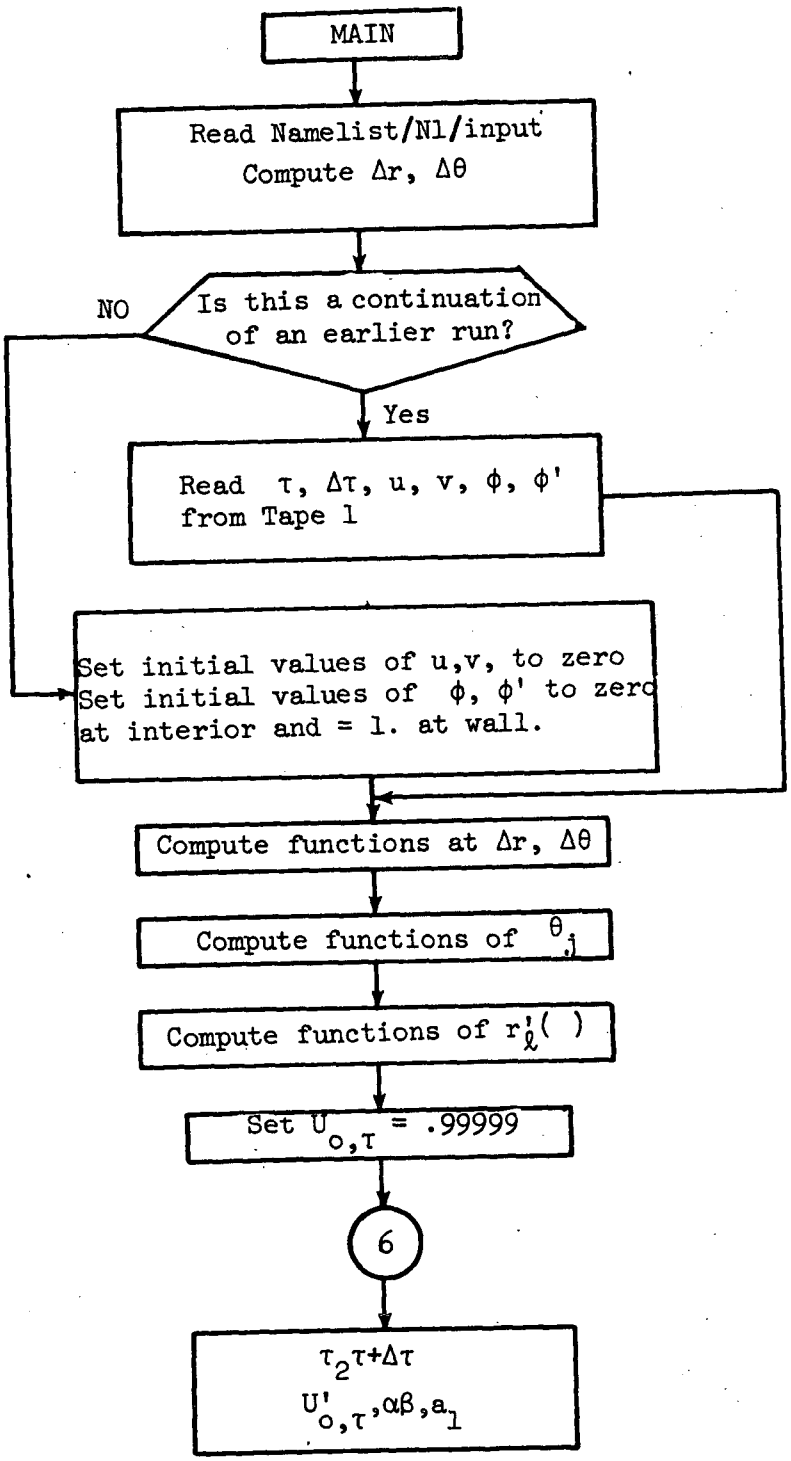

Figure 3-b.- (Continued).

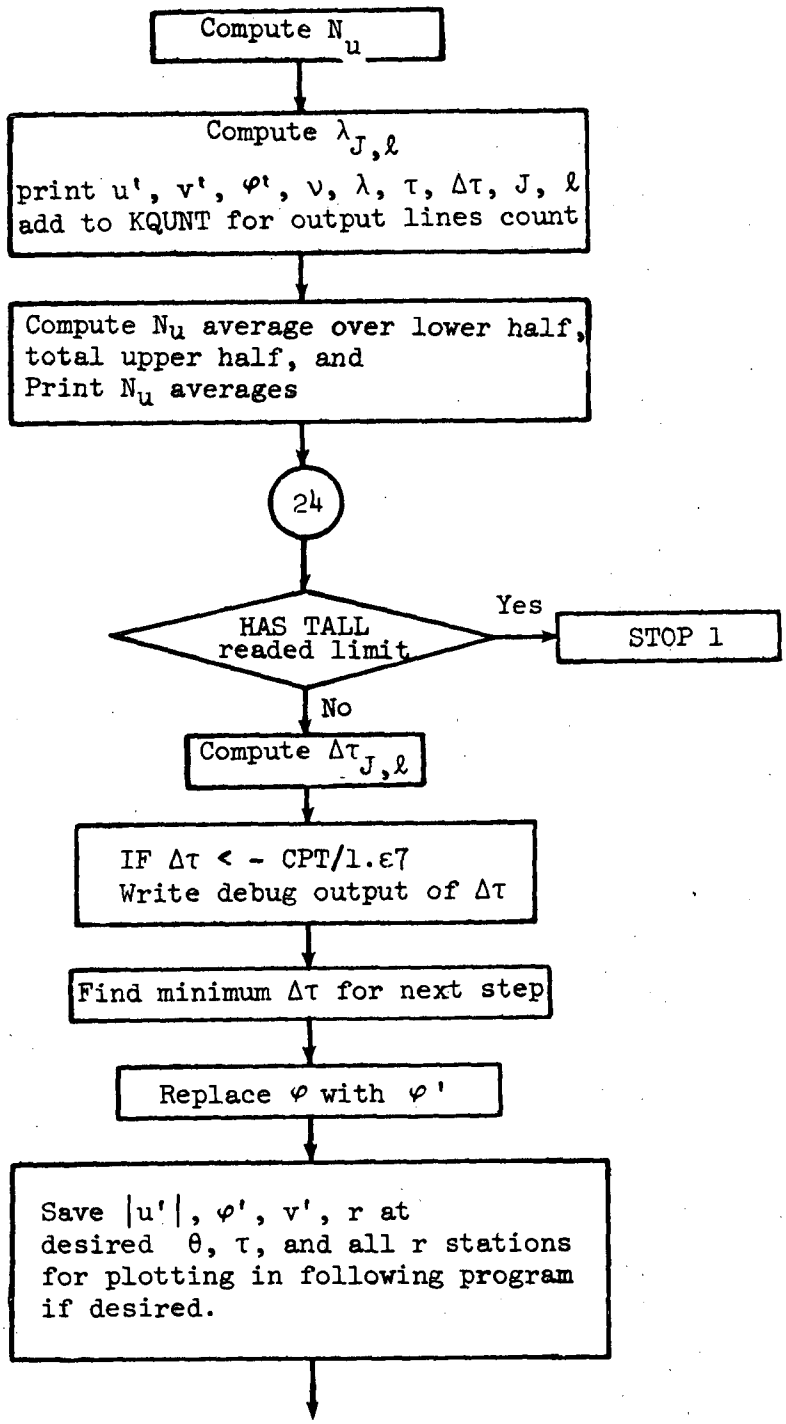

Figure 3-c.- (Continued).

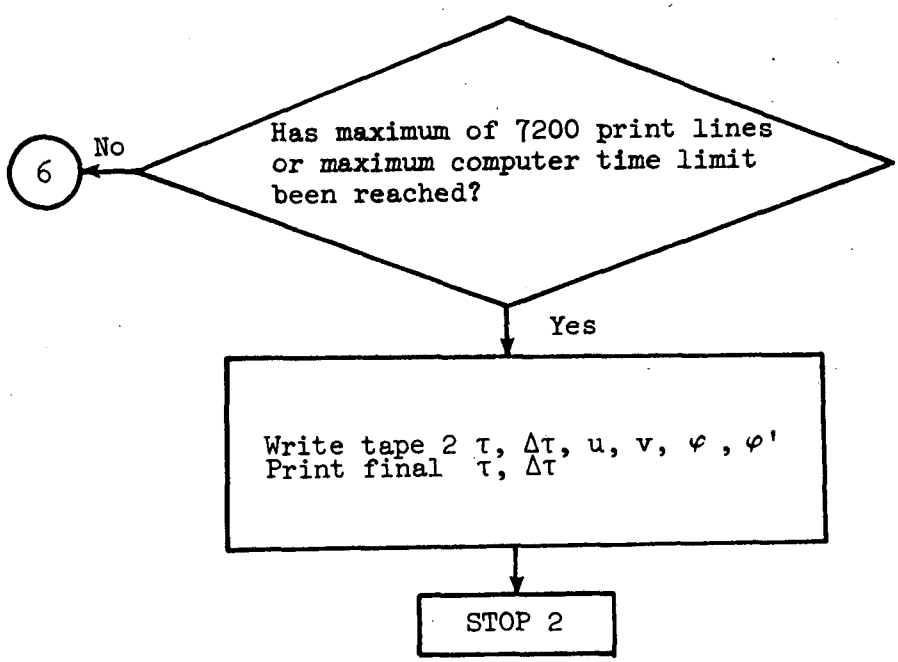

Figure 3-d.- (Concluded).

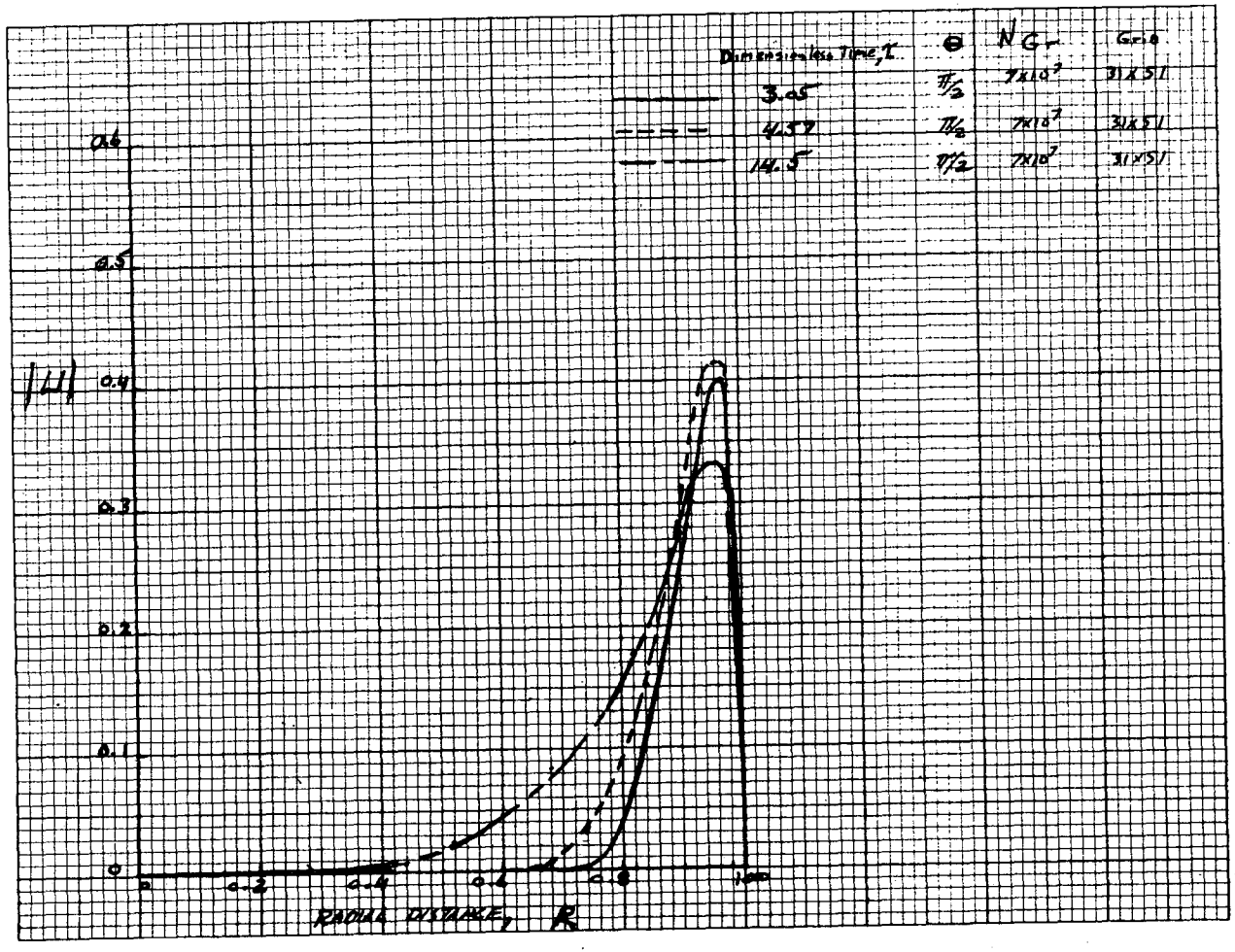

Figure 4a.- Azimuthal velocity variation with radial distance.

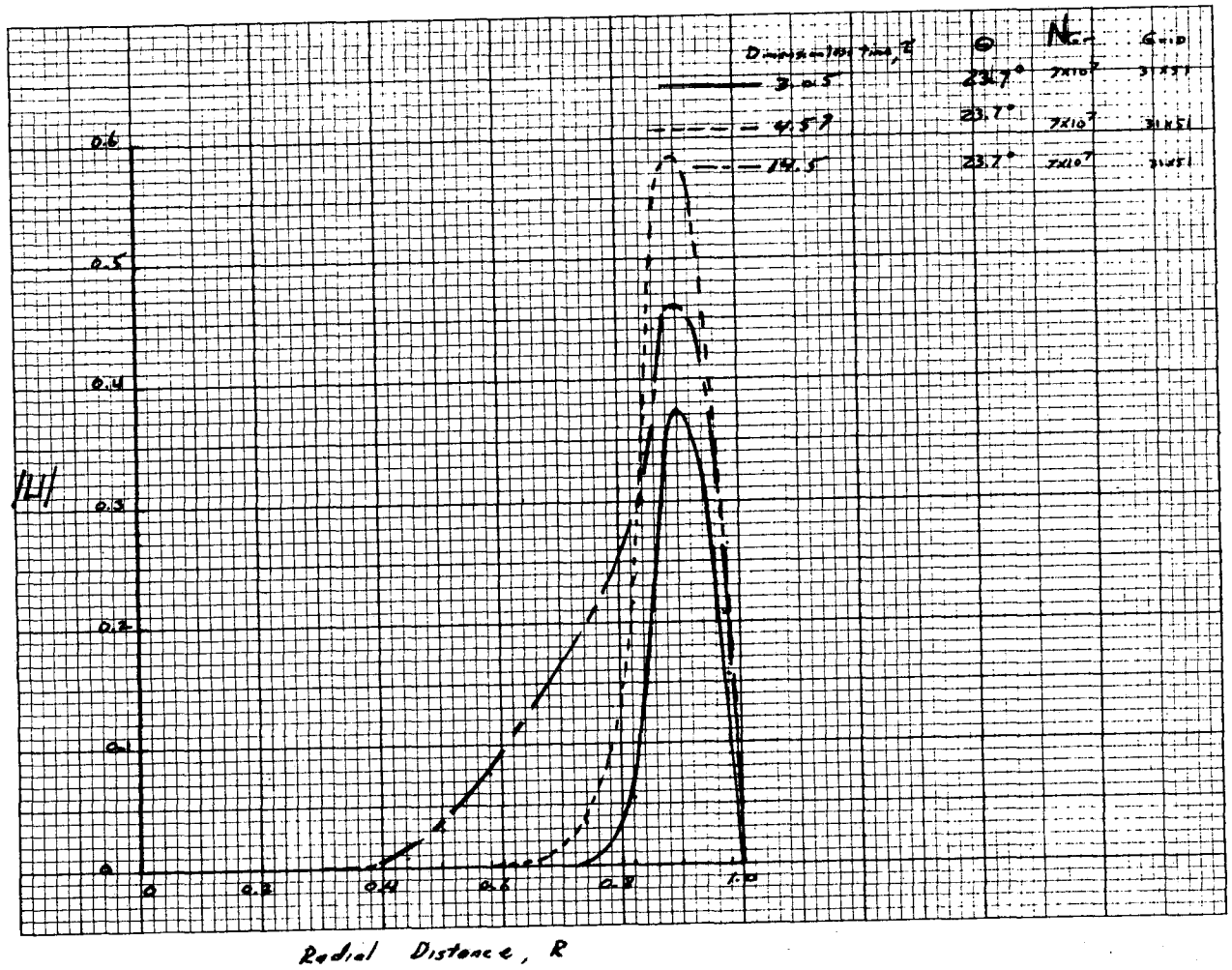

Figure 4-b.- (Continued).

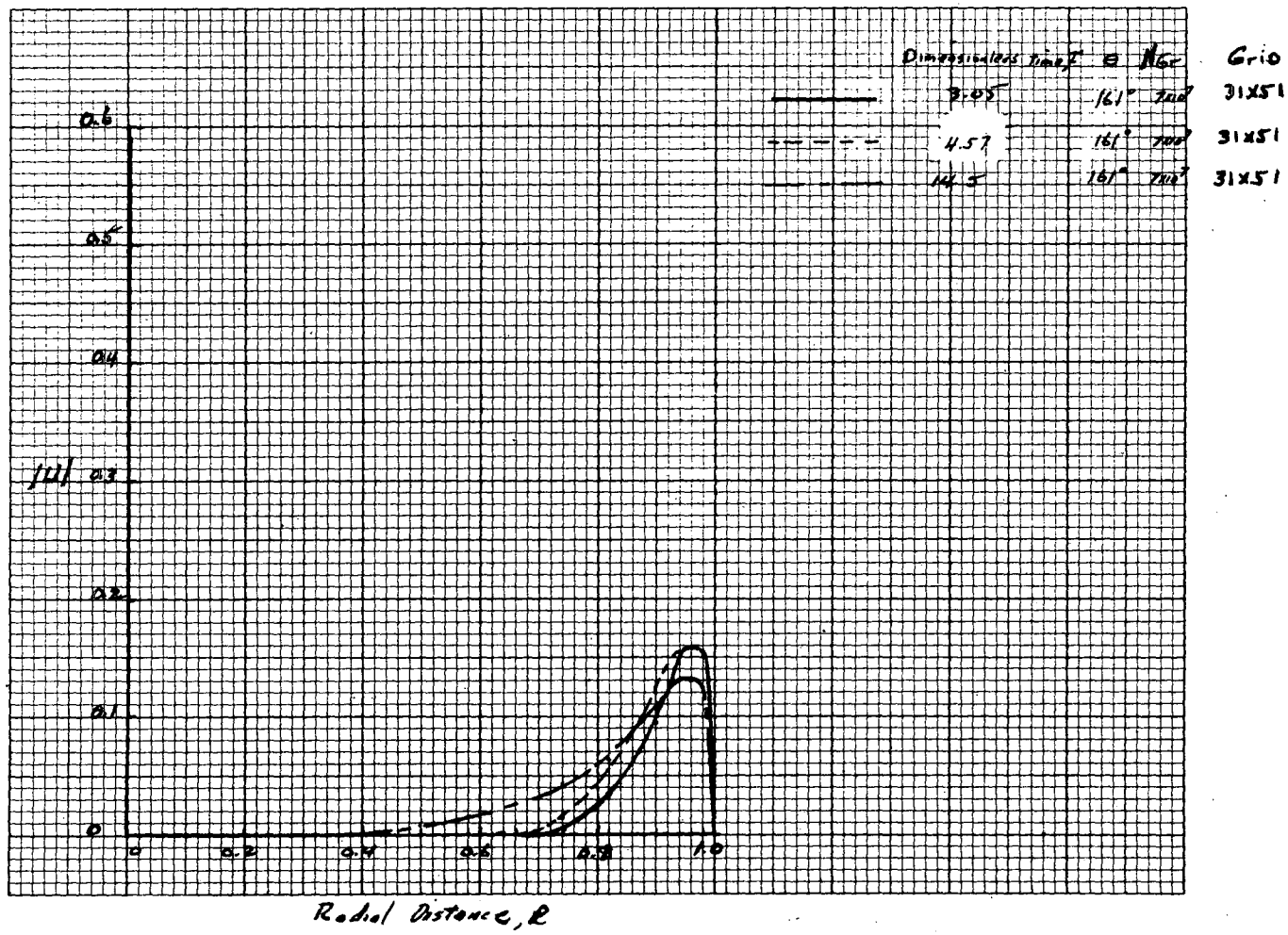

Figure 4-c.- (Concluded).

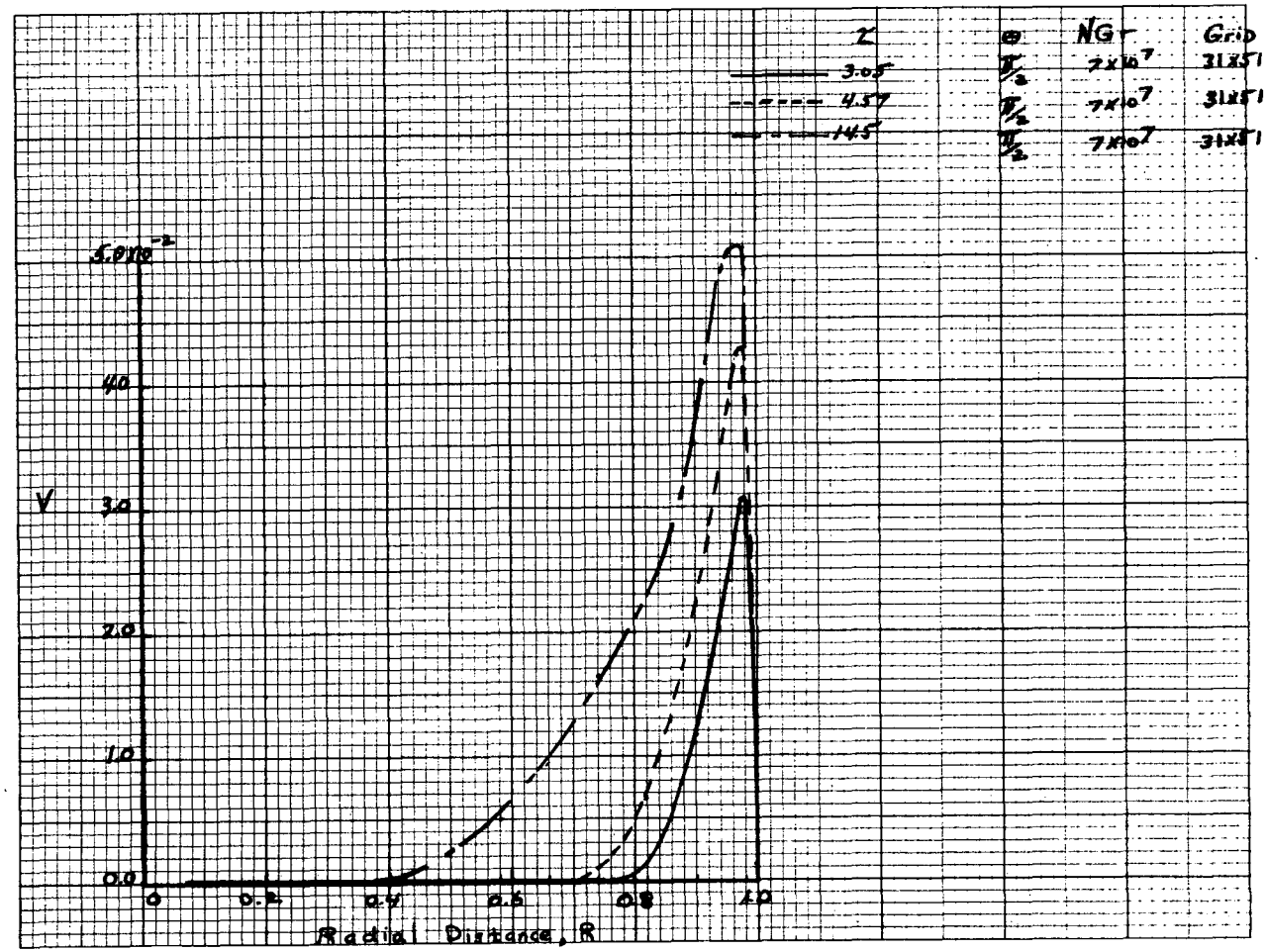

Figure 5a.- Radial velocity variation with radial distance.

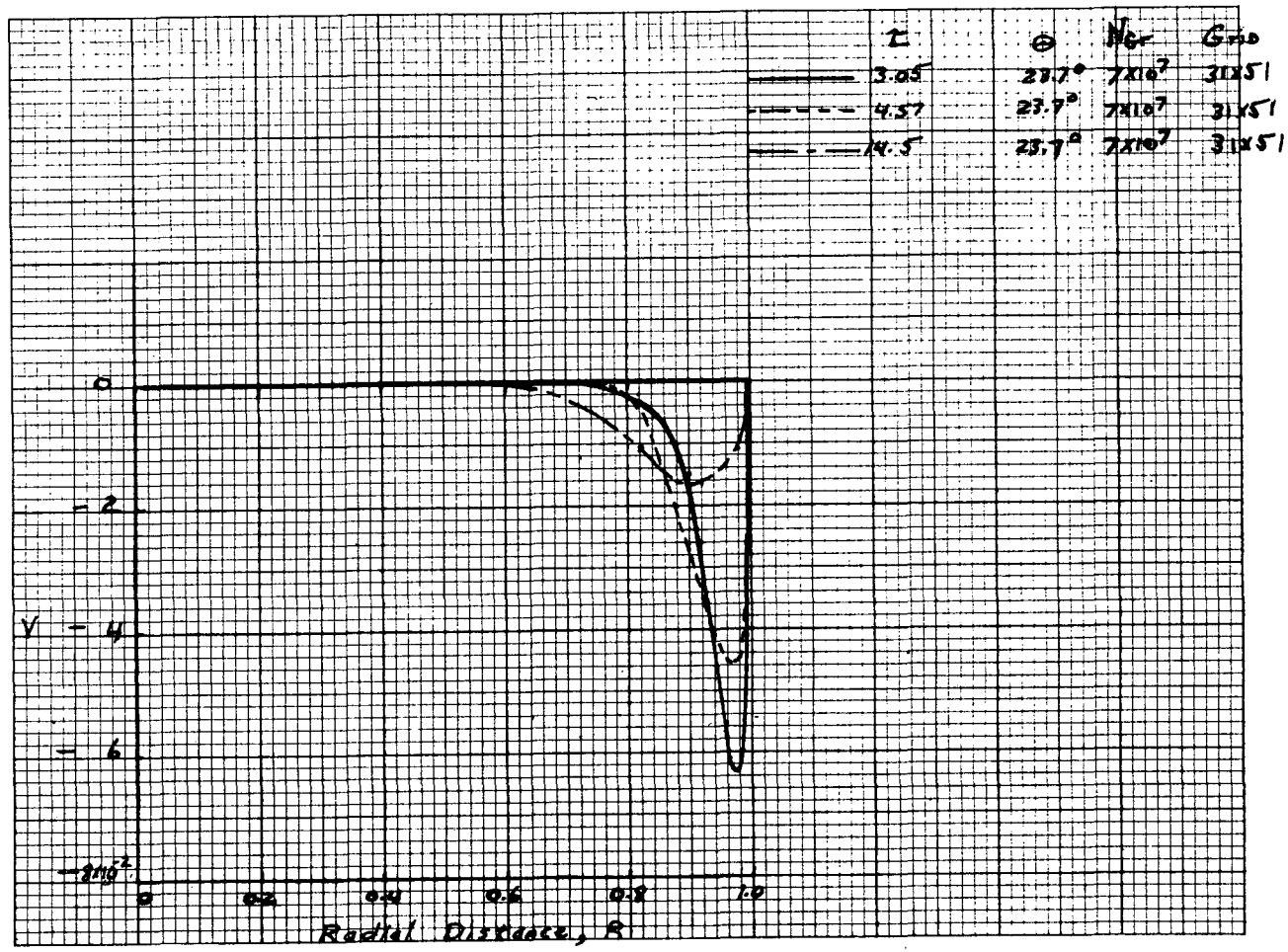

Figure 5b.- (Continued).

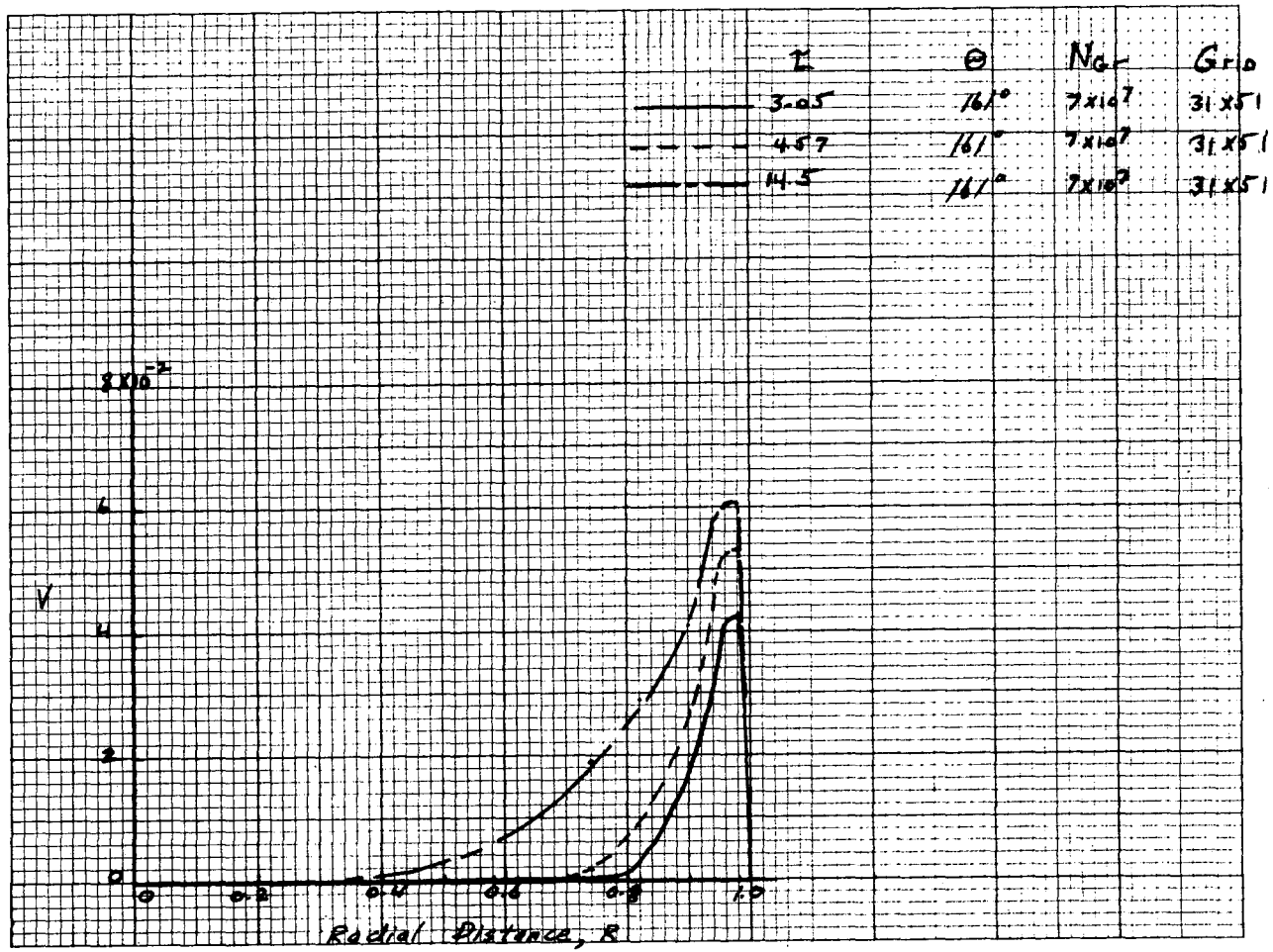

Figure 5c.- (Continued)

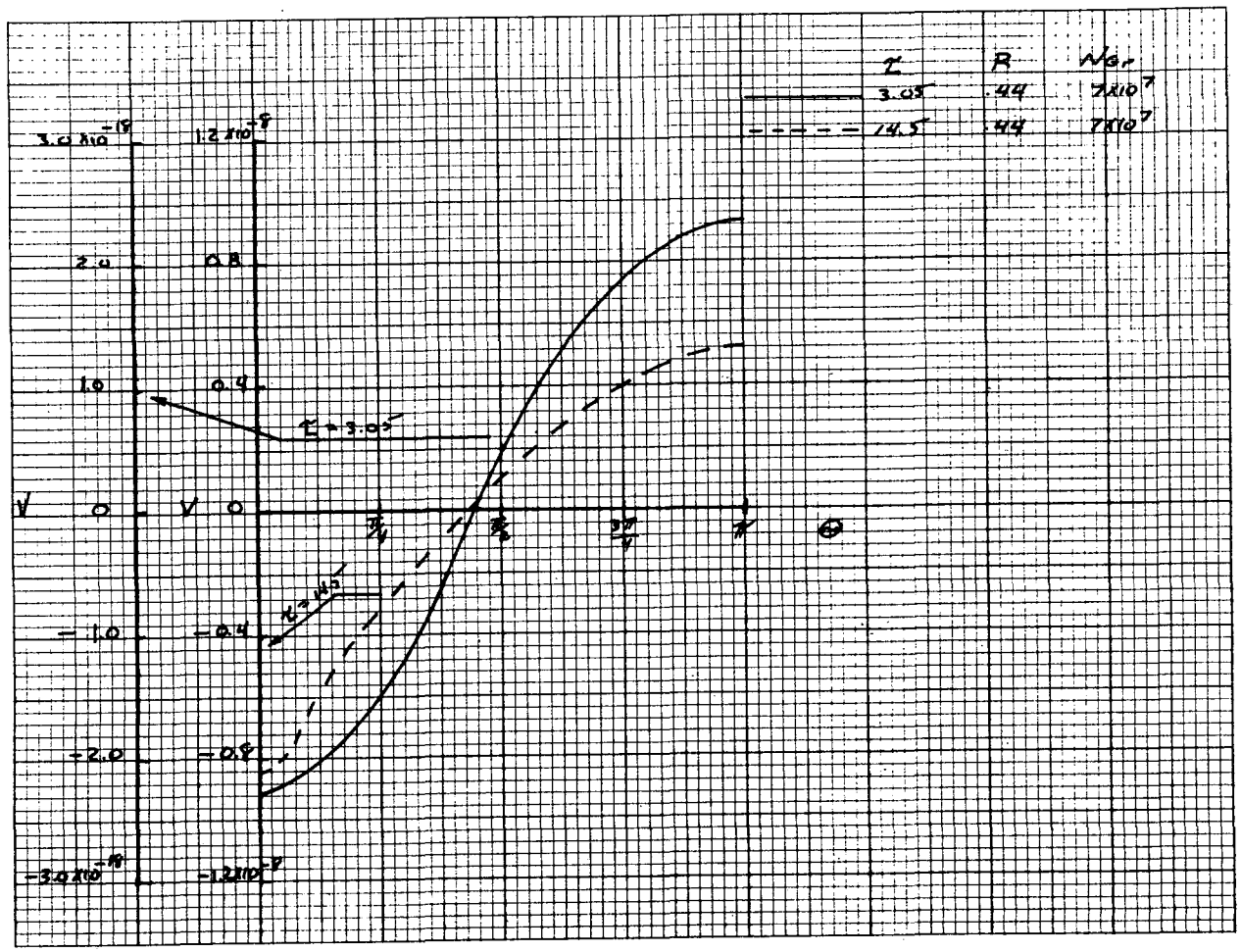

Figure 5d.- (Concluded)

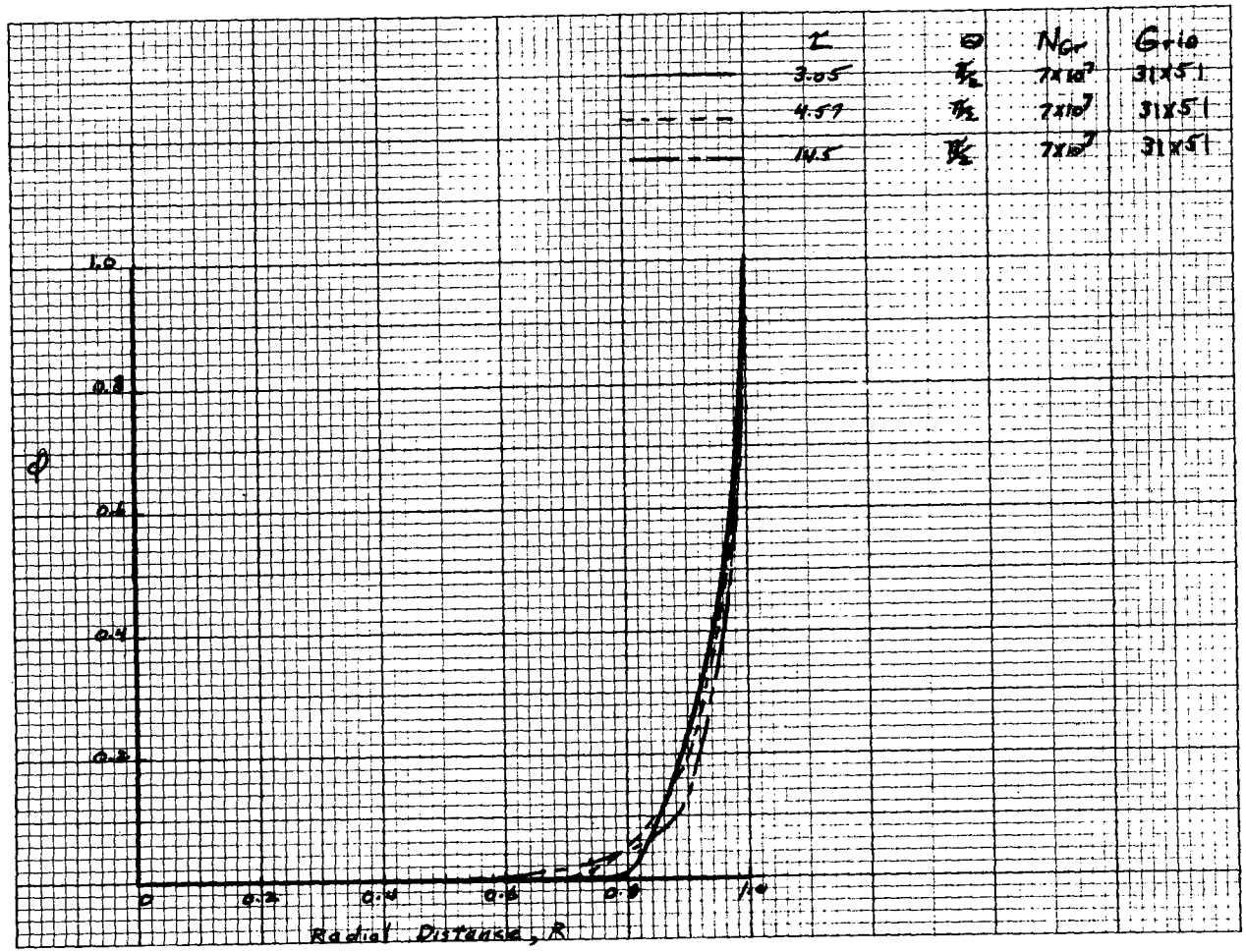

Figure 6a.- Temperature variation with radial distance.

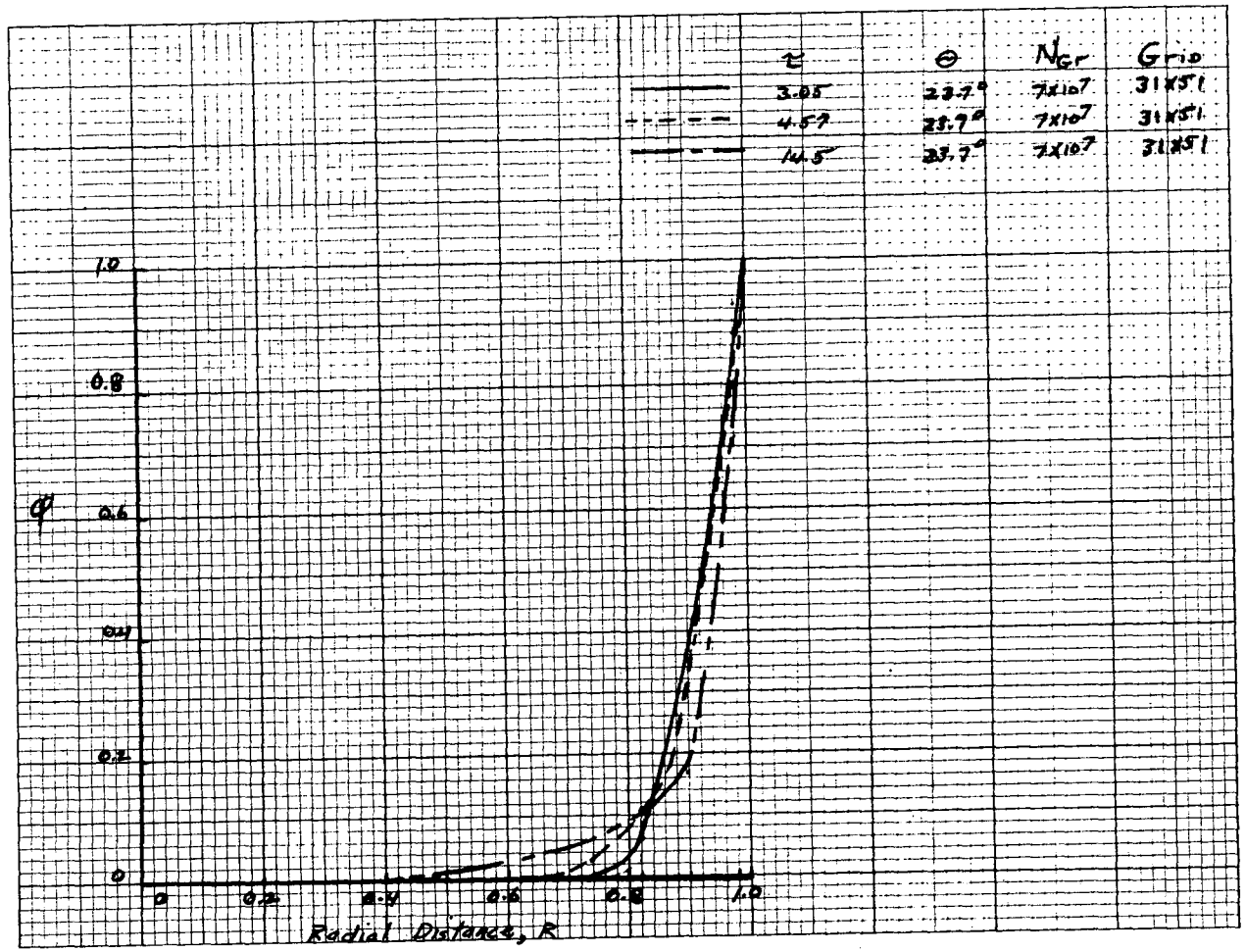

Figure 6b.- Temperature variation with radial distance.

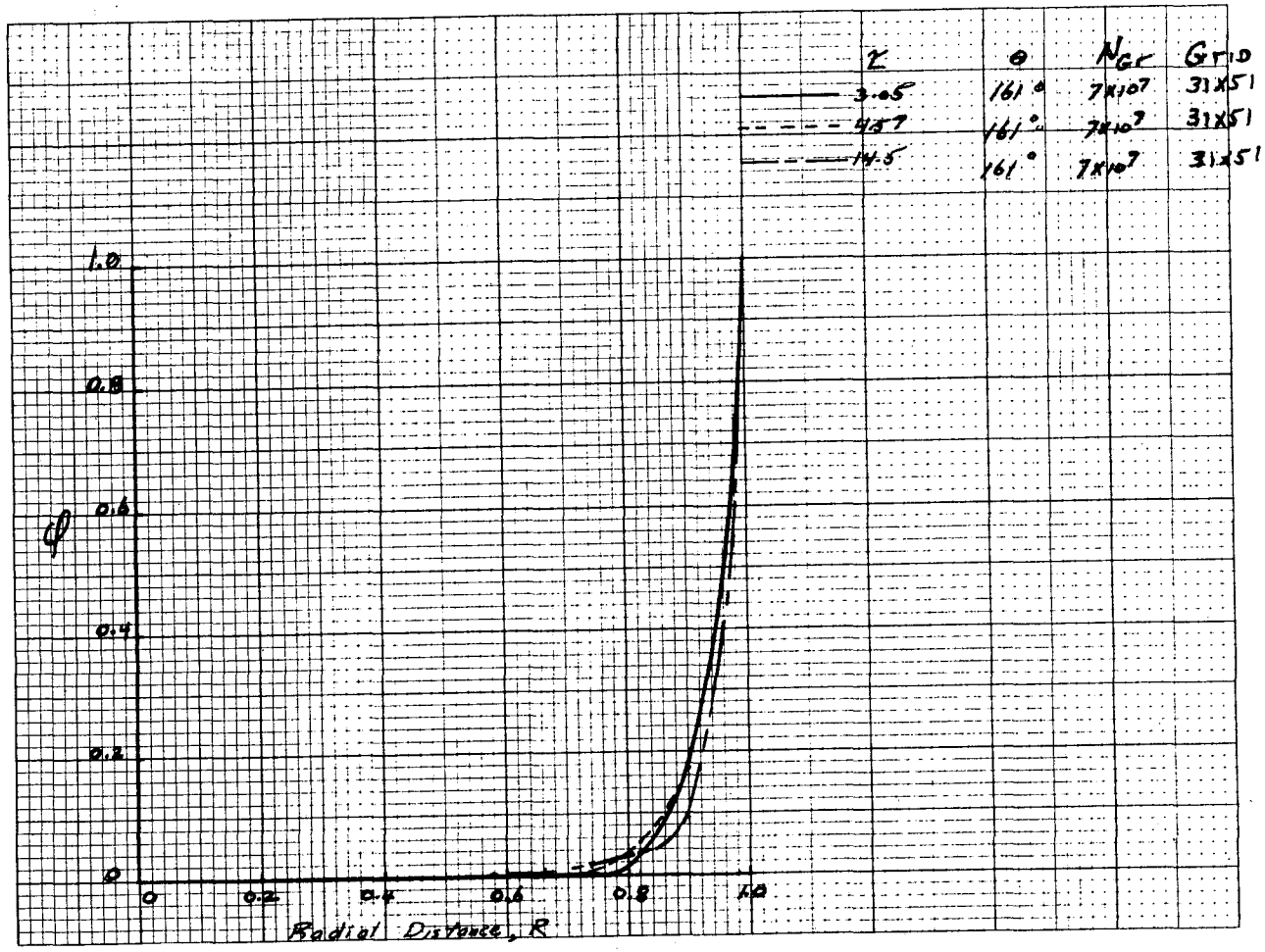

Figure 6c.- Temperature variation with radial distance.

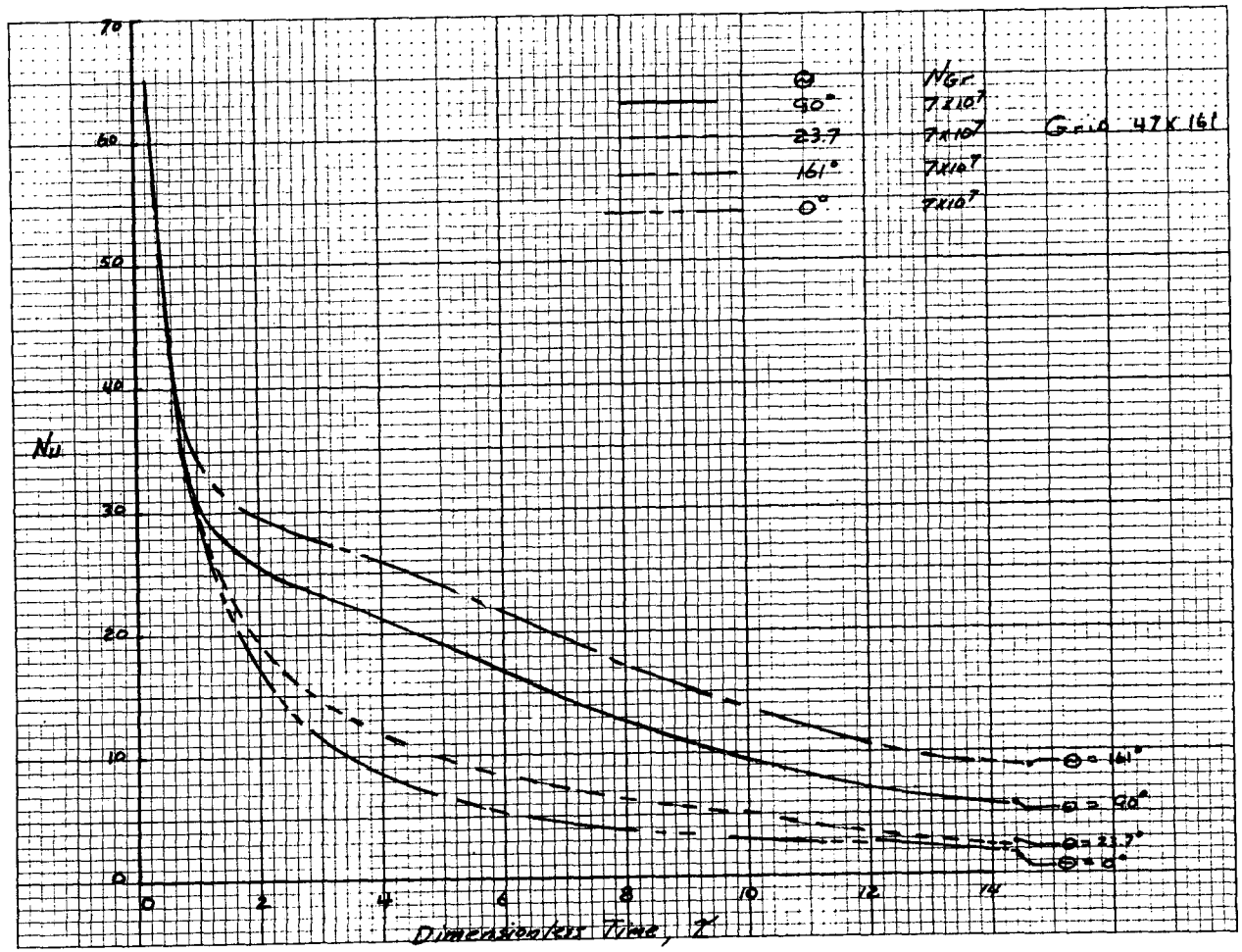

Figure 7.- Wall heat transfer decay with time.

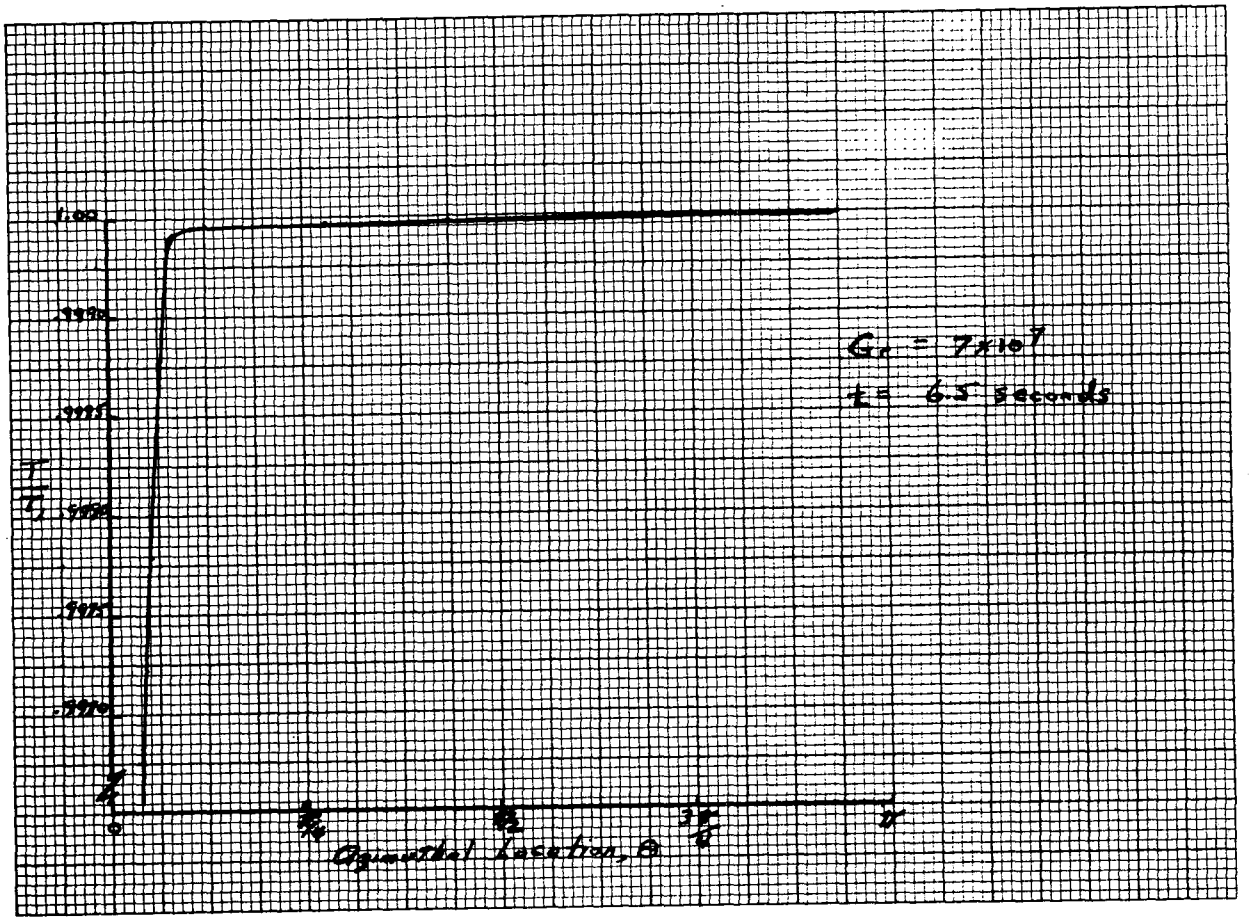

Figure 8.- Azimuthal temperature distribution within the core.

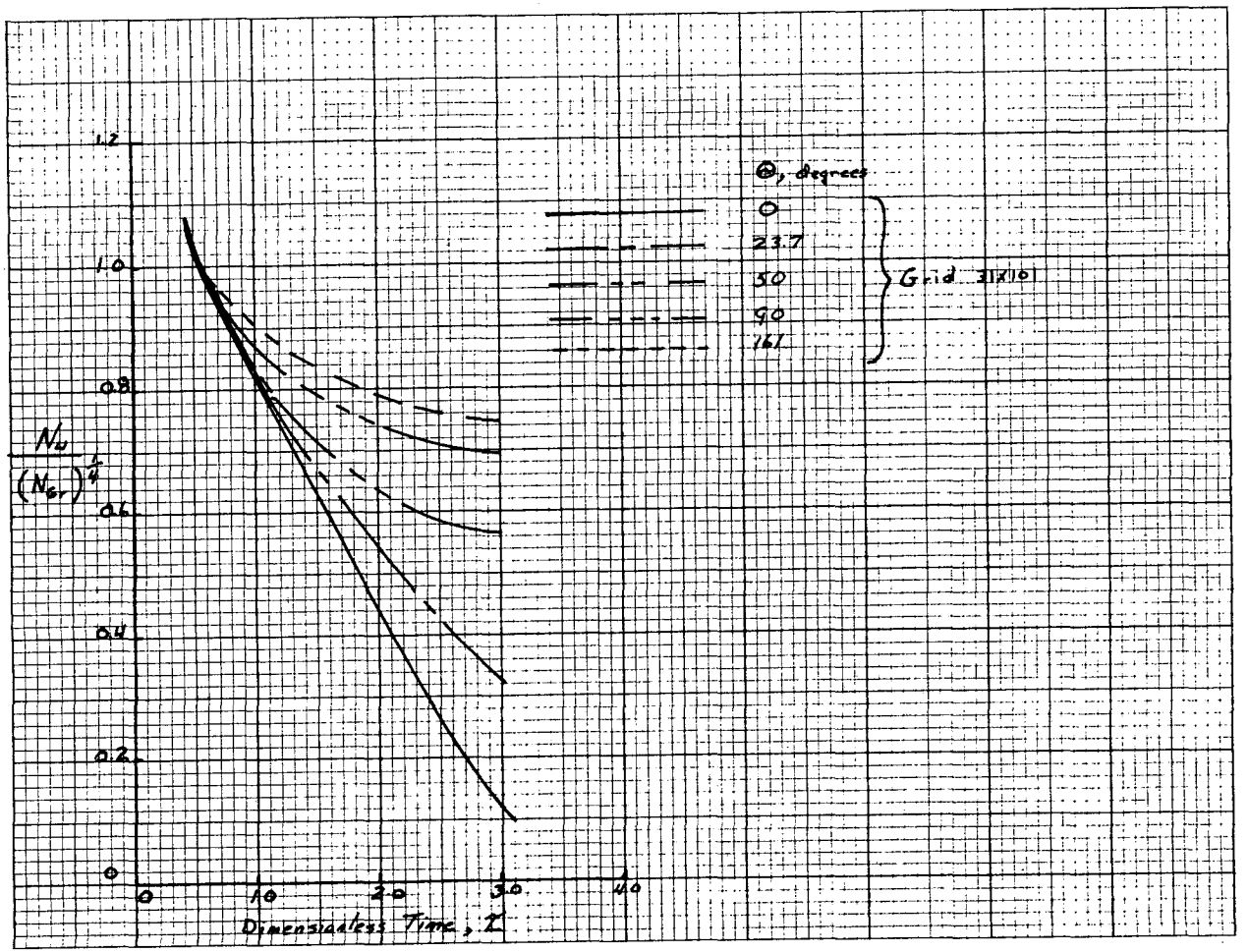

Figure 9.- The Nusselt-Grashof relation for a time dependent natural convection flow.

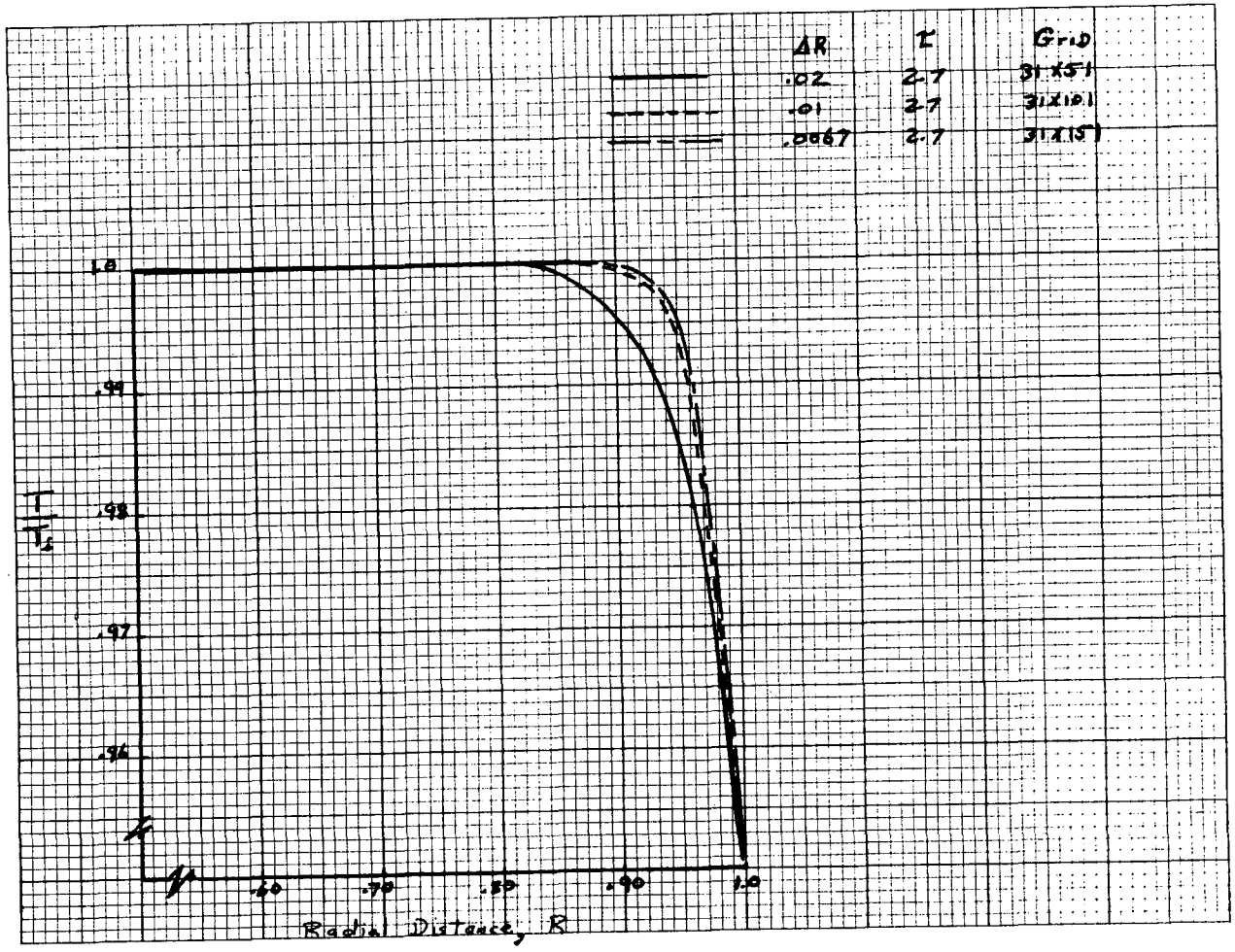

Figure 10a.- Radial grid refinement effects for a Grashof number of 1.3×10^6.

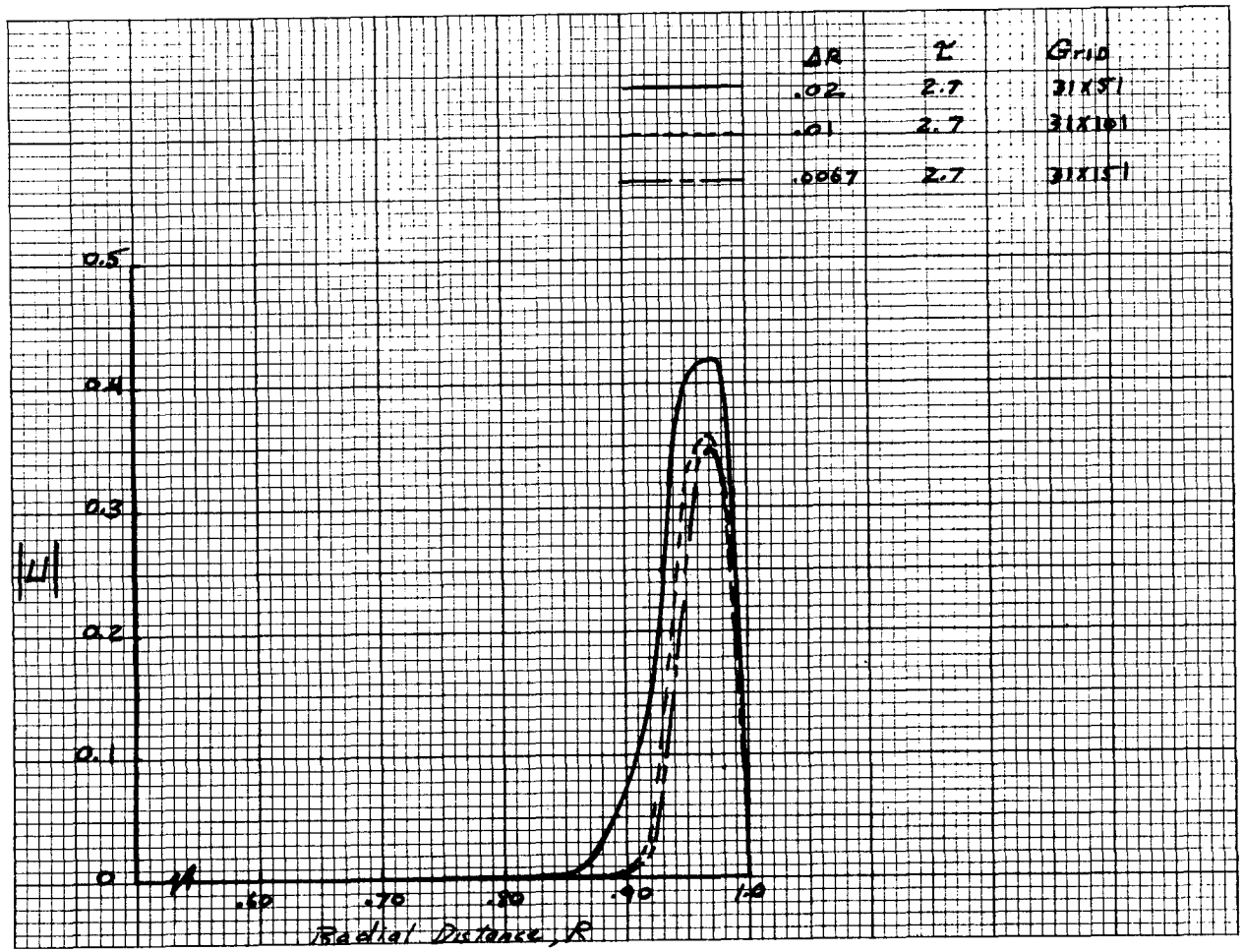

Figure 10b.- Radial grid refinement effects at a Grashof number 1.

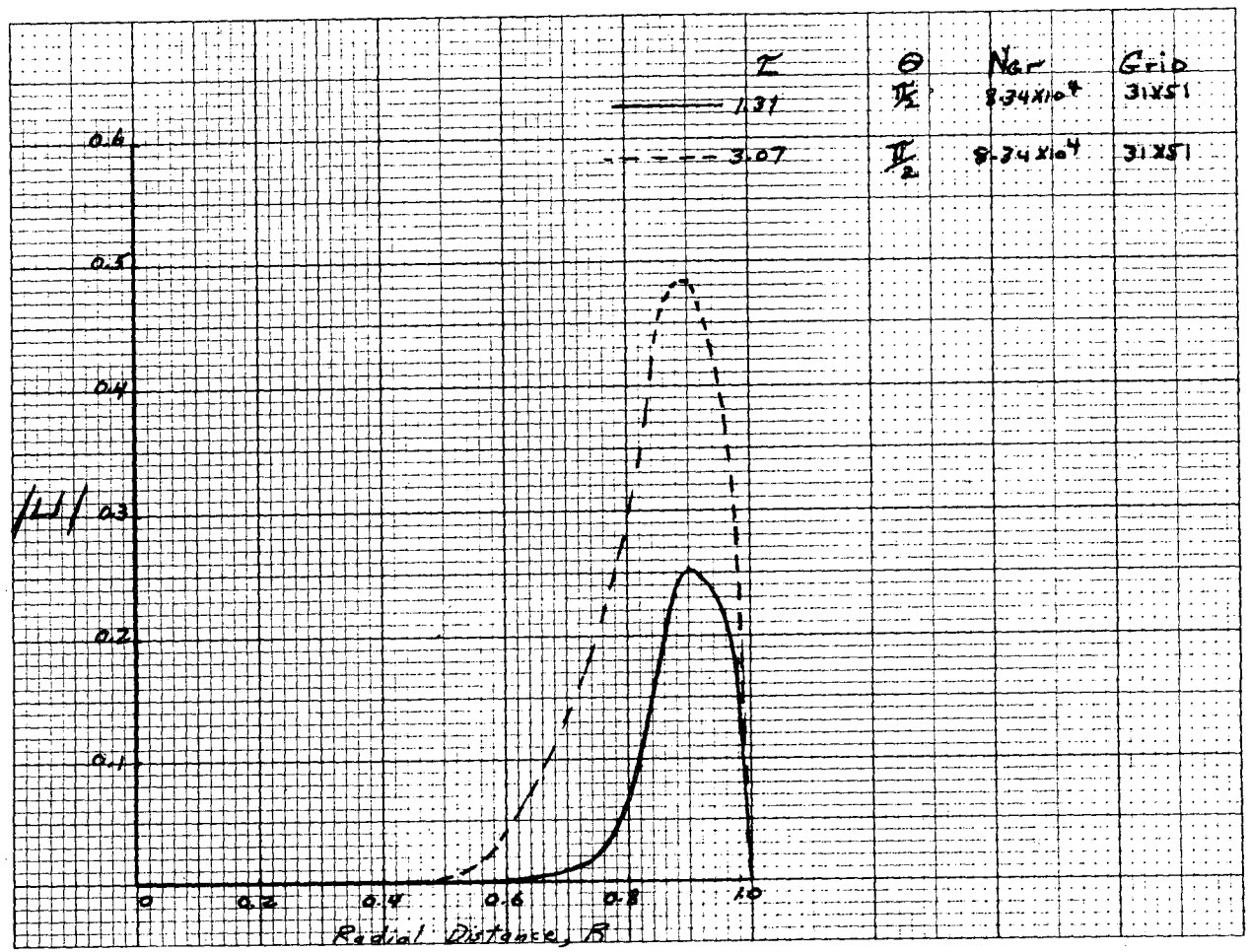

Figure 11a.- Azimuthal velocity distribution for natural convection flow at low Grashof number.

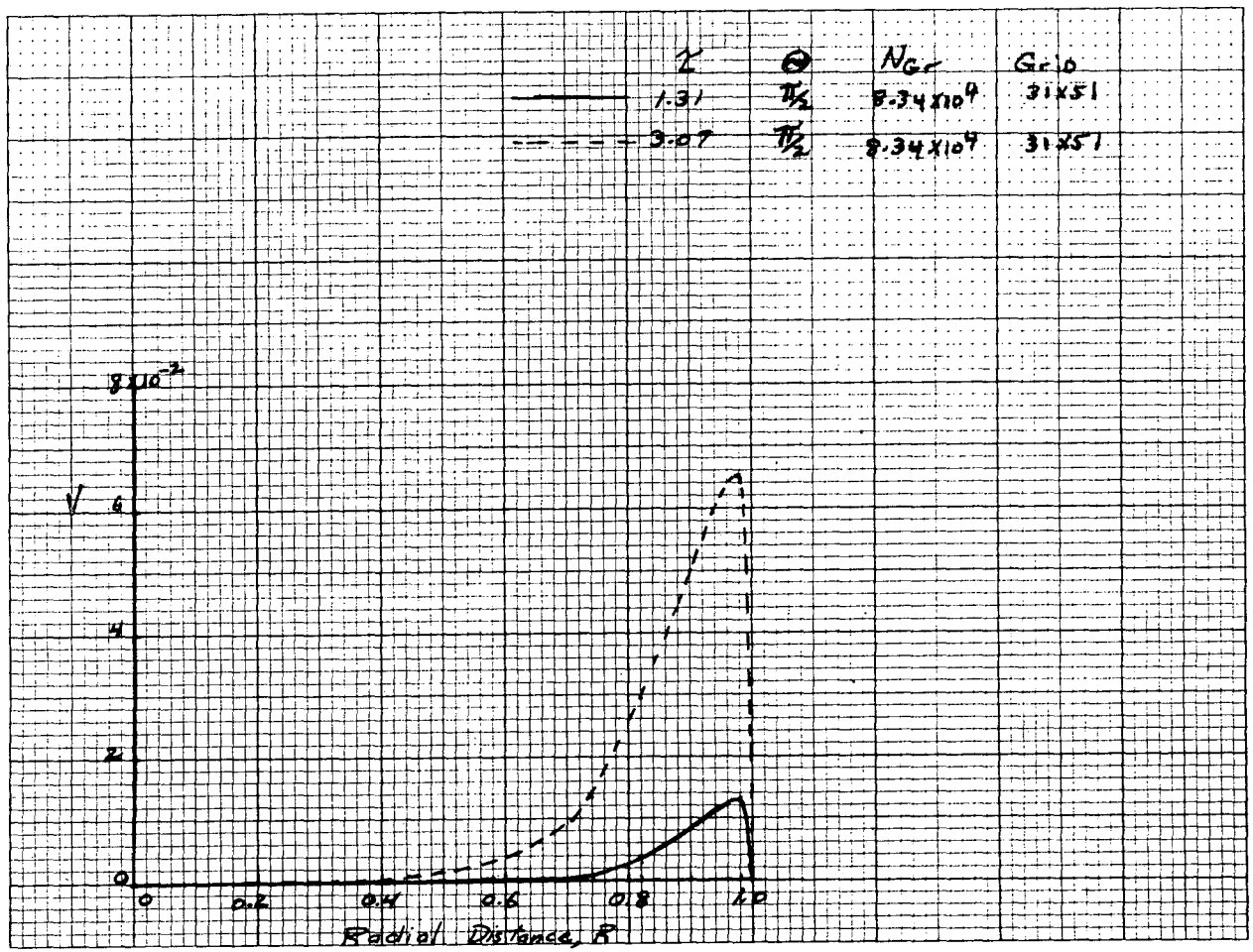

Figure 11b.- Radial velocity distribution.

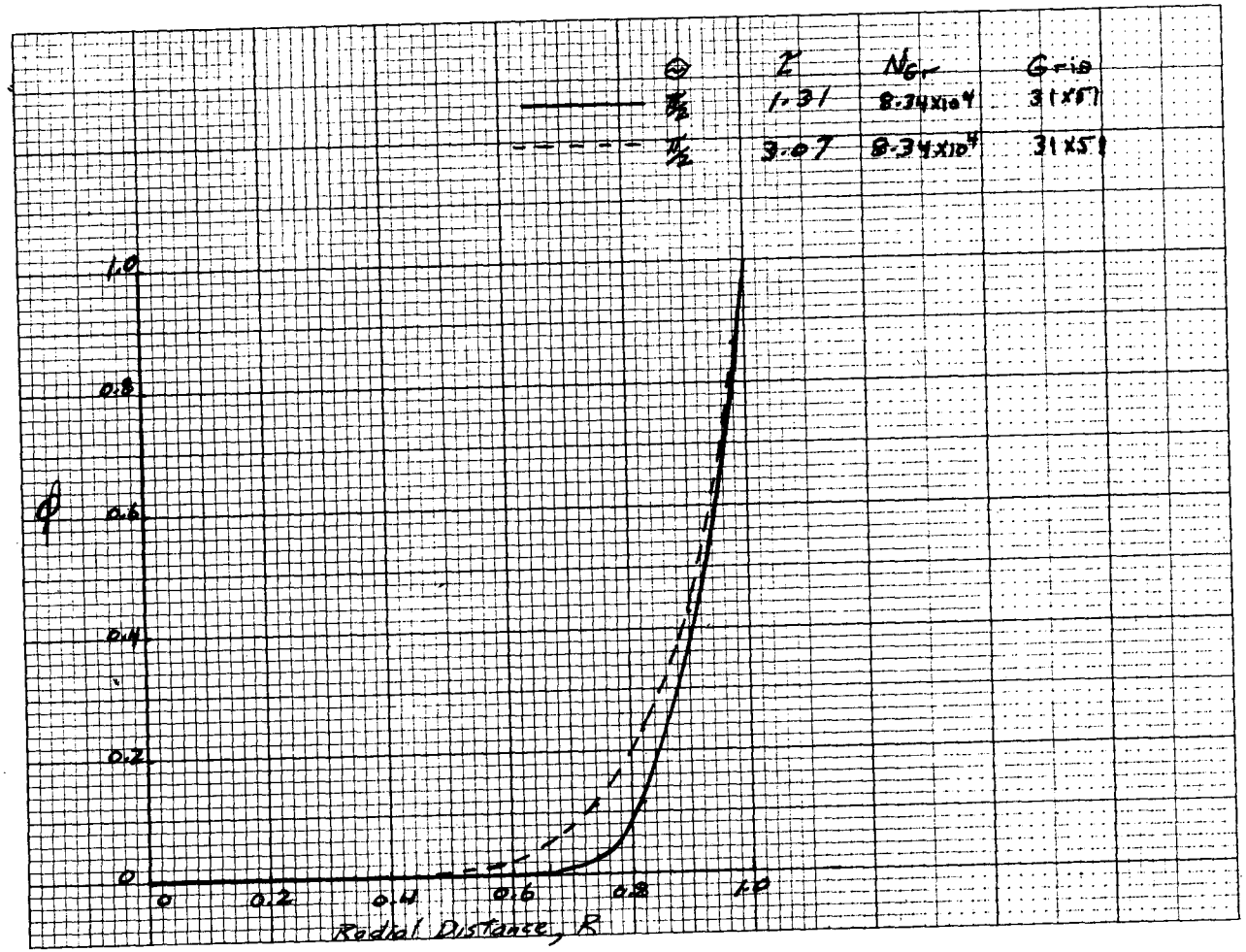

Figure 11c.- Temperature distribution.

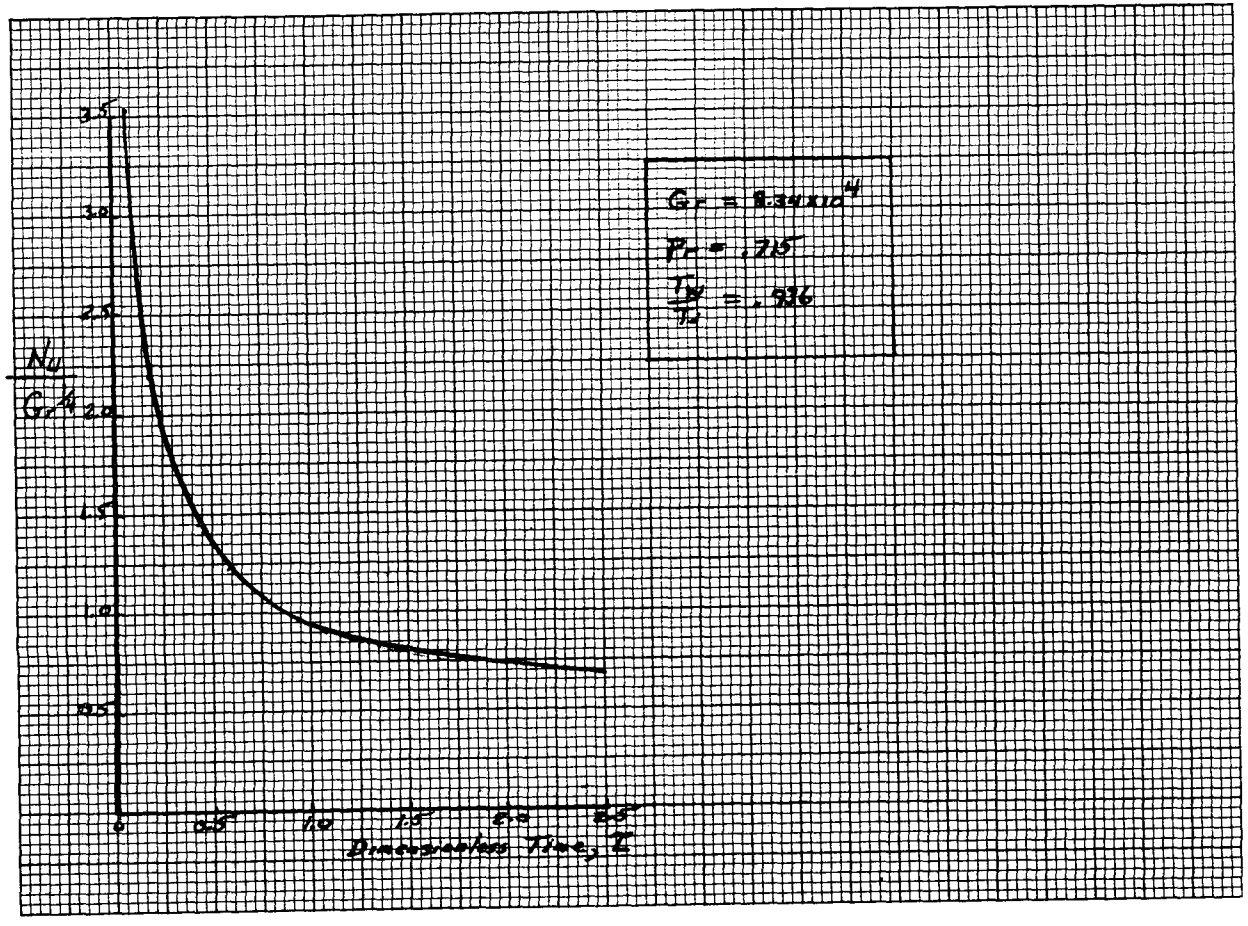

Figure 11d.- Nusselt-Grashof relation for low Grashof numbers natural convection flow within a horizontal cylinder.

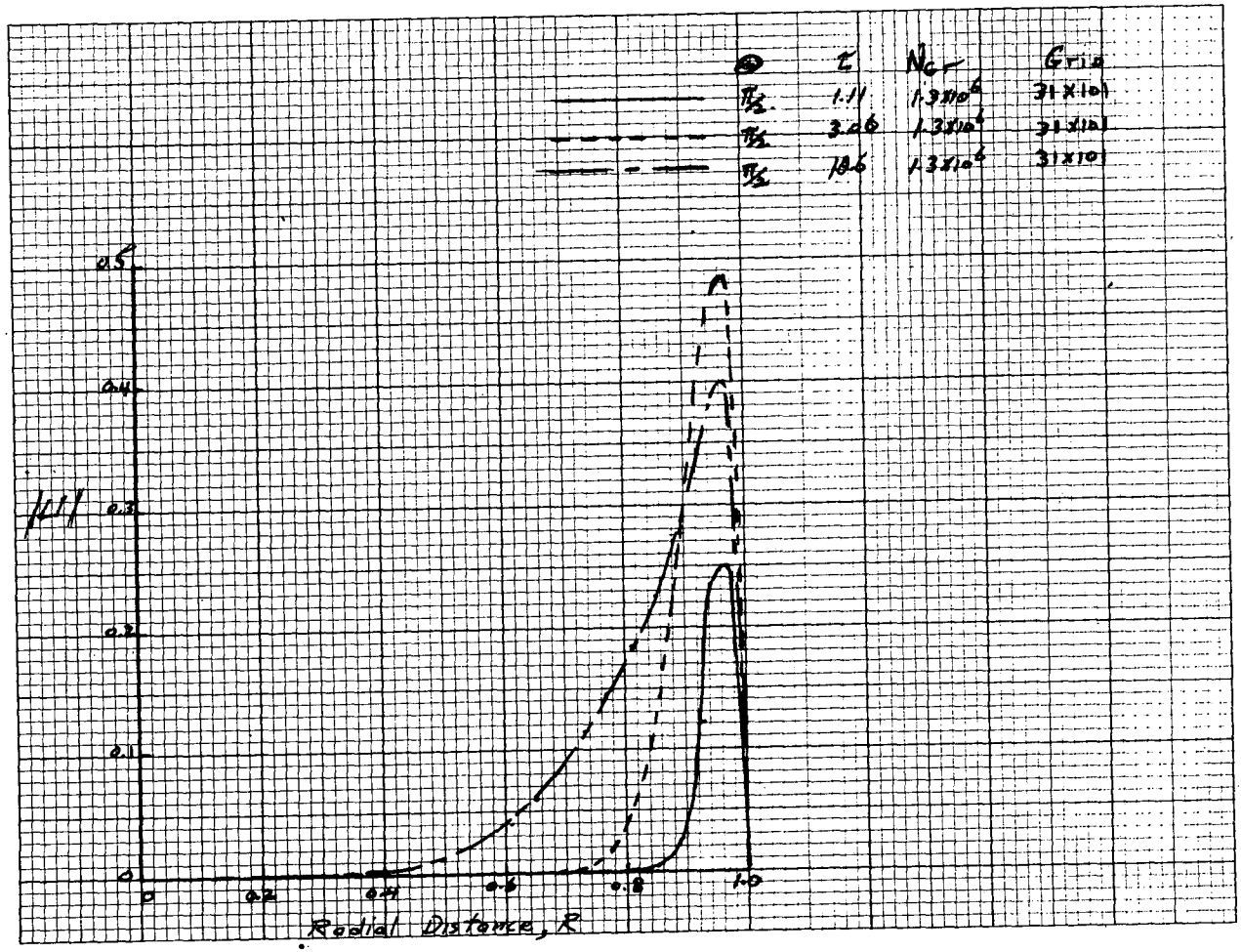

Figure 12.- Azimuthal velocity distribution in horizontal cylinder.

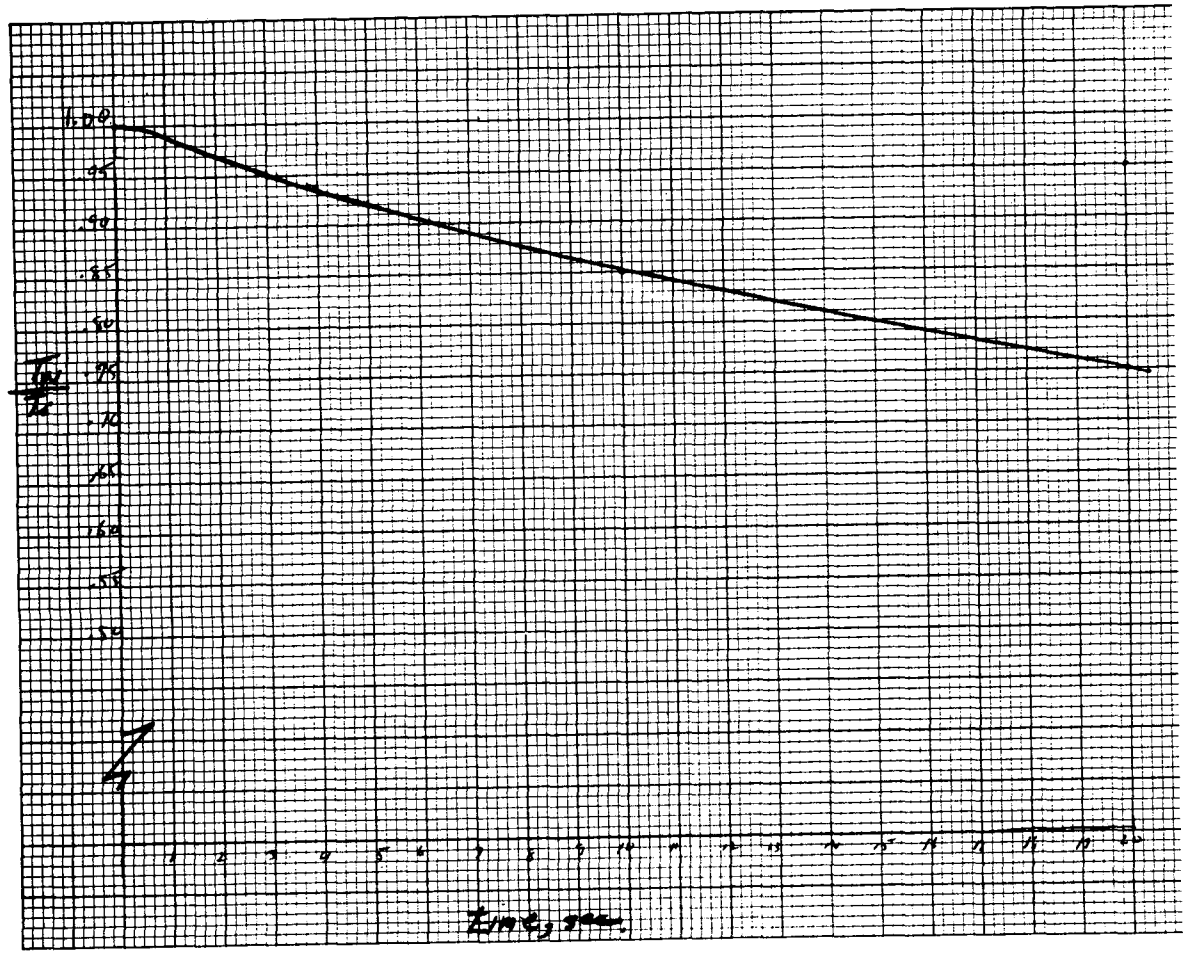

Figure 13.- Wall temperature decay from the heat conduction equation.

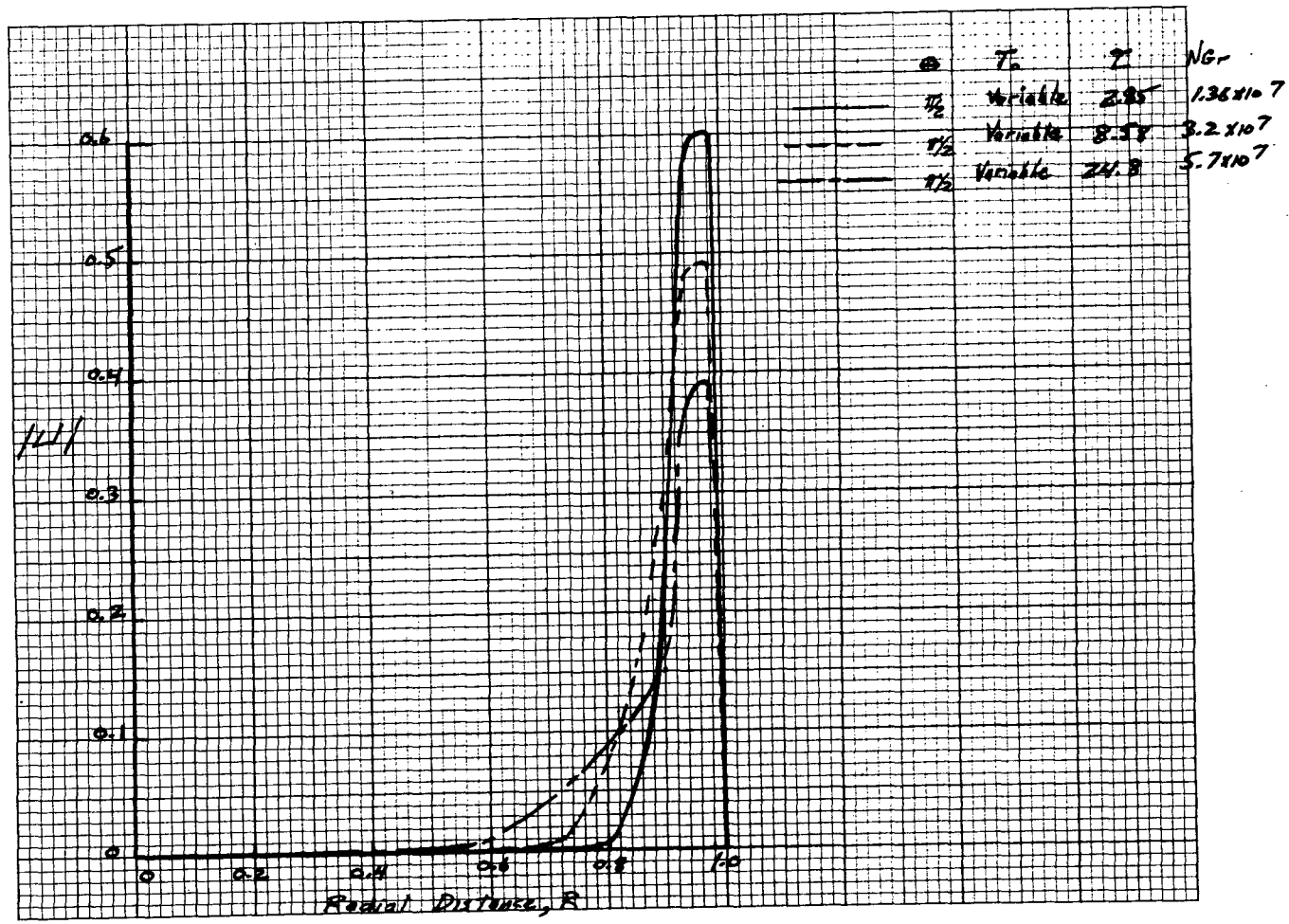

Figure 14.- Azimuthal velocity distribution for time dependent wall temperature.

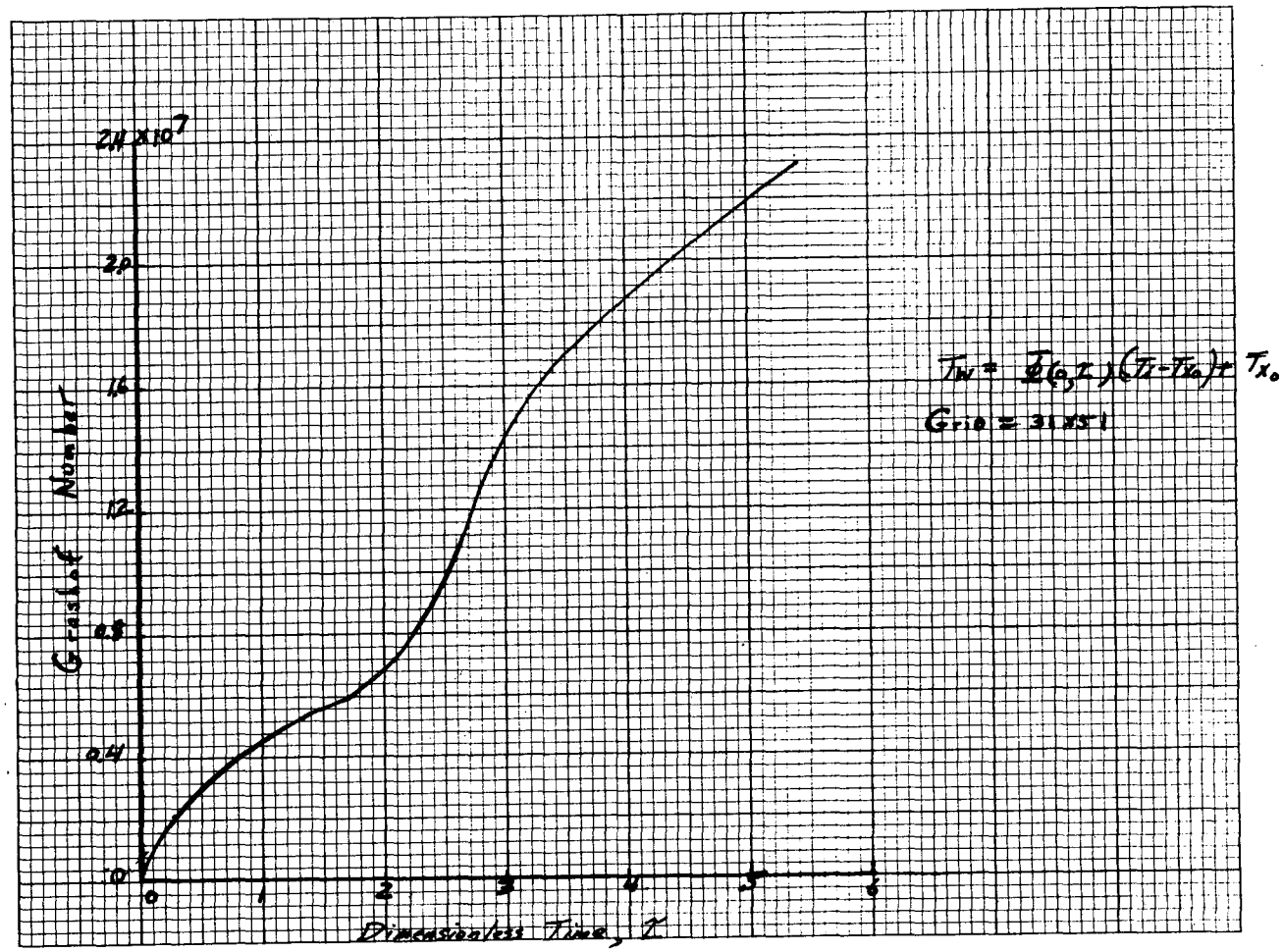

Figure 15.- Time development of the Grashof number for unsteady wall temperature.

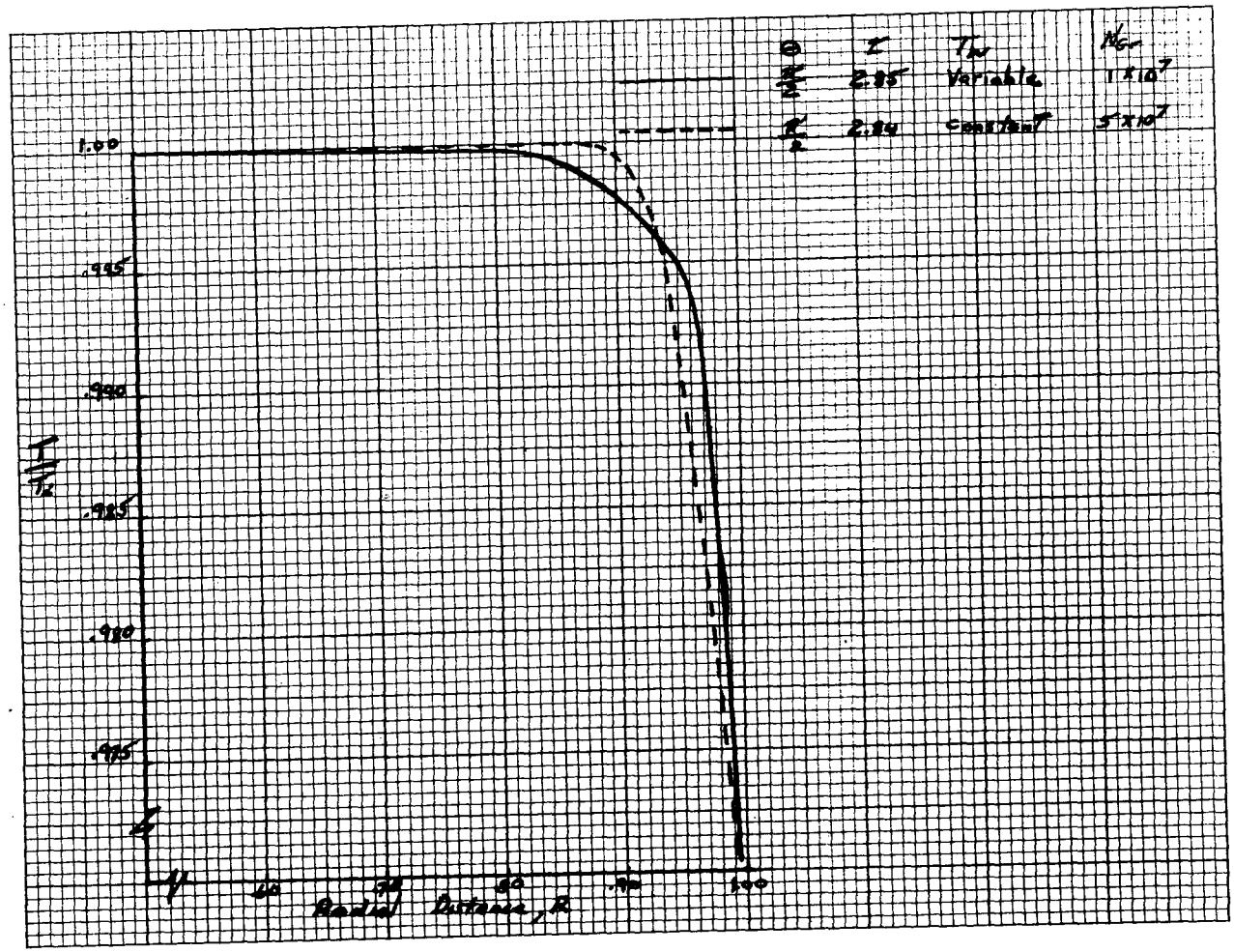

Figure 16a.- Temperature distributions for a time dependent wall temperature.

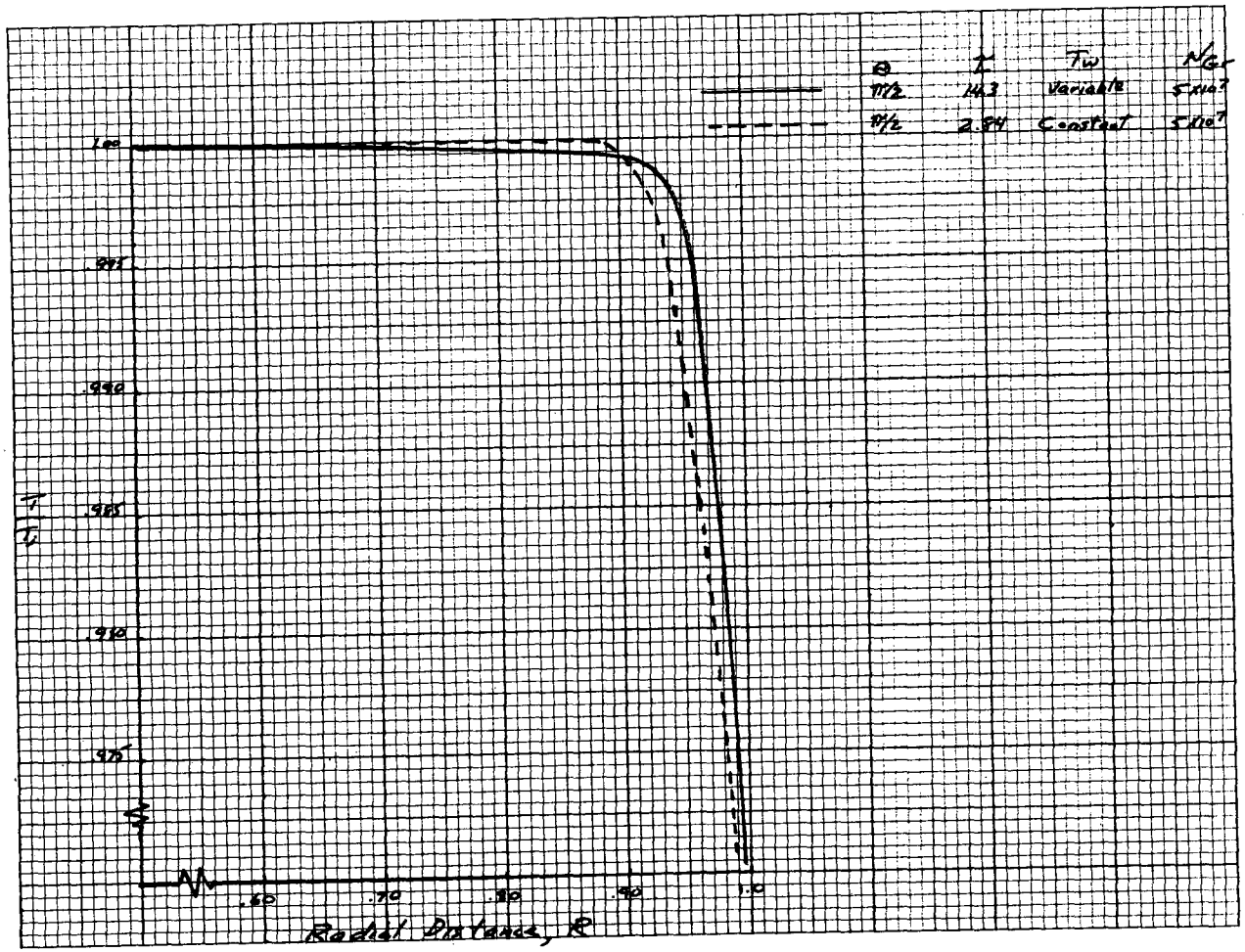

Figure 16b.- Temperature distributions for constant and variable wall temperature boundary conditions with equal values of Grashof number.

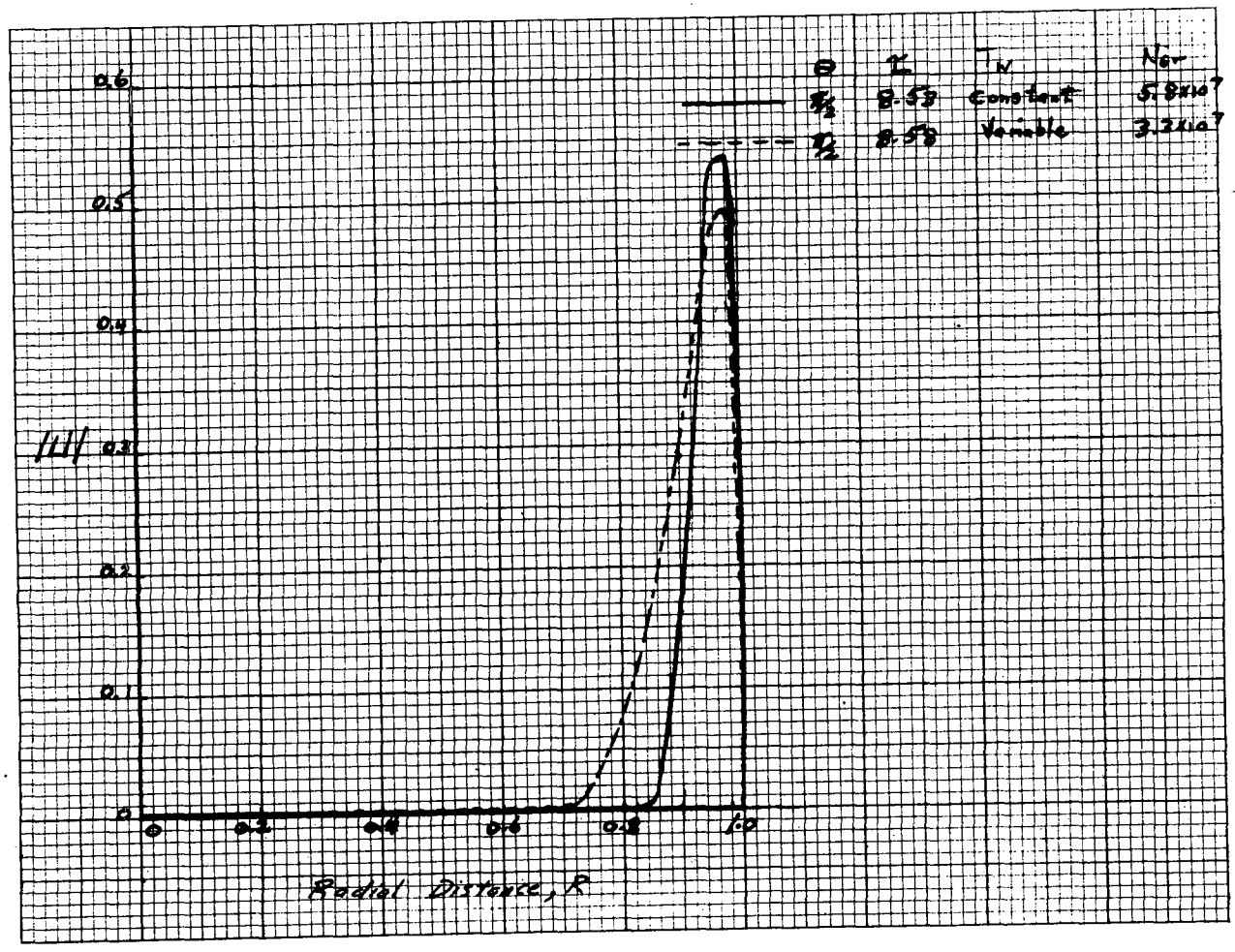

Figure 17a.- Azimuthal velocity distributions for constant and variable wall temperature.

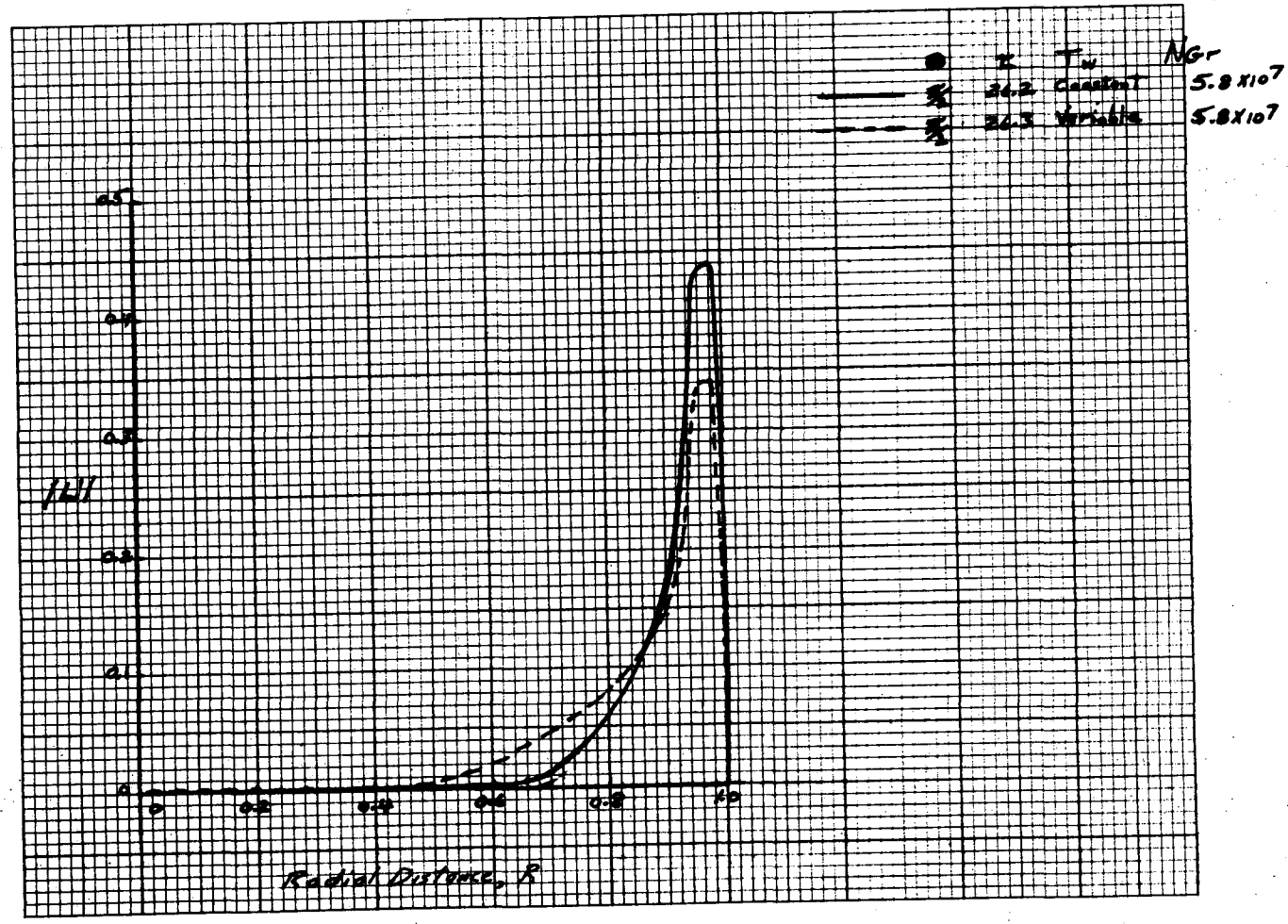

Figure 17b.- Azimuthal velocity distribution for constant and variable wall temperatures.

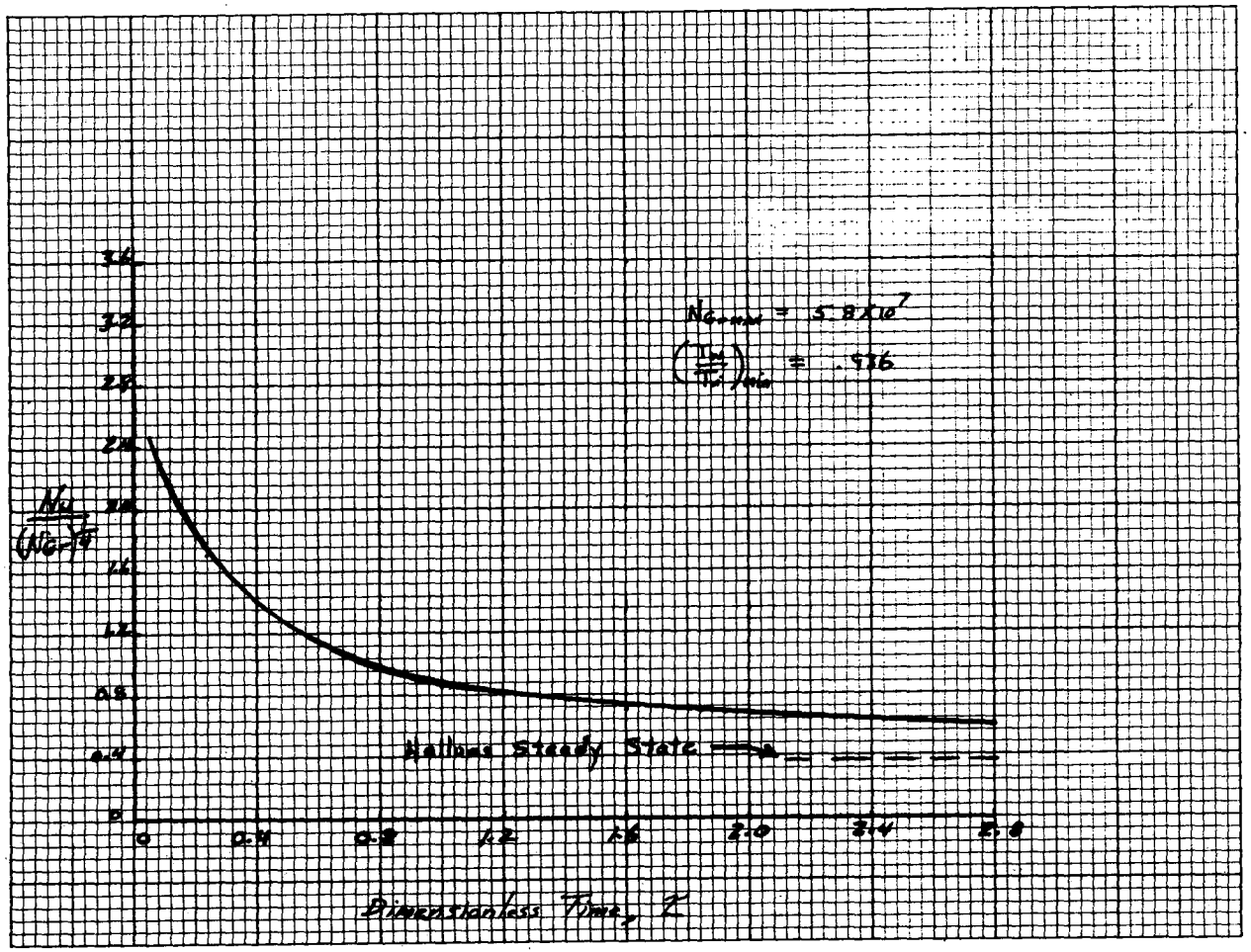

Figure 18.- Nusselt-Grashof correlation for time dependent flow within a horizontal cylinder.

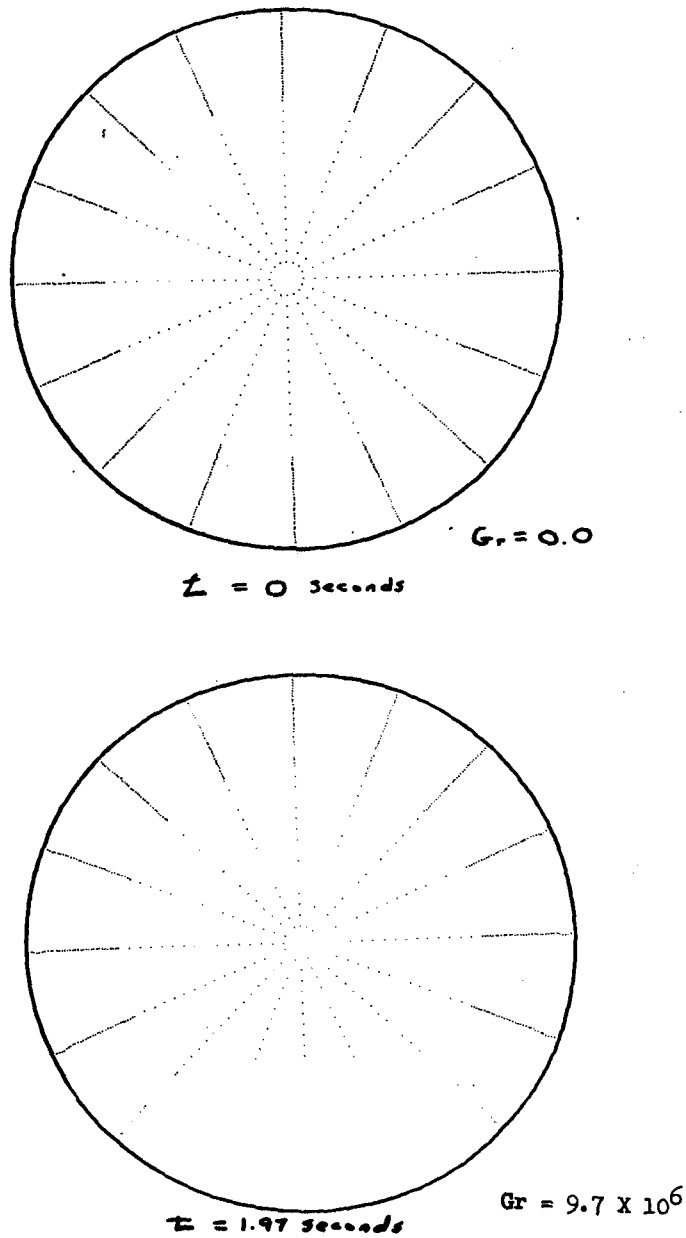

a. t=0 and t=1.97 seconds

Figure 19.- Oscilloscope photographs of fluid element displacements from the numerical solutions for natural convection flow within a horizontal cylinder.

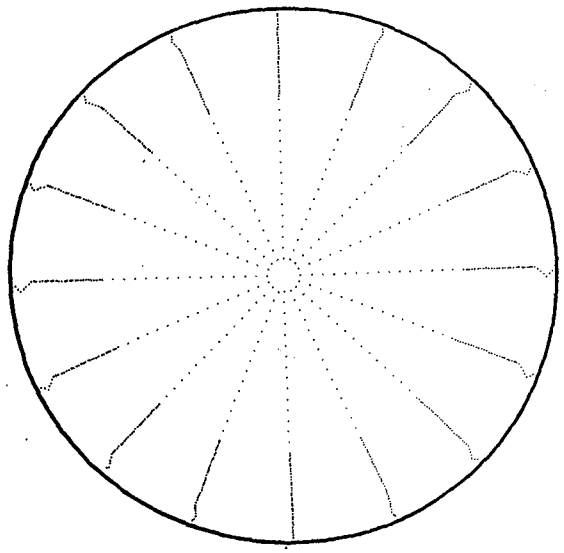

$t = 3.04$ seconds
$G_r = 1.6 \times 10^7$

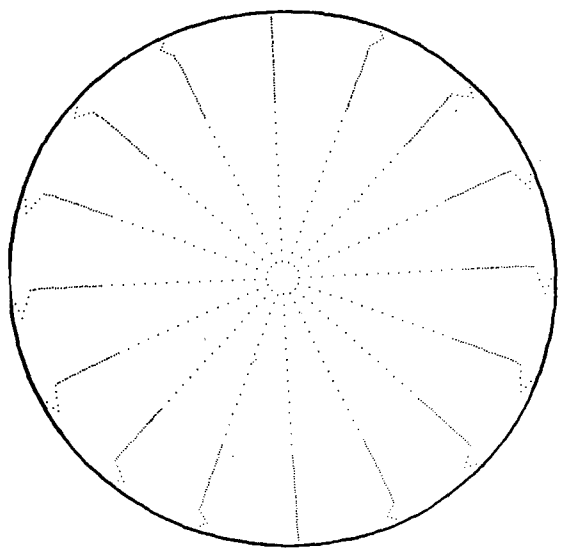

$t = 3.86$
$G_r = 2.3 \times 10^7$

Figure 19.- (Continued).

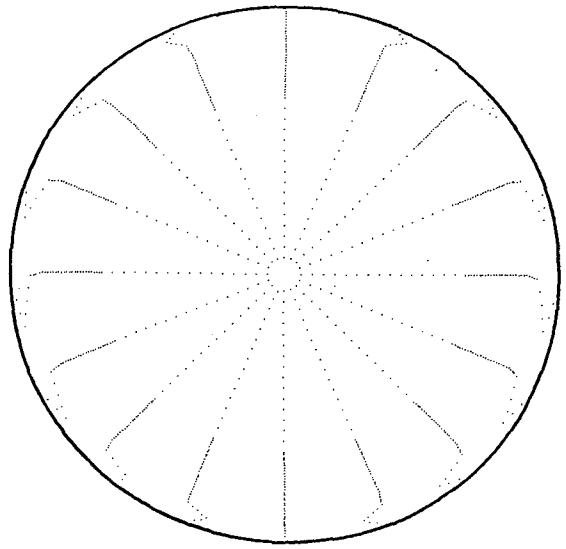

$t = 4.54$ seconds
$Gr = 2.9 \times 10^7$

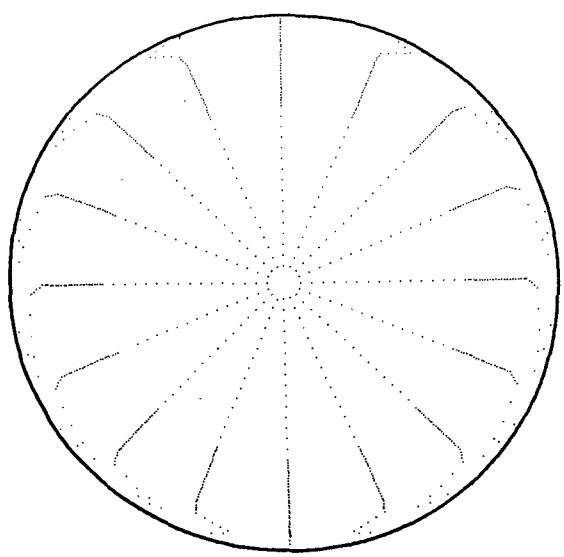

$t = 5.13$ seconds
$Gr = 3.6 \times 10^7$

Figure 19.- (Continued).

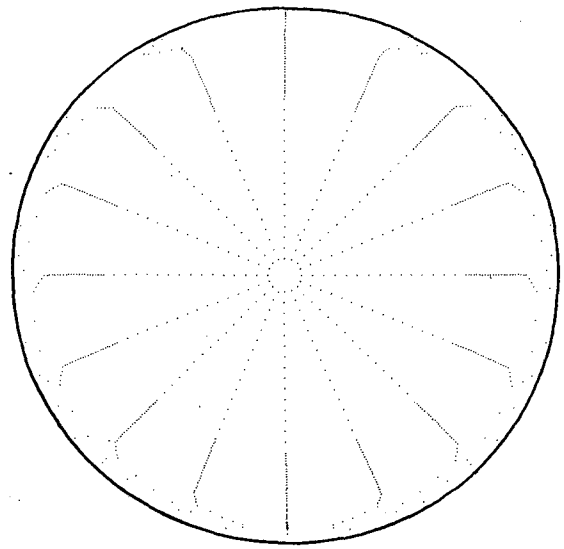

$t = 5.67$ seconds
$Gr = 4.2 \times 10^7$

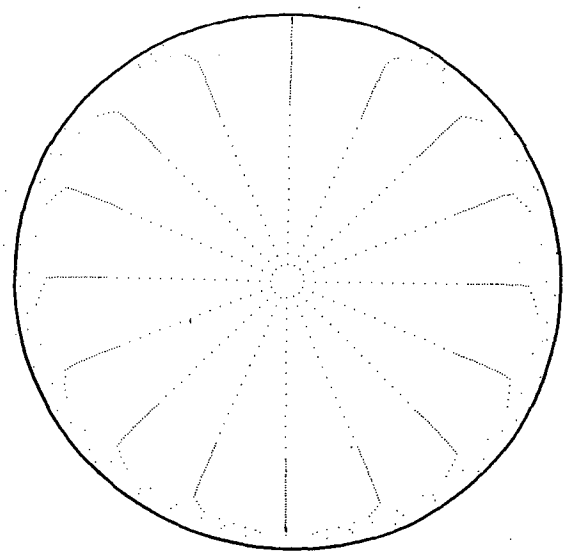

$t = 6.15$
$Gr = 4.9 \times 10^7$

Figure 19.- (Continued).

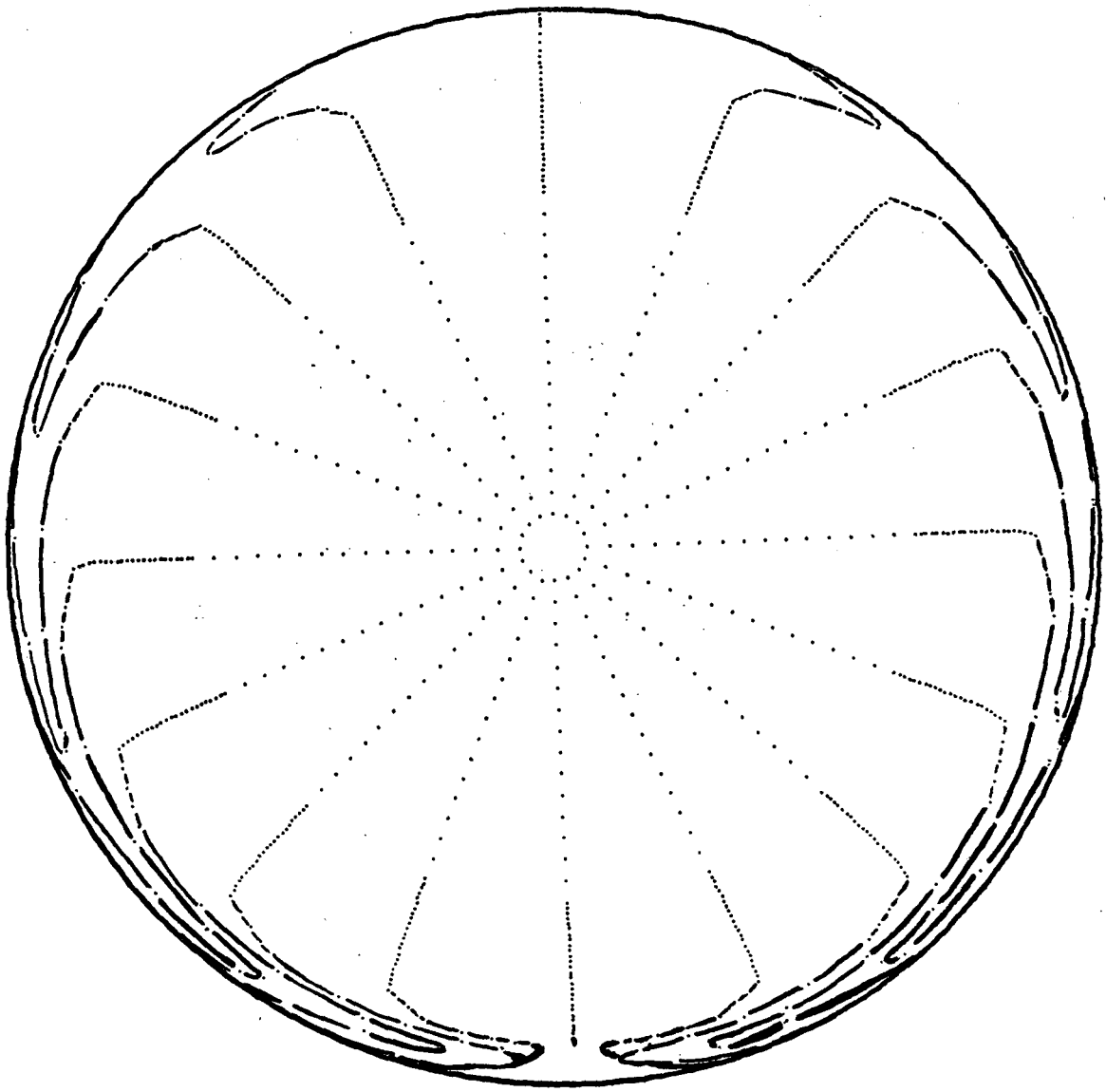

e. t=6.6 $G_r = 5.5 \times 10^7$

Figure 19.- (Concluded).

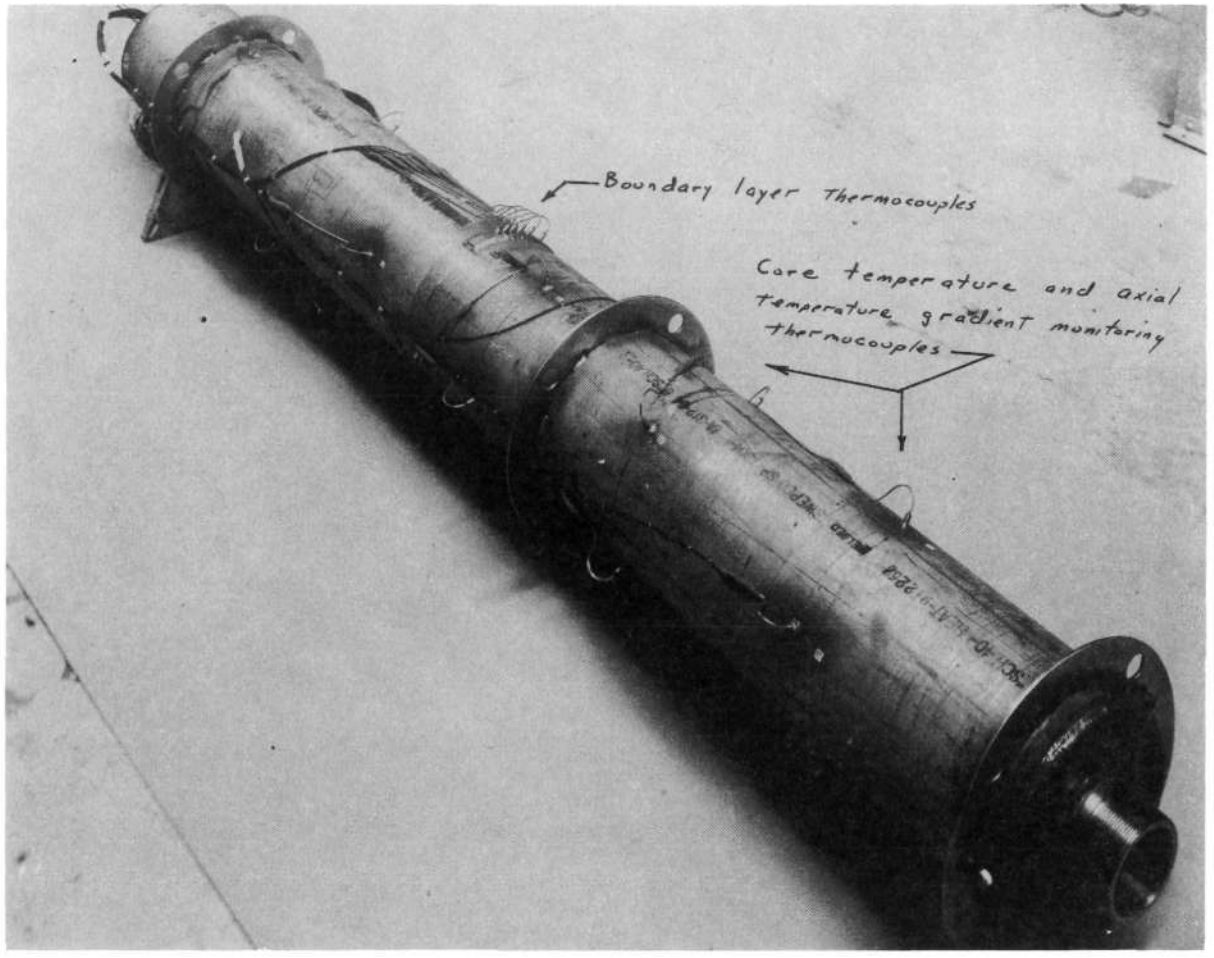

Figure 20a.- Instrumented natural convection chamber.

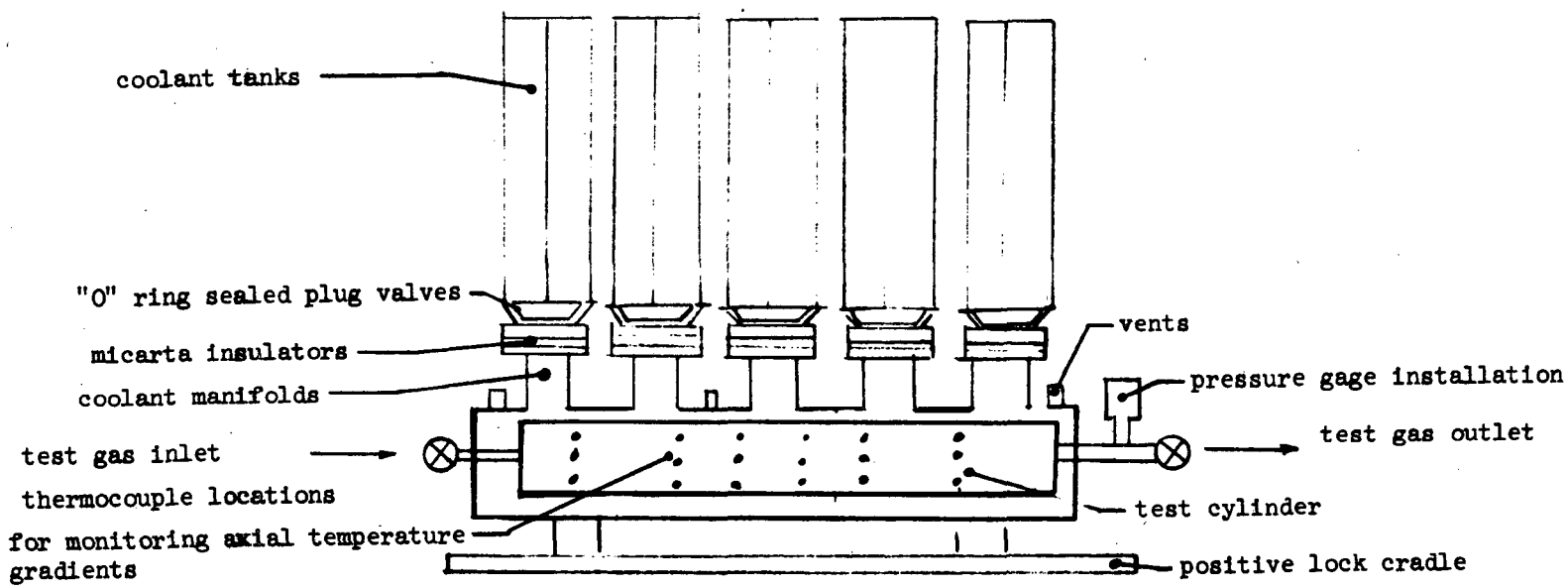

Figure 20b.- Schematic diagram of experimental natural convection apparatus.

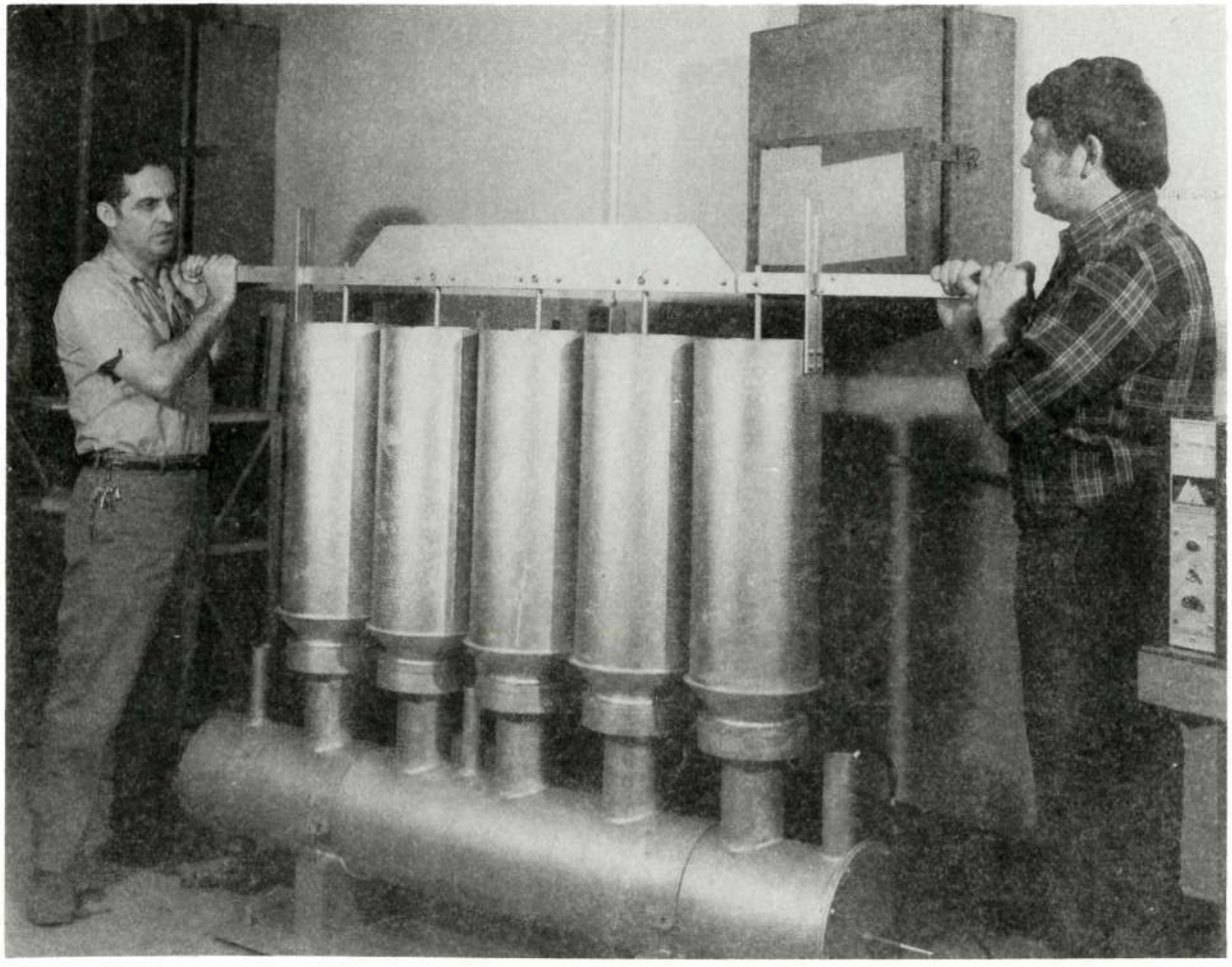

Figure 21.- Cooling manifolds for natural convection chamber.

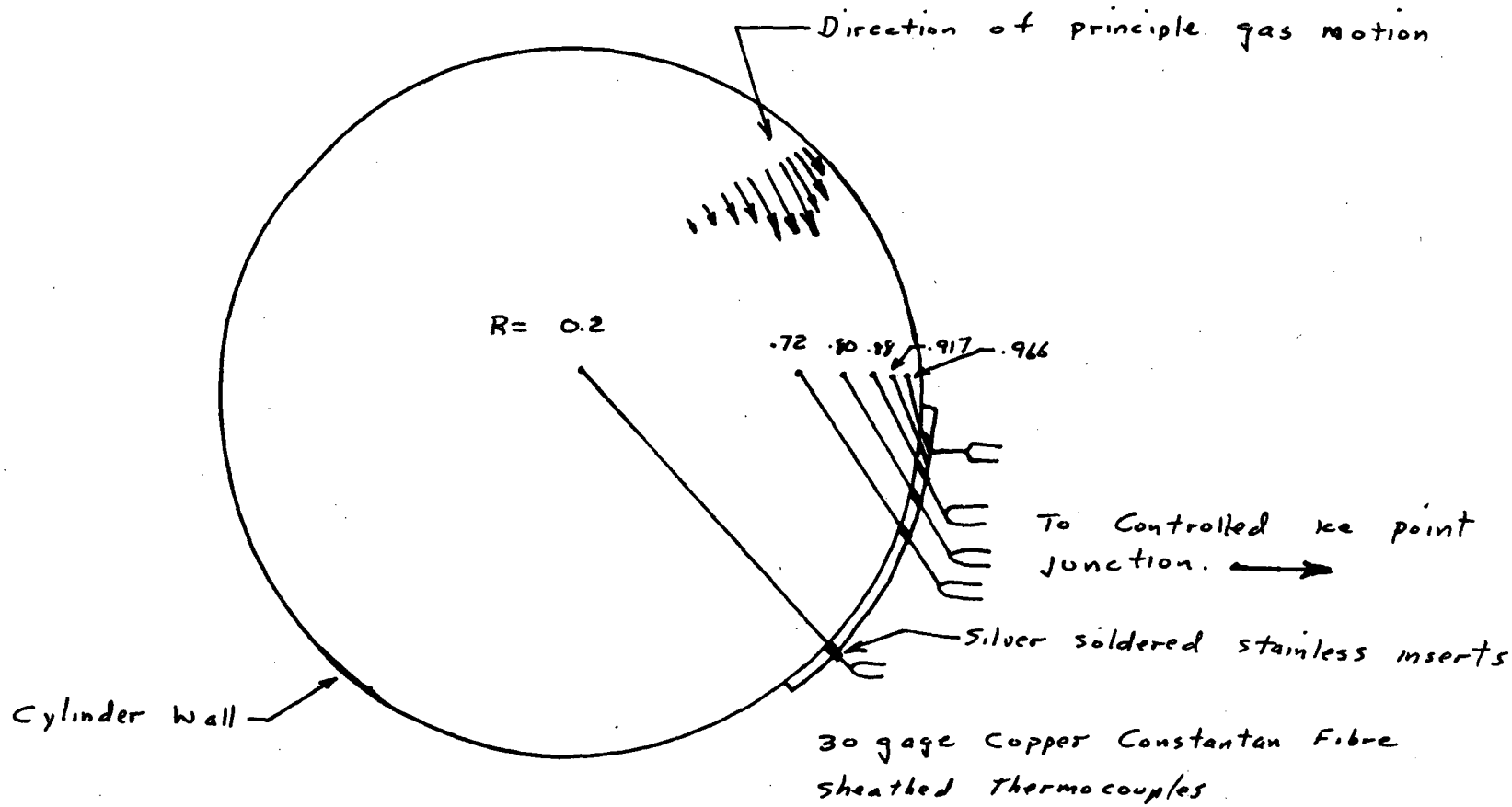

Figure 22.- Boundary layer and core thermocouple locations within horizontal cylinder.

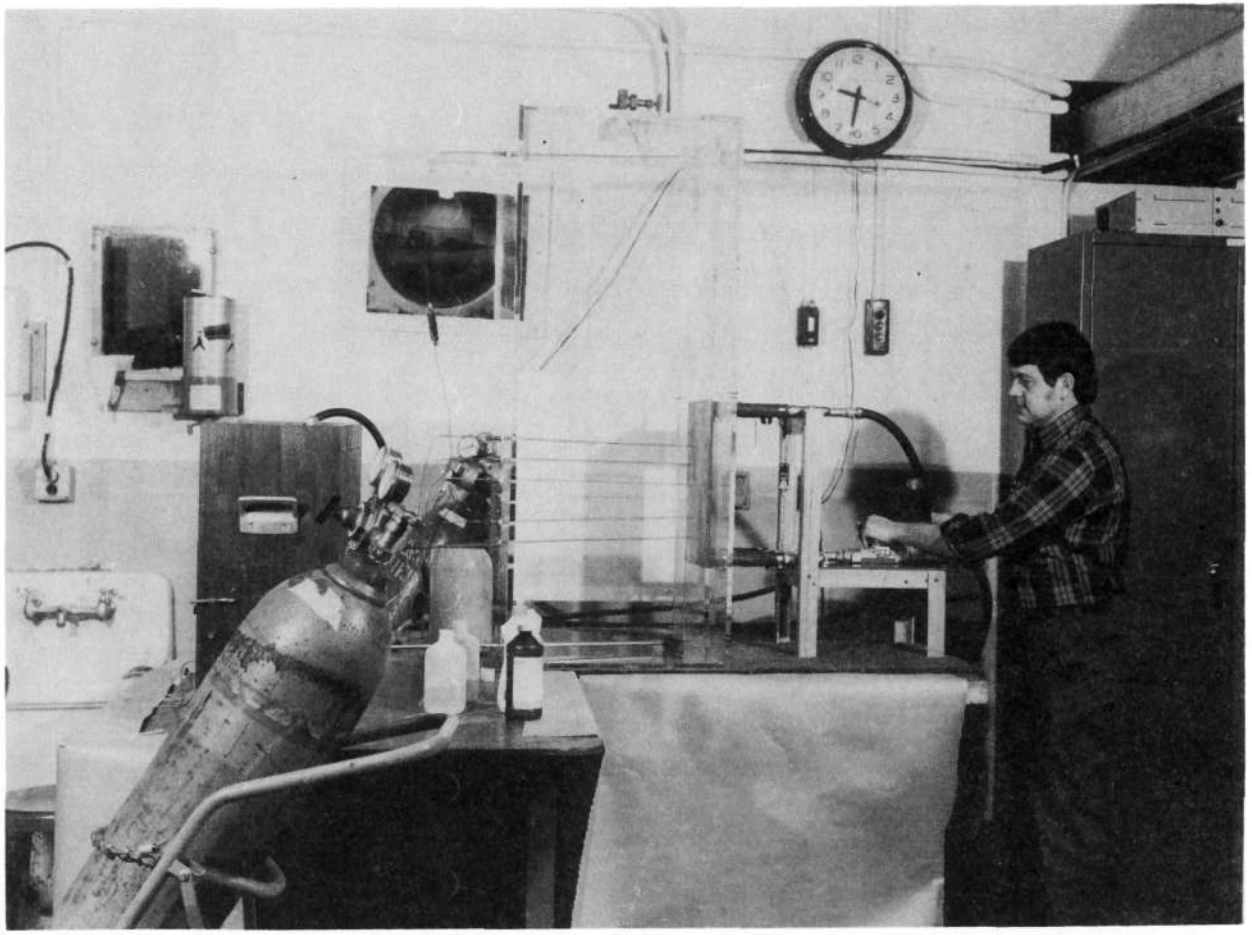

Figure 23a.- Vertical flat plate used for natural convection velocity measurements.

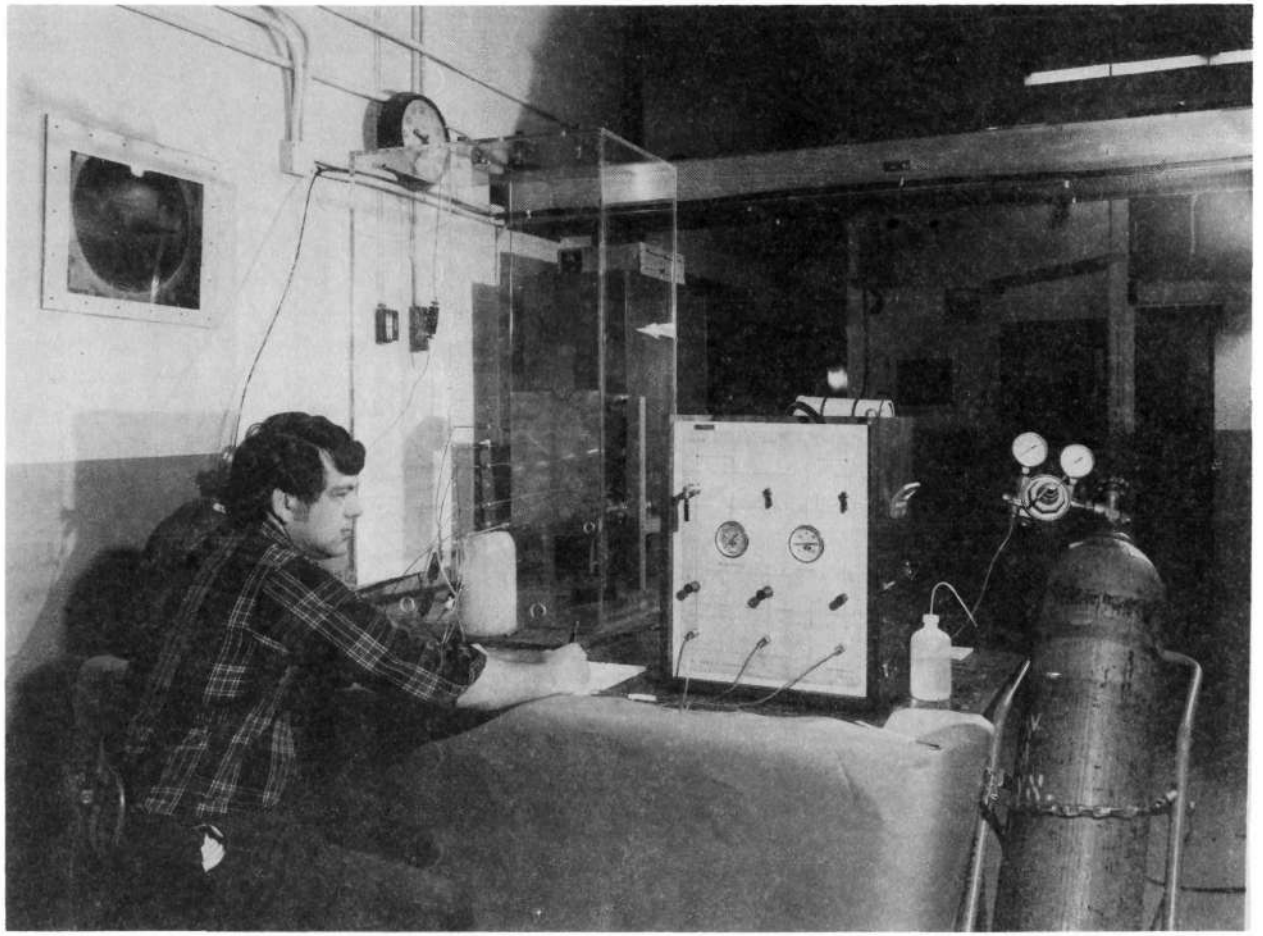

Figure 23b.- Vertical flat plate apparatus concluded.

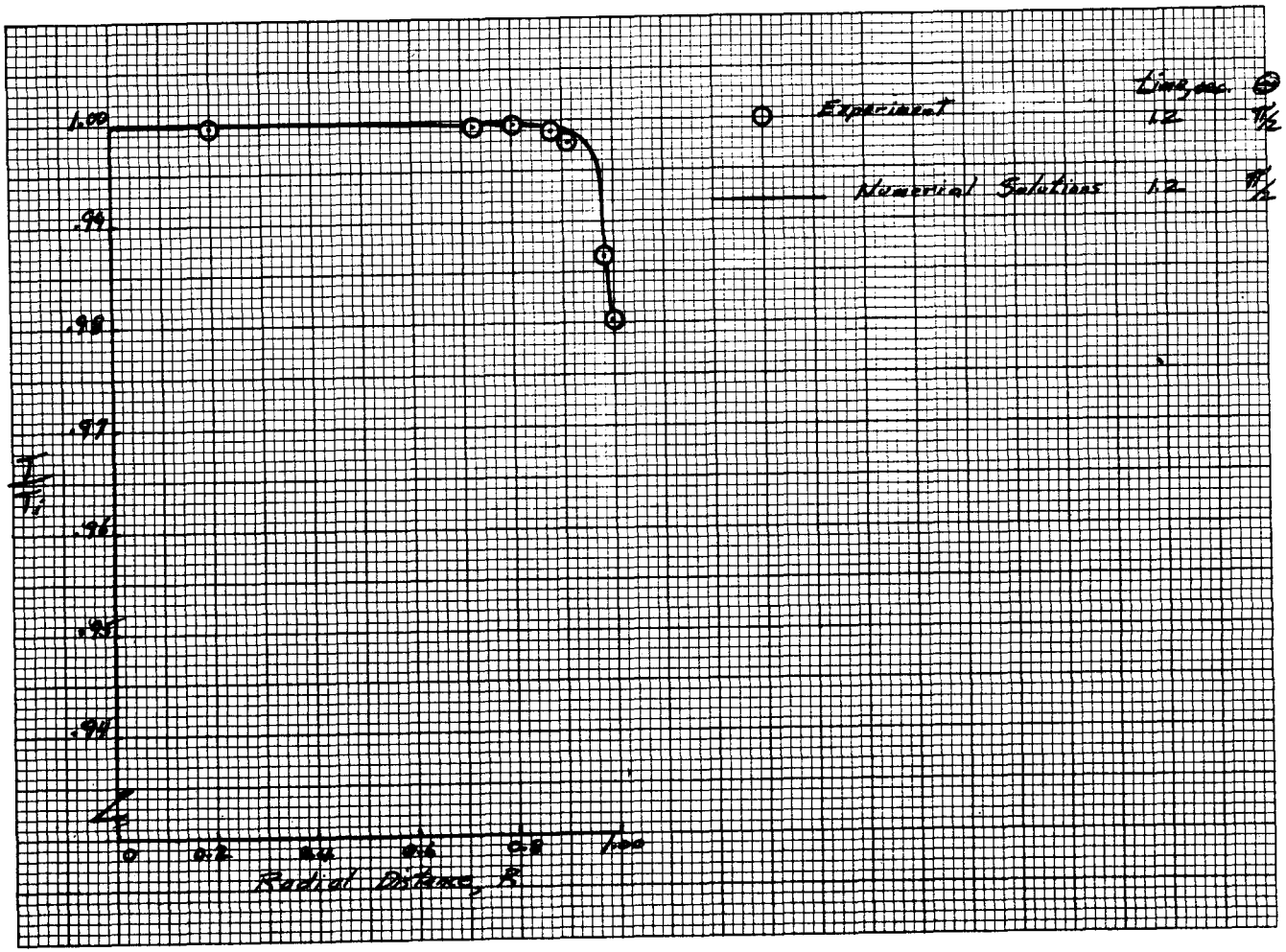

Figure 24a.- Temperature distribution for a time dependent wall boundary condition.

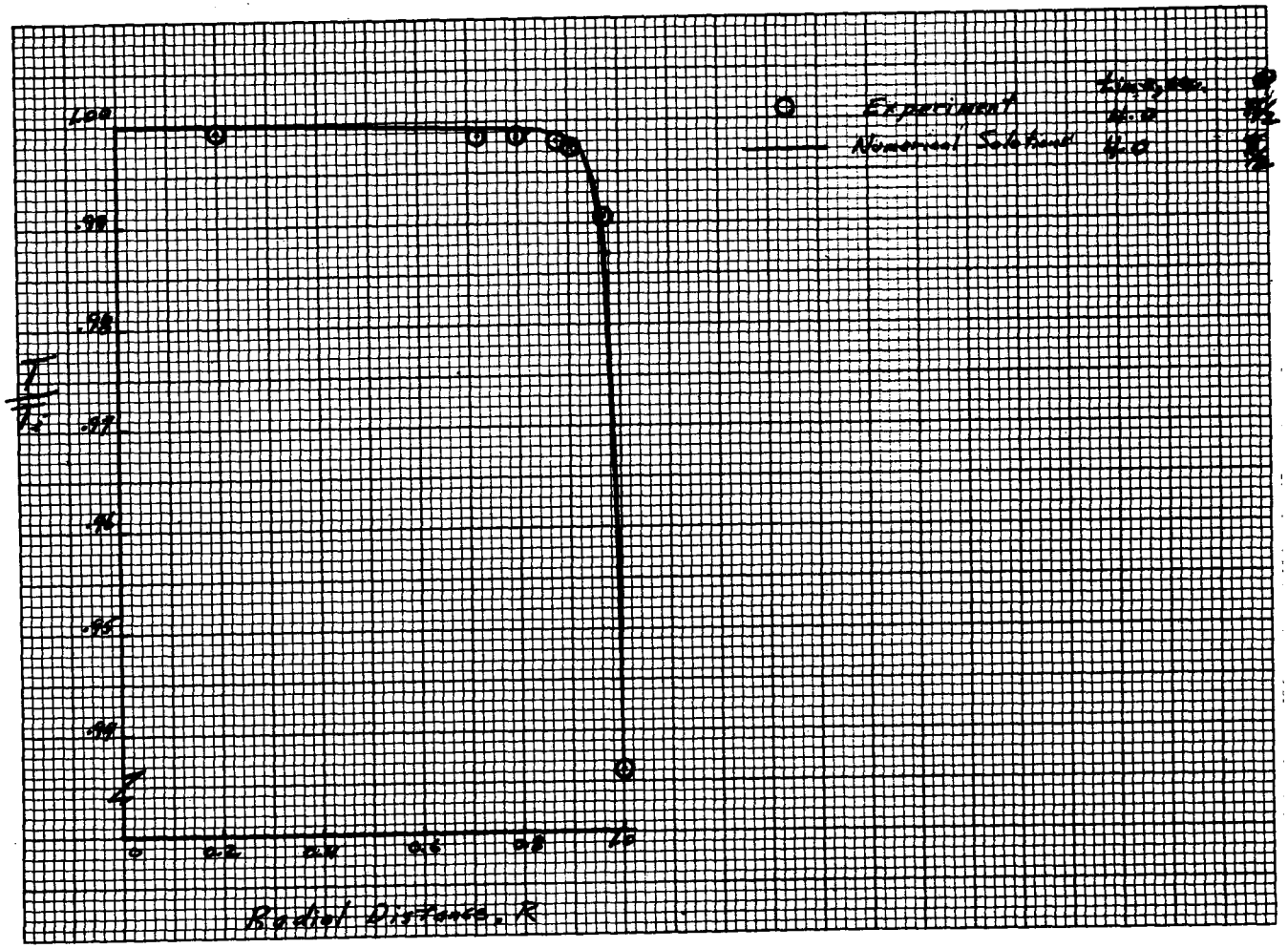

Figure 24b.- Temperature distribution for a time dependent wall temperature.

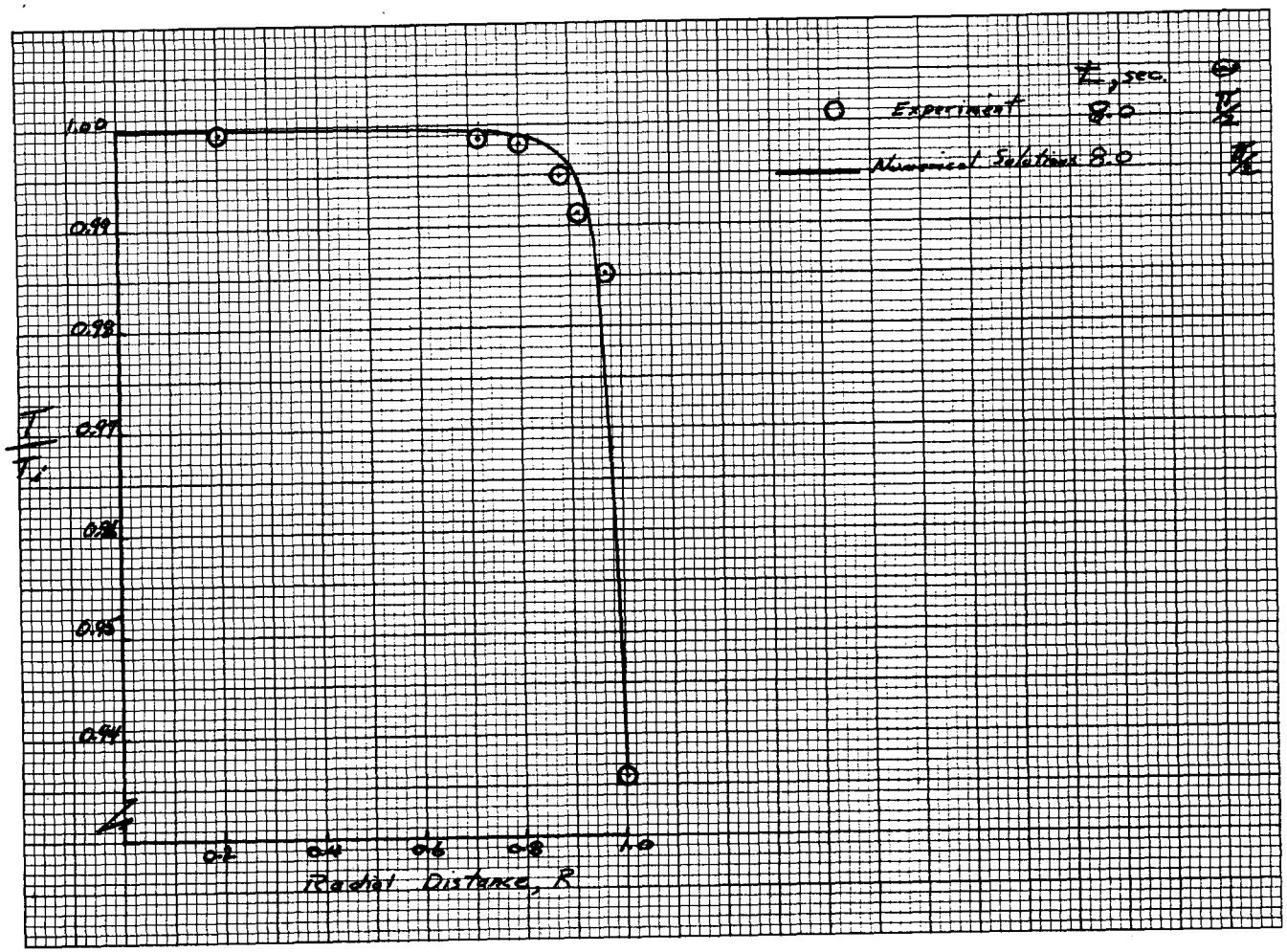

Figure 24c.- Temperature distribution for a time dependent wall boundary condition.

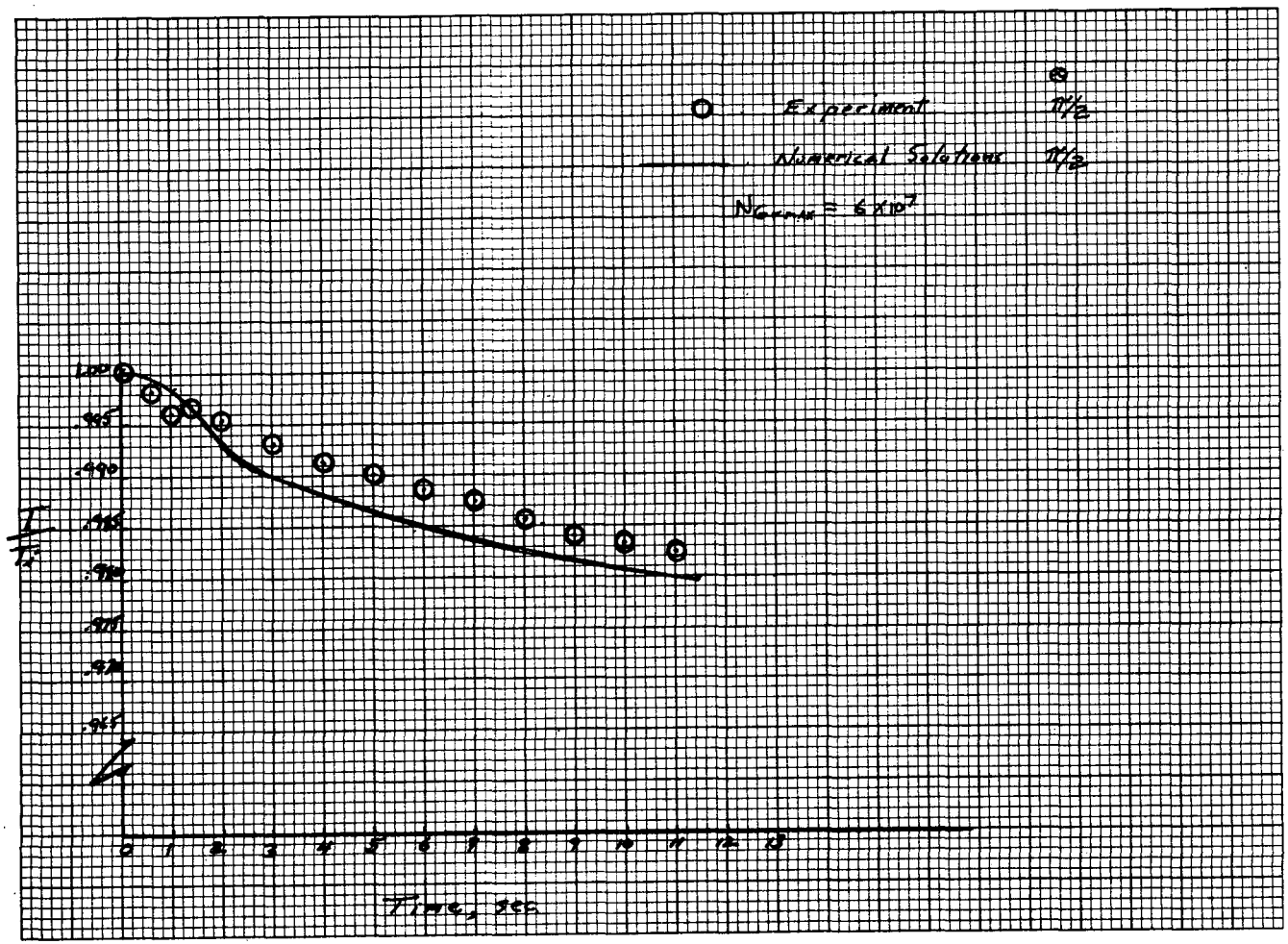

Figure 25a.- Boundary layer temperature decay at $\theta = 90^{\circ}$ and $R = .966$.

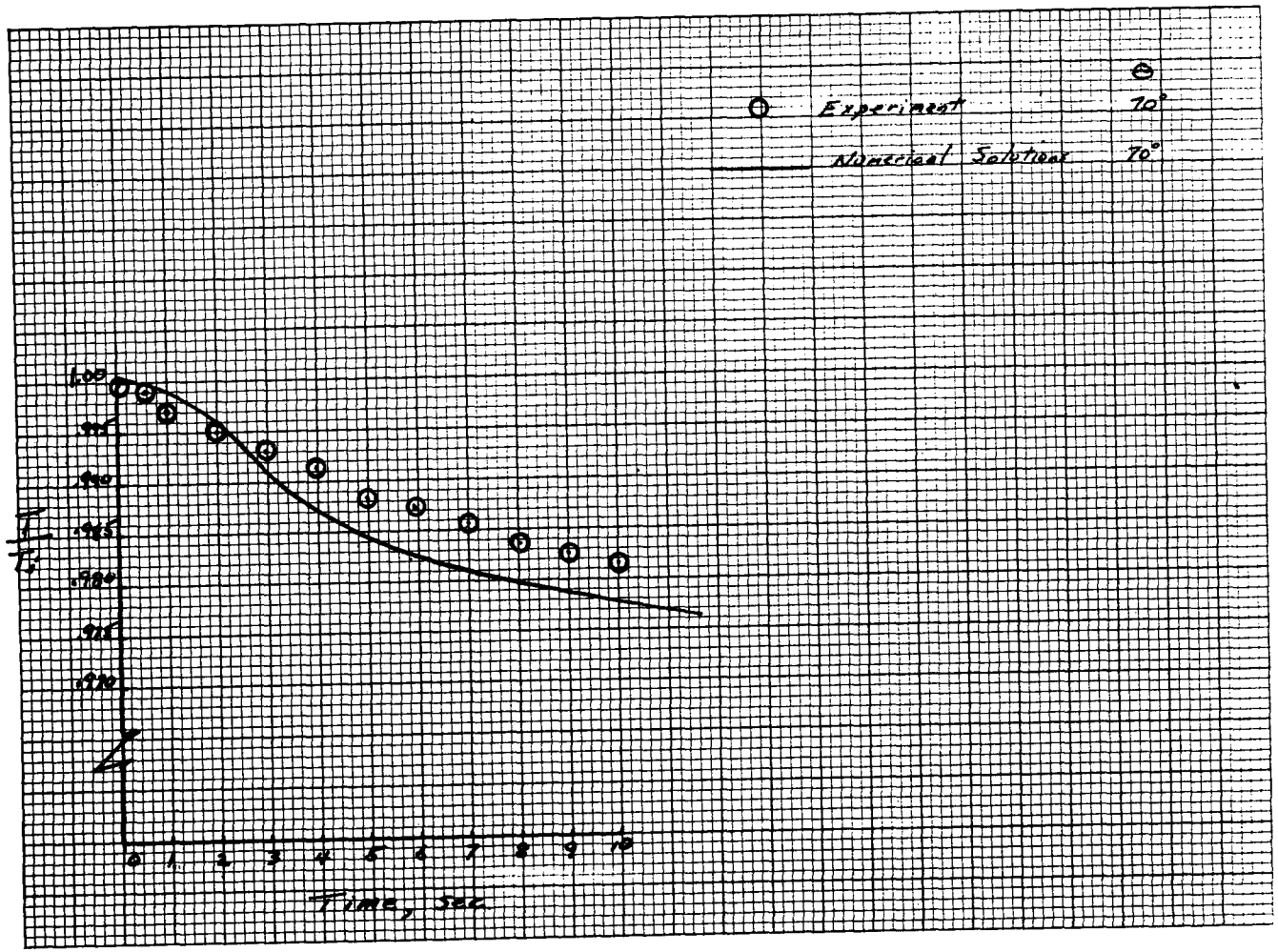

Figure 25b.- Boundary layer temperature decay at R = .966.

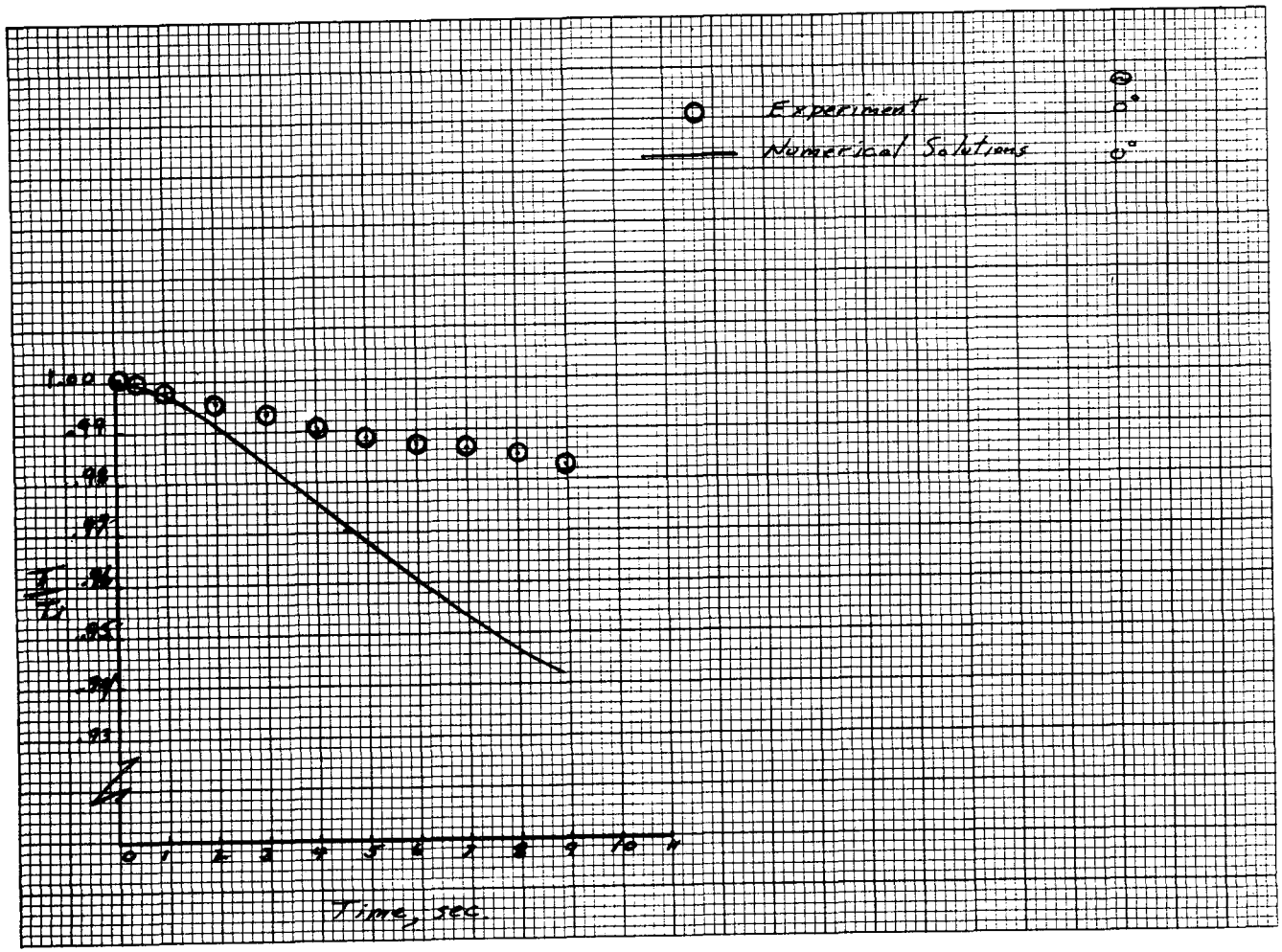

Figure 25c.- Boundary layer temperature decay at $\theta = 0^{\circ}$ and $R = .966$.

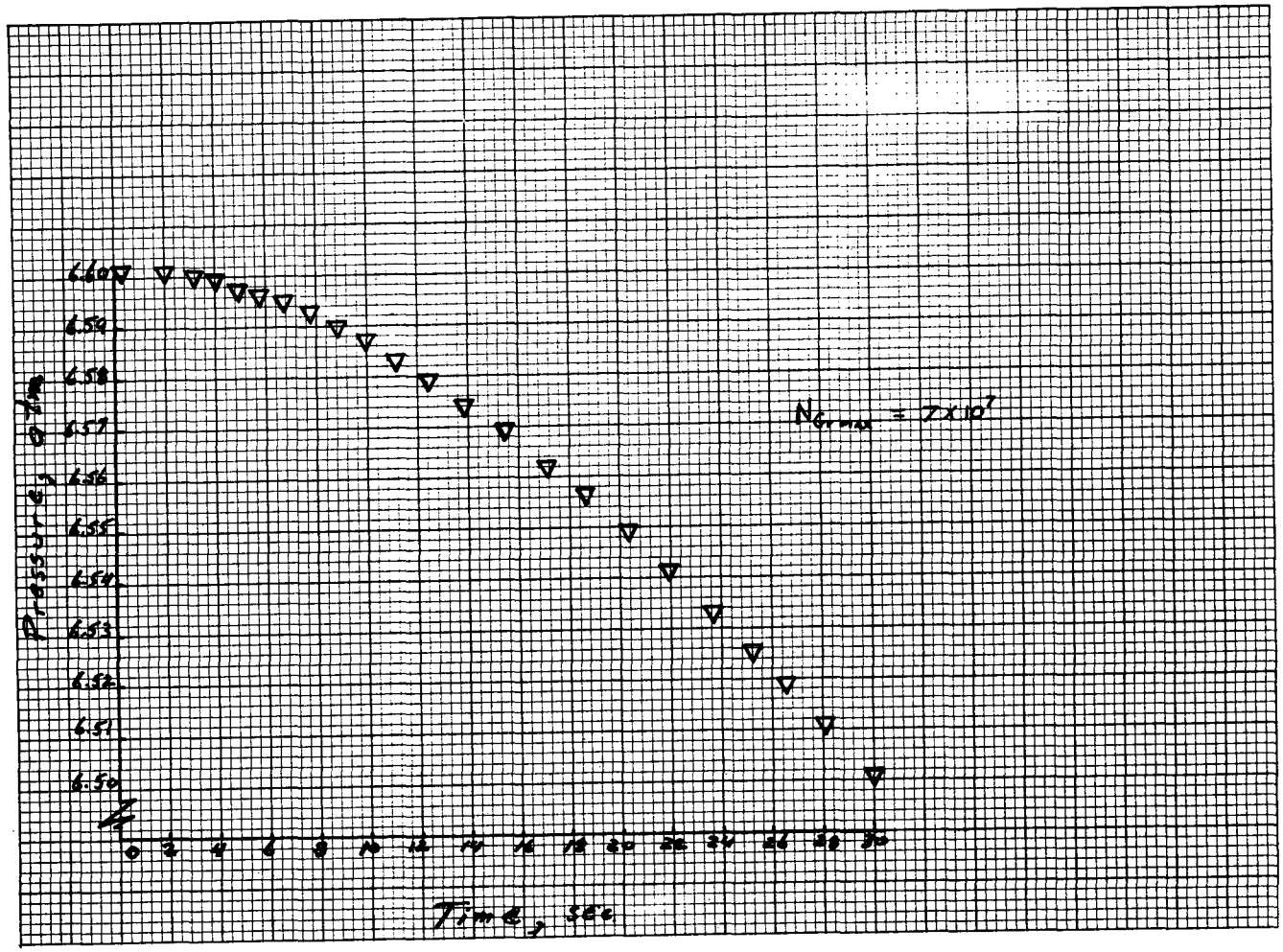

Figure 26.- Measured pressure decay in natural convection flow within a horizontal cylinder.

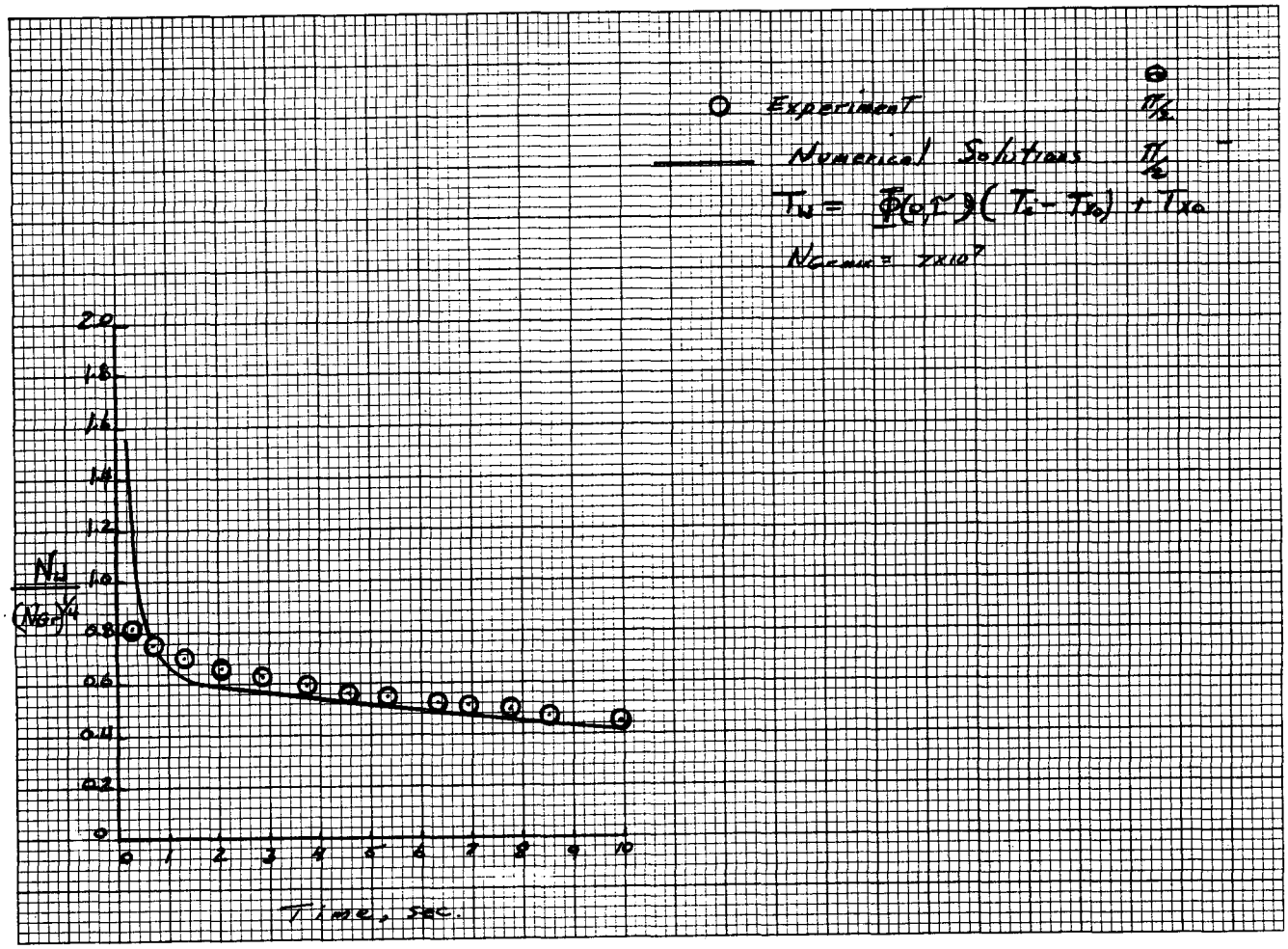

Figure 27.- Nusselt-Grashof relation for natural convection flow within a horizontal cylinder.

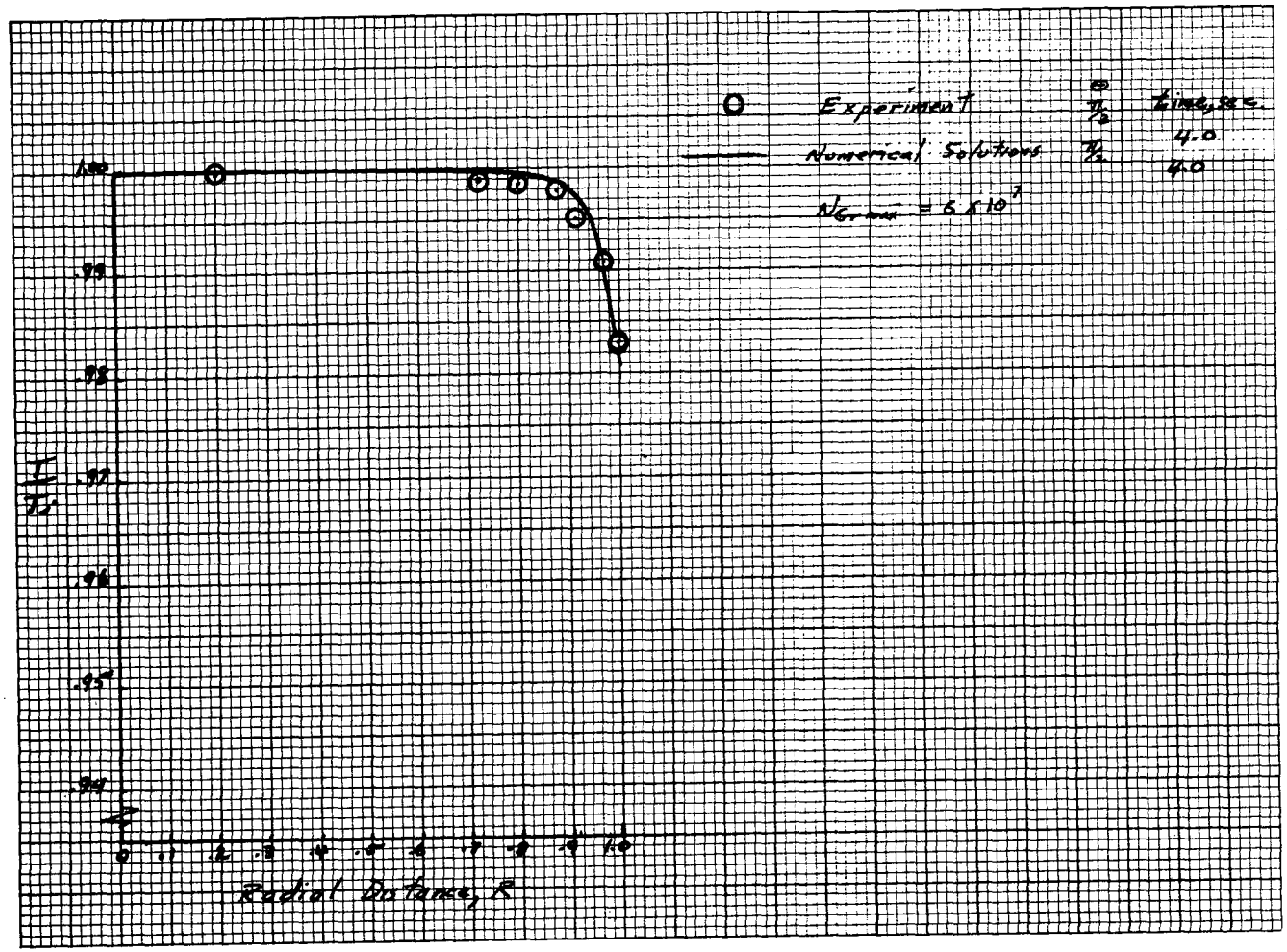

Figure 28a.- Radial temperature distribution at $\theta = 90^{\circ}$, $t = 4.0$ seconds.

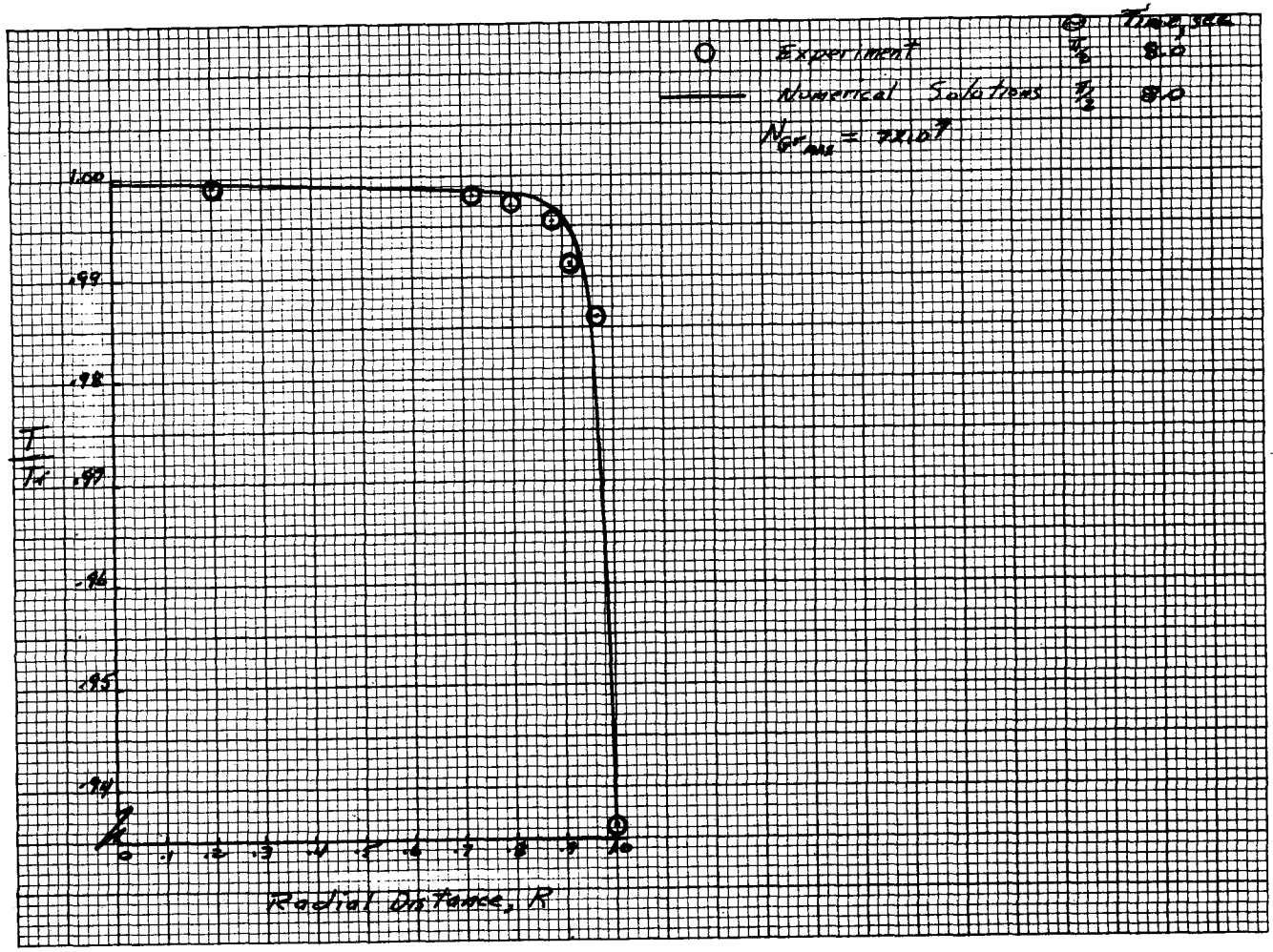

Figure 28b.- Radial temperature distribution at $\theta = 90^{\circ}$, t = 8.0 seconds.

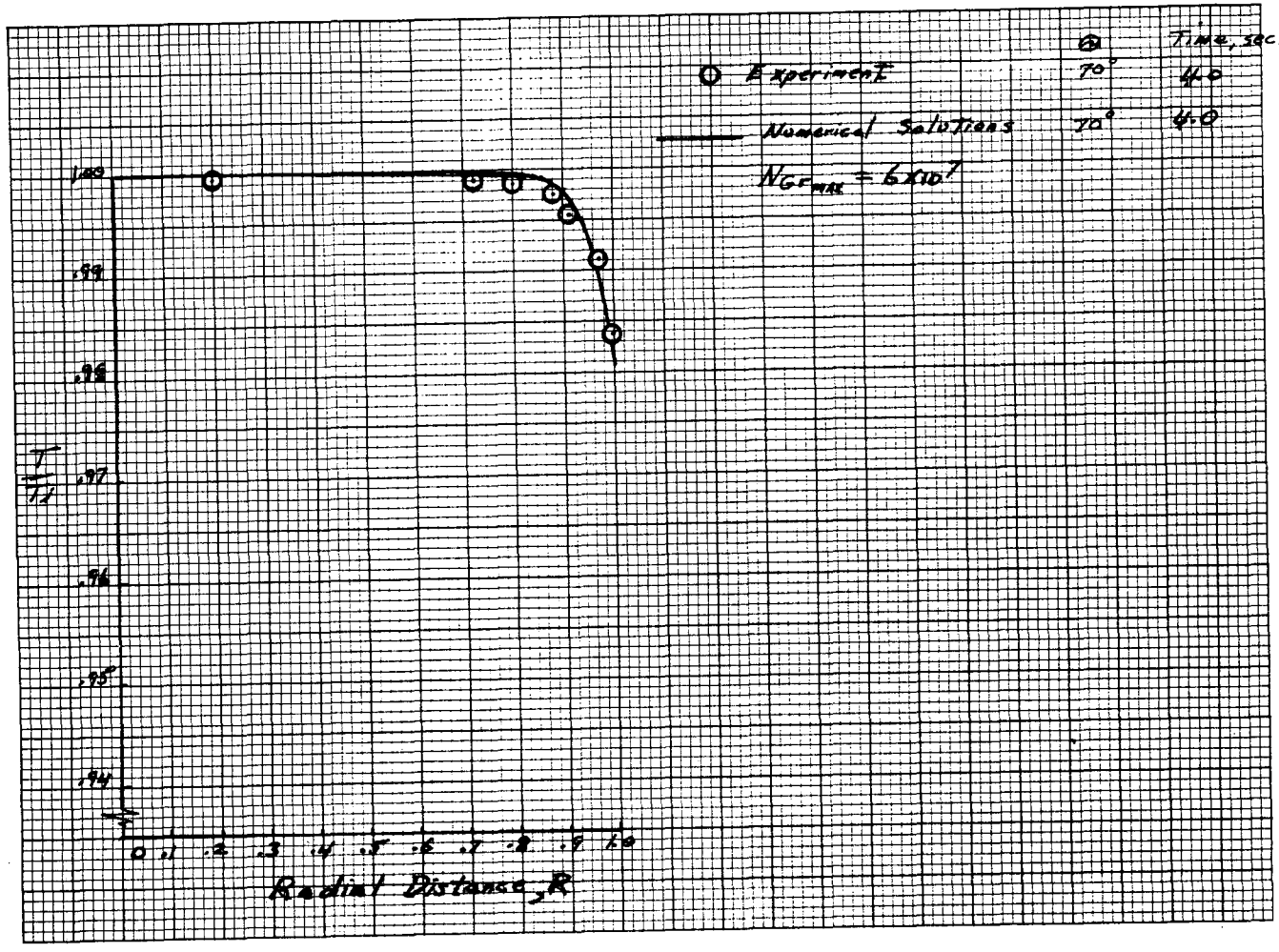

Figure 29a.- Radial temperature distribution at $\theta = 70^{\circ}$, t = 4 seconds.

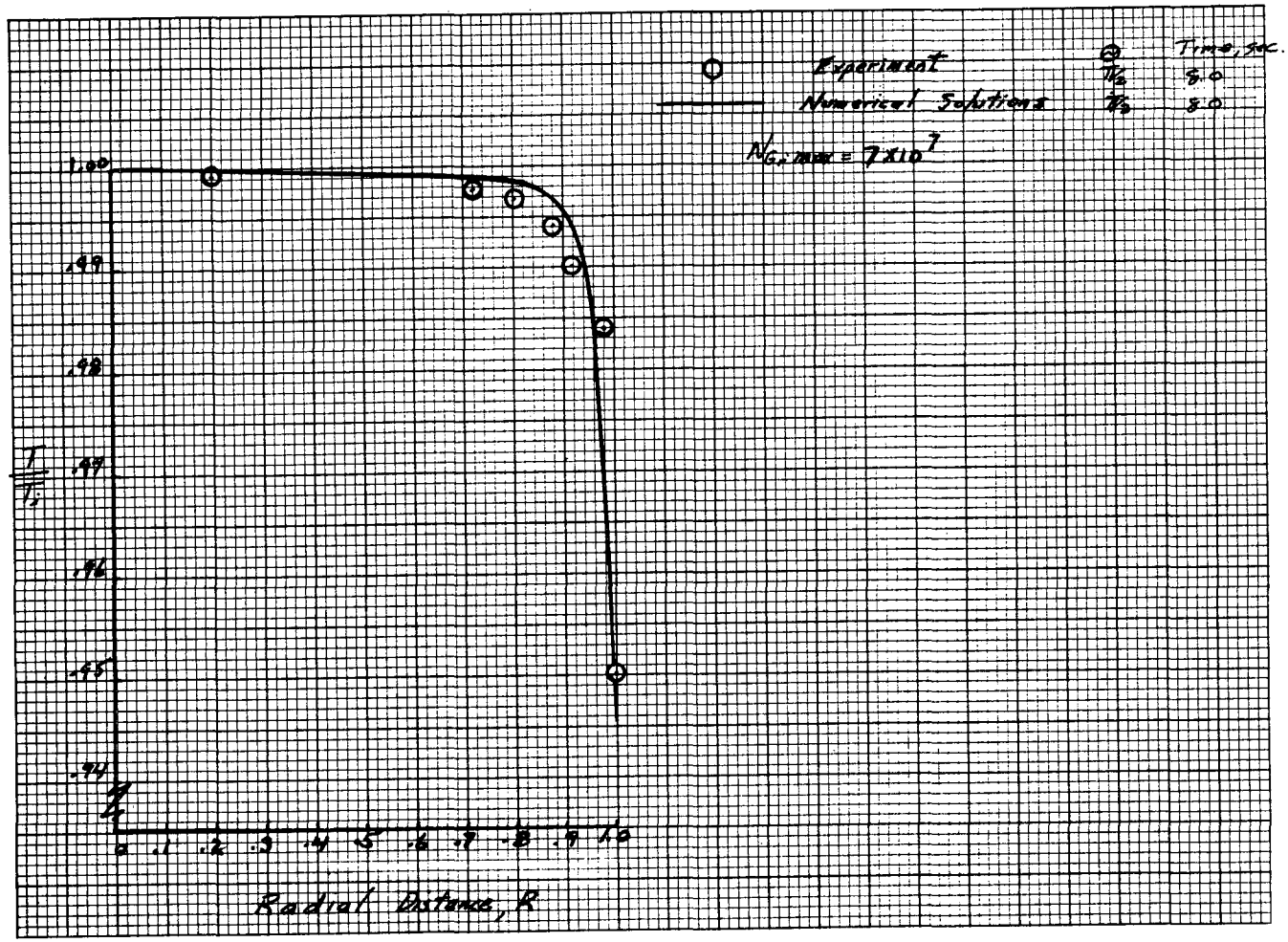

Figure 29b.- Radial temperature distribution at $\theta = 70^{\circ}$, t = 8.0 seconds.

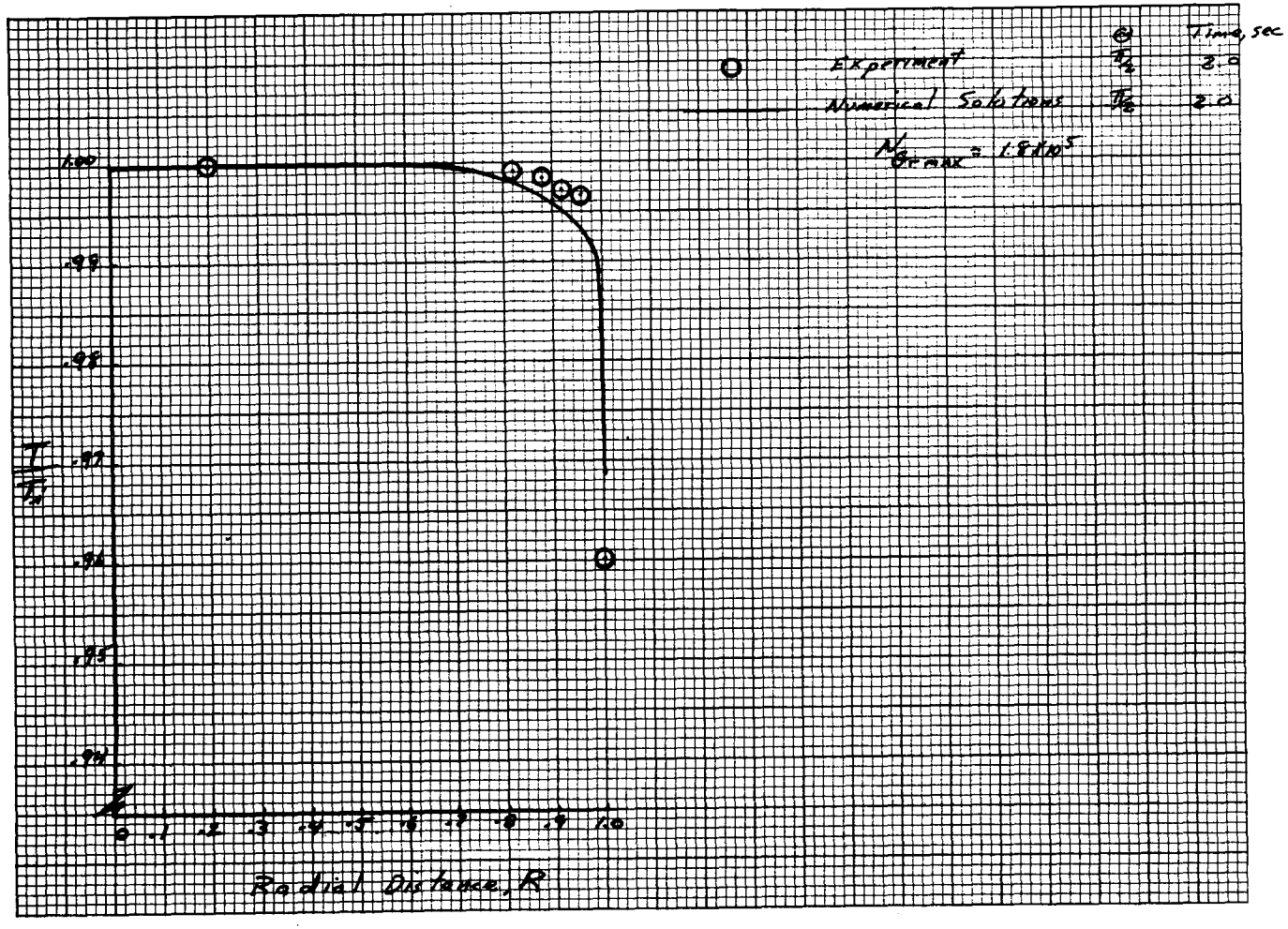

Figure 30a.- Radial temperature distribution at $\theta = 90^{\circ}$, t = 2.0 seconds.

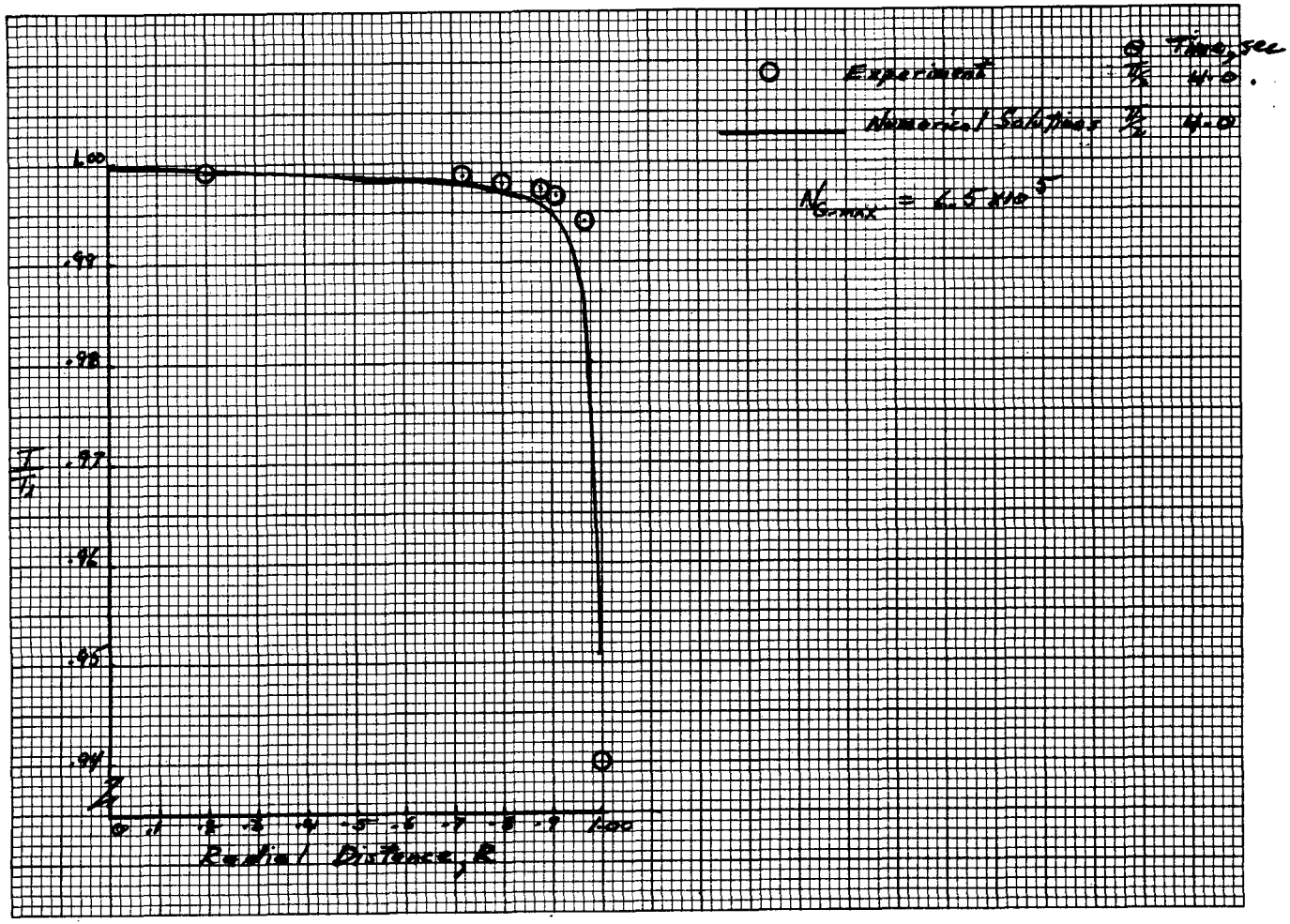

Figure 30b.- Radial temperature distribution at $\theta = 90^{\circ}$, $t = 4.0$ seconds.

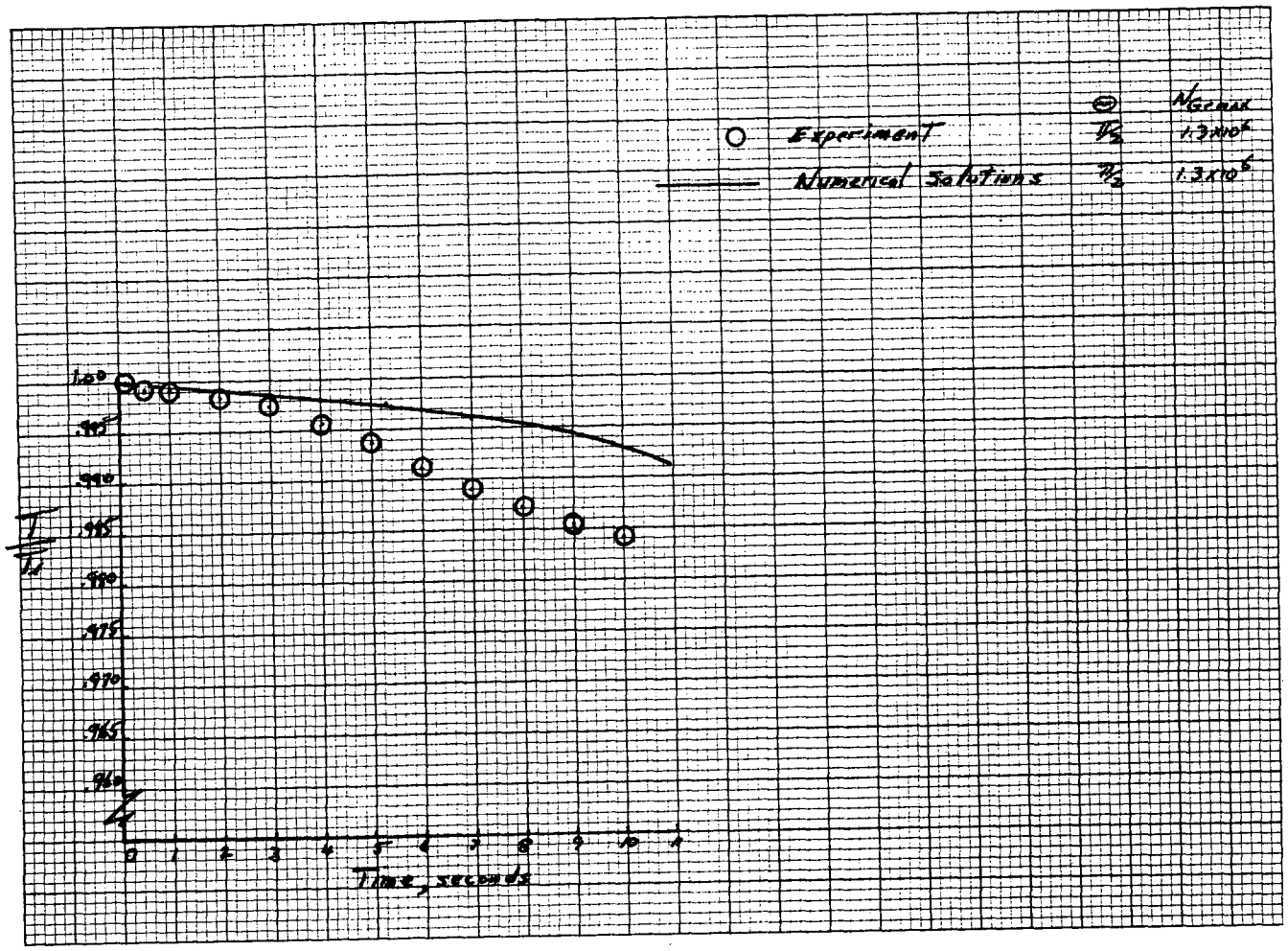

Figure 31.- Boundary layer temperature decay at $\theta = 90^{\circ}$ and $R = .966$, $G_{r\ max} = 1.3 \times 10^{6}$.

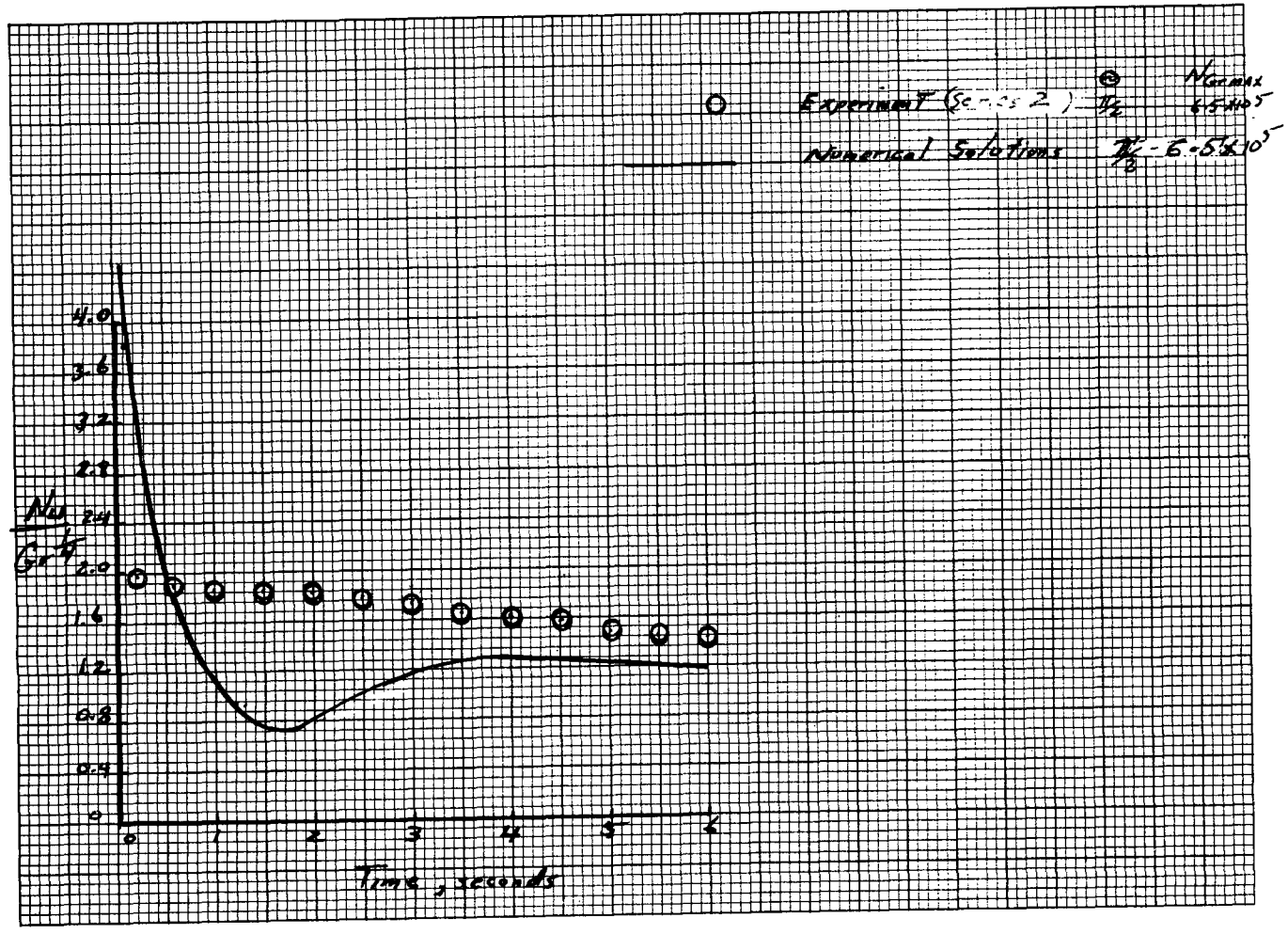

Figure 32.- Nusselt Grashof relation for $\theta = 90^{\circ}$, $G_{r\ max} = 6.5 \times 10^{5}$.

VITA

The author was born [redacted]. After moving to Seattle, Washington in 1938 he graduated from Garfield High School in Seattle. Two years after entering the University of Washington he entered the Naval Aviation Training program and in 1954 earned his commission and Naval aviators wings. For two and one half years he flew with an operational Marine jet fighter squadron. Following completion of military service the author enrolled in the University of Colorado School of Engineering. In 1960 had earned a Bachelor of Science degree in Aerospace Engineering from the University of Colorado and in that same year began full time employment with the National Aeronautics and Space Administration at the Langley Research Center. Through the NASA cooperative study program, the author earned a Master of Aerospace Engineering degree from the University of Virginia in 1964. In September of 1968 the author entered graduate school at Virginia Polytechnic Institute to begin study for the degree of Doctor of Philosophy in Aerospace Engineering.

The author resides in Yorktown, Virginia with his wife, Patricia, and three sons, Roger, Keith, and Gordon.